Electronic and magnetic properties of nanostructured graphene

Thomsen, Morten Rishøj

DOI (link to publication from Publisher):
10.5278/vbn.phd.engsci.00140

Publication date:
2016

Document Version
Publisher's PDF, also known as Version of record

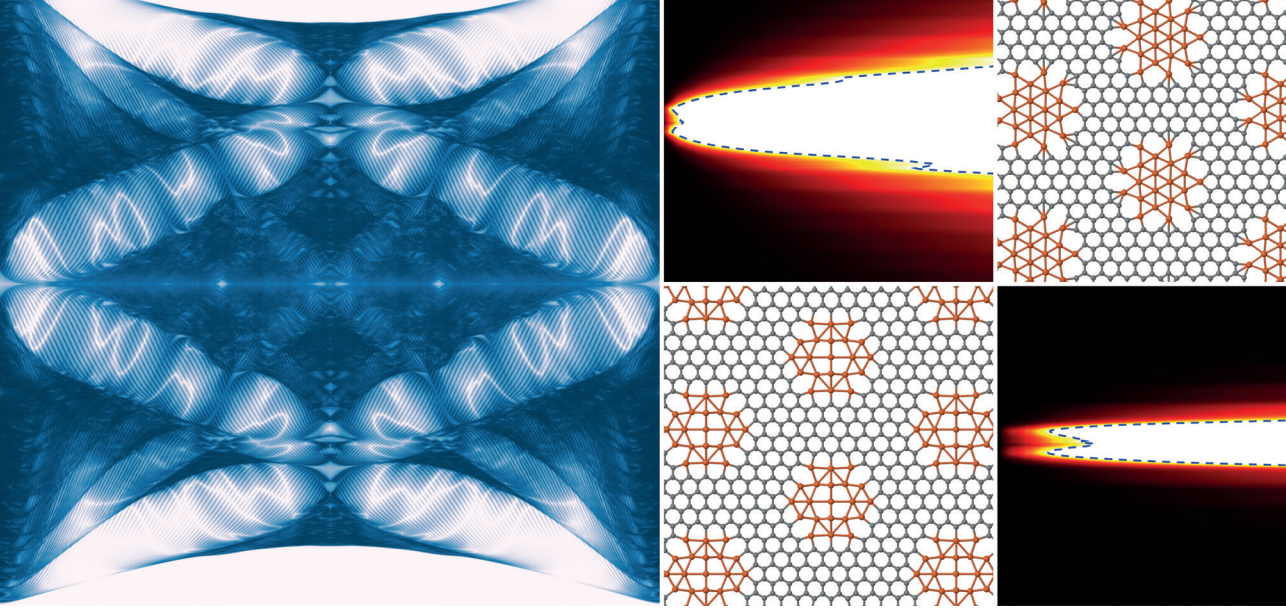

ELECTRONIC AND MAGNETIC PROPERTIES OF NANOSTRUCTURED GRAPHENE

BY
MORTEN RISHØJ THOMSEN

DISSERTATION SUBMITTED 2016

AALBORG UNIVERSITY
DENMARK

Electronic and magnetic properties of nanostructured graphene

Ph.D. Dissertation

Morten Rishøj Thomsen
Department of Physics and Nanotechnology
Aalborg University

AALBORG UNIVERSITY
DENMARK

Dissertation submitted September 9, 2016

Dissertation submitted: September 9, 2016

PhD supervisor: Prof. Thomas Garm Pedersen
Aalborg University

PhD committee: Associate Professor Lars Diekhöner (chairman)
Aalborg University, Denmark

Professor Nuno Miguel Machado Reis Peres
University of Minho, Portugal

Professor Mads Brandbyge
DTU Nanotech, Denmark

PhD Series: Faculty of Engineering and Science, Aalborg University

ISSN (online): 2246-1248
ISBN (online): 978-87-7112-791-1

Published by:
Aalborg University Press
Skjernvej 4A, 2nd floor
DK – 9220 Aalborg Ø
Phone: +45 99407140
aauf@forlag.aau.dk
forlag.aau.dk

Printed in Denmark by Rosendahls, 2016

English abstract

This thesis focuses on exploring the electronic and magnetic properties of nanostructured graphene from a theoretical and computational physics point of view. Pristine graphene does not have a band gap, making it unsuitable for semiconductor applications such as field effect transistors. The main focus in this work is calculating the properties of graphene antidot lattices (GALs), which are periodic perforations in an otherwise pristine graphene sheet, and which open a tunable band gap in the material. The thesis has a strong focus on simulations of very large systems in an attempt to reach the point, where the simulated systems are of comparable size to experiments. To that end, a considerable effort has been made on formulating methods for calculating electronic structure and electronic transport in graphene antidot structures based on a low-energy approximation, known as the Dirac equation (DE). The calculation time of these methods is scale invariant and thus allows for simulations of arbitrarily large systems. These DE models are demonstrated to be very accurate in the absence of localized edge states, which are common for antidots with zigzag edge chirality. The DE-based models are thus ideal for calculating properties of very large graphene antidot systems, but only when the effects of edge states are negligible.

The transport properties of graphene with magnetic impurities and GALs under a magnetic field have also been investigated. The transport properties are calculated using the non-equilibrium Green's function formalism, which is a very efficient method that makes it possible to handle systems with up to hundreds of thousands of atoms.

Magnetic fields are often used to characterize transport in nanoscale materials, which makes it important to understand how an applied magnetic field affects the transport properties. The presented magnetotransport study of GALs was inspired by recent experiments, which demonstrated that ballistic transport is possible in these systems. The presence of magnetic edge states is demonstrated, which are states that are localized on the periphery of the

antidots due the presence of a magnetic field. These states are demonstrated to survive a modest amount of disorder and are therefore expected to be observable in experiments as well.

Hydrogen adatoms are common magnetic impurities in graphene and it is therefore important to understand their influence on spin transport for graphene-based spin devices. The transport calculations show that even a dilute concentration of hydrogen adatoms is detrimental to the spin relaxation length, which was found to scale nearly linearly with the hydrogen concentration. Moreover, the spin relaxation mechanism was found to be Markovian only near the charge neutrality point or in the highly dilute limit.

Another common magnetic impurity is iron, which typically comes from leftover residue from a common method used to transfer CVD-grown graphene from copper to another substrate. Recent experiments have shown that monolayer iron membranes can be formed in graphene perforation by e-beam irradiation. However, the formation and stability of these membranes are not yet understood theoretically. The lattice geometry in experiments was found to be square, while it is predicted to be triangular for freestanding monolayer iron. The bonds lengths in experiments are also much larger than predicted. In order to obtain a theoretical understanding of the membrane formation, the stability of iron membranes in GALs is studied using density functional theory (DFT). The DFT analysis shows that the reason for the lattice geometry is likely that, during formation, the square lattice is favored as it has a lower edge formation energy, which is the energy associated with having an open edge. After formation, the membrane is then kinetically hindered from rearranging into the triangular lattice. The increased bond lengths occur due to straining of the iron membrane by the very rigid graphene lattice.

Danish abstract

Denne tese fokuserer på de elektroniske og magnetiske egenskaber af nanostruktureret grafen fra et teoretisk og computerbaseret fysik synspunkt. Ren grafen har ikke et båndgab, hvilket gør det uegnet til halvlederanvendelser, såsom felteffekt transistorer. Det primære fokus i dette arbejde er at beregne egenskaberne af grafen antidotgitre (graphene antidot lattices, GALs), som er periodiske huller i et ellers rent grafenlag og som giver anledning til et justerbart båndgab. Der er stor fokus på simuleringer af meget store systemer i et forsøg på at nå systemstørreler, der er sammenlignelige med eksperimenter. Til det formål formuleres metoder til at beregne elektronisk struktur og elektronisk transport i graphene antidot systemer baseret på en lavenergi tilnærmelse, kendt som Diracligningen (Dirac equation, DE). Udregningstiden for disse metoder er målestoksuafhængige og giver derfor mulighed for beregninger på arbitrært store systemer. Det demonstreres at disse DE modeller er meget nøjagtige, når der ikke er lokaliserede kanttilstande, som er typiske ved antidots med zigzag kanter. De DE baserede modeller er derfor ideelle til at beregne egenskaberne af meget store grafen antidotsystemer, mun kun når effekten af kanttilstande er negligibel.

Transportegenskaberne af grafen med magnetiske urenheder og GAL systemer under et magnetfelt bliver også betragtet. Transportegenskaberne udregnes ved brug af en uligevægts Green's funktions methode, som er meget effektiv og giver mulighed for at håndtere systemer med op til hundredetusinder af atomer.

Magnetiske felter bruges ofte til karakterisering af transport i nanoskala materialer. Dette gør det vigtigt at forstå, hvordan et påtrykt magnetfelt påvirker transportegenskaberne. Det præsenterede studie af magnetotransport i GAL systemer er inspireret af nye eksperimenter, der demonstrerer at ballistisk transport er mulig i disse systemer. Forekomsten af magnetiske kanttilstande demonstreres, hvilket er tilstande der er lokaliserede på kanten af antidots grundet det magnetiske felt. Det demonstreres at disse tilstande over-

lever beskedne mængder af uorden og forventes derfor også at kunne observeres i eksperimenter.

Hydrogen adatomer er et typisk eksempel på magnetiske urenheder i grafen og det er derfor vigtigt at forstå deres indflydelse på spin transport i grafen. Transportberegningerne viser at selv en meget lav koncentration af hydrogen adatomer er ødelæggende for spin henfaldslængden. Det blev fundet at denne længe skalerer næsten lineært med hydrogen koncentrationen. Det blev også fundet at spinhenfaldsmekanismen kun er Markovisk nær ladningsnulpunktet for grafen, samt ved meget lav hydrogen koncentration.

En anden typisk magnetisk urenhed i grafen er jern, som typisk kommer fra en overførselsteknik der ofte bruges til af overføre CVD grafen til et andet substrat. Nye eksperimenter har vist at monolag jernmembraner kan dannes i grafenhuller ved bestråling med elektronstråler. Dannelsen og stabiliteten af disse membraner er dog endnu ikke forstået teoretisk. Gittergeometrien i eksperimenterne blev fundet til at være firkantet, selvom den er forudsagt til at være triangulær for fritstående jernmembraner. Bindingslængerne i eksperimenterne er også meget større end det forudsagte. For at opnå en teoretisk forståelse af membrandannelsen, analyseres stabiliteten af jernmembraner med tæthedsfunktionalteori. Analysen viser at gittergeometrien sandsynligvis kommer af at, det firkantede gitter er favoriseret under dannelsen, fordi det har en lavere kantformeringsenergi, som er den energi det koster at have en åben kant. Efter dannelsen er gitteret formentligt kinetisk hindret i at omordne sig til et triangulært gitter. De øgede bindingslænger kommer af tøjring af jernmembranen af det stærke grafengitter.

Contents

Thesis Details

Thesis Title:	Electronic and magnetic properties of nanostructured graphene
Ph.D. Student:	Morten Rishøj Thomsen
Supervisors:	Prof. Thomas Garm Pedersen, Aalborg University

The main body of this thesis consist of the following papers.

[I] S. J. Brun, **M. R. Thomsen** and T. G. Pedersen, *Electronic and optical properties of graphene antidot lattices: comparison of Dirac and tight-binding models*, J. Phys. Condens. Matter **26**, 335301 (2014).

[II] **M. R. Thomsen**, S. J. Brun and T. G. Pedersen, *Dirac model of electronic transport in graphene antidot barriers*, J. Phys. Condens. Matter **26**, 265301 (2014).

[III] **M. R. Thomsen**, S. J. Brun and T. G. Pedersen, *Stability and magnetization of free-standing and graphene-embeded iron membranes*, Phys. Rev. B **91**, 125439 (2915).

[IV] **M. R. Thomsen**, M. M. Ervasti, A. Harju and T. G. Pedersen, *Spin transport in hydrogenated graphene*, *Phys. Rev. B* **92**, 195408 (2015).

[V] **M. R. Thomsen**, S. R. Power, A.-P. Jauho and T. G. Pedersen, *Magnetic edge states and magnetotransport in graphene antidot barriers*, Phys. Rev. B **94**, 045438 (2016).

This thesis has been submitted for assessment in partial fulfillment of the PhD degree. The thesis is based on the published scientific papers which are listed above. As part of the assessment, co-author statements have been made available to the assessment committee and are also available at the Faculty. The thesis is not in its present form acceptable for open publication but only in limited and closed circulation as copyright may not be ensured.

Preface

This thesis summarizes the work I have done as a PhD student at the Department of Physics and Nanotechnology at Aalborg University as well as the work I have done as visiting researcher at the Quantum Many-Body Physics group at Aalto University, over the past three years in the period 2013 – 2016.

Already in the summer of 2012, my PhD supervisor, Professor Thomas Garm Pedersen, suggested the research topic of nanostructured graphene to Søren Jacob Brun and myself. Based on this topic, Søren and I decided to write our Master's thesis in collaboration. The thesis went sufficiently well that we were both offered PhD positions in Prof. Pedersen's research group focusing on large-scale simulations of nanostructured graphene. My work has primarily focused on developing and implementing methods for dealing with large-scale systems based on graphene.

There are several people I would like to thank, who in some shape or form have helped me through my PhD studies. First of all, I would like to thank Thomas Garm Pedersen, not only for proposing an exciting research topic to me, but also for his continued support, skilled supervision and his immense insight of physics. I would also like to thank Ari Harju for an extremely hospitable stay at his research group at Aalto University. It was a valued and productive three months for me. I would advise others from going to Finland during winter, but the sometimes questionable weather kept me indoors much of the time, which helped me focus on my research. I would also like to thank two of his students, Mikko Ervasti and Ville Vierimaa, for their collaboration and interesting discussions. I would like to thank my friends and family for their continued support during my PhD, and especially thanks to my partner, Louise Simone Jensen, for supporting me even in my most absent-minded moments and when I stay up late at night to finish a piece of programming code for simulations. Also a special thanks to my brother, Jesper Rishøj Thomsen, for proof reading a large part of the thesis. In addition, I would like to thank Søren Jacob Brun and René Petersen for an especially pleasant office environ-

ment as well as for useful and fun discussions about anything, sometimes even physics. I also thank them both, and Farzad Bonabi, for helping me clear my head with very entertaining table tennis matches in the basement when my code is not working properly or I simply need a break.

Morten Rishøj Thomsen
Aalborg University, September 9, 2016

Chapter 1

Introduction

Graphene is a single layer of atomic carbon in a hexagonal lattice configuration and can as such be viewed as a single layer of graphite. For a long time, this material was though not to exist, since the brilliant L. D. Landau [1] in 1937 showed theoretically that infinite and purely 2D systems cannot exist[1]. In an effort to calculate the properties of graphite, P. R. Wallace [3] calculated the band structure of a single, decoupled layer of graphite, now known as graphene, already in 1947. Since graphene was thought not to exist at the time, the theory of graphene was used only to explain the model of graphite. Wallace, however, discovered one of the most remarkable features of graphene, namely that it is a semi-metal with a linear energy dispersion at the Dirac point. The linear dispersion is exactly what gives rise to the remarkable features of graphene. The dispersion of light is also linear, thus by having a linear dispersion, electrons in graphene behave much like light. In essence, electrons in graphene behave as had they no mass, but move with a velocity about 300 times lower than that of light in a vacuum [3]. Charge carriers in graphene are therefore often referred to as massless Dirac fermions. The band structure and density of states of graphene is shown in Fig. 1.1 calculated using three different levels of theory, where density functional theory (DFT) is the most accurate, tight-binding (TB) is less accurate and the Dirac equation (DE) is least accurate. The figure clearly shows that the band structure is linear around the K point of the Brillouin zone in all levels of theory and also shows that the two less accurate models reproduce the DFT result at low energy.

[1]Specifically, Landau found that the fluctual displacement of atoms in two dimensional systems at non-zero temperature diverges logarithmically with the area of the system [1, 2]. However, the fluctual displacement in finite 2D systems or 2D systems on 3D substrates could remain finite, especially due to the very slow divergence of the problem.

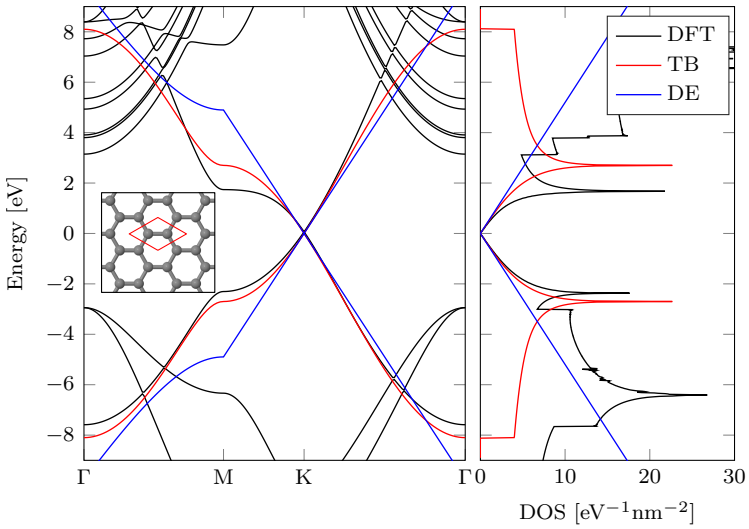

Fig. 1.1: Band structure (left) and density of states (right) of pristine graphene calculated using density functional theory (DFT), nearest-neighbor tight-binding (TB) and the Dirac equation (DE). The hopping parameter in TB and DE is taken as $\gamma = 2.7$ eV. The atomic structure of graphene is shown in the inset with the unit cell outlined in red.

Graphene was first isolated by a German group in the early 1960's [4, 5] by reduction of graphite oxide. This method is still used today as it is an affordable method for producing vast amounts of graphene, albeit of inferior quality to competing methods. Graphene was rediscovered by K. Novoselov and A. Geim in 2004 [6] by means of mechanical exfoliation of high-quality graphite, the so-called Scotch tape method, which allows for easy preparation of very high quality graphene samples. This soon created a boom of graphene-based research. According to Web of Science, more than 18,000 papers with 'graphene' in the title was published last year alone. In 2010, the Nobel prize in physics was awarded to Novoselov and Geim "for groundbreaking experiments regarding the two-dimensional material graphene" [7]. From a nanoelectronic standpoint, some of the most interesting features of graphene are its experimentally observed ultrahigh mobility of up to 1 000 000 cm^2/Vs [8], ballistic transport over more than 15 μm [8] and spin relaxation length up to 200 μm [9].

Pristine graphene is semi-metallic and is therefore not well-suited for semiconductor applications, such as field-effect transistors (FETs) and diodes. A large number of methods for opening a band gap in graphene have been proposed, including graphene nanoribbons (GNRs) [10–13], gated bilayer graphene

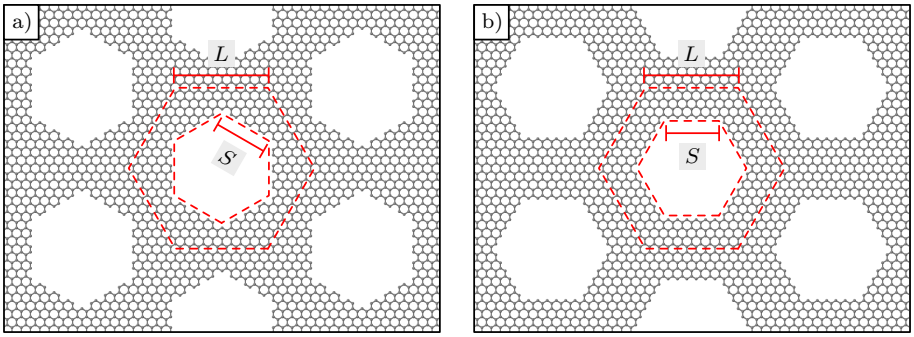

Fig. 1.2: Graphene antidot lattices with a) armchair and b) zigzag antidot edge chirality in a triangular lattice. The unit cell and antidots are outlined in red. The notation $\{L, S\}$ is commonly used to refer to an antidot lattice with unit cell side length L and antidot side length S in units of the graphene lattice constant.

[14–16], gated trilayer graphene [17], periodic electrostatic gating [18], uniaxial strain [19, 20], patterned hydrogen adsorption [21] and induced by substrate [22, 23]. The primary focus in this thesis is on another promising method for opening a band gap, namely by means of creating periodic perforations in an otherwise pristine graphene sheet, known as graphene antidot lattices (GALs) or graphene nanomeshes. The structure of two GALs with different antidot edge chiralities is shown in Fig. 1.2, along with an outline of the unit cell. GALs were first proposed by Pedersen *et al.* [24] and has been widely studied since, both theoretically [25–42] and experimentally [43–57]. One of the advantages of GALs is that the band gap can be tuned by geometrical factors. It is therefore possible to envision a nanoelectronic device made completely of graphene, where metallic regions are made from pristine graphene and semiconducting regions are made from GALs.

A universal band gap opening rule for graphene antidot lattices was developed by Dvorak *et al.* [40], showing that only one ninth of all possible GAL configurations are semiconducting while the rest are semi-metallic. An important subclass of GALs is one where both lattice vectors are strictly in armchair directions, which has the remarkable property that they all have (sizable) band gaps. Of course, this rule only applies for perfect periodic structures. Transport gaps have been observed several times in experiments [43, 45, 47, 49], where control of chirality is not so high that it is possible to actively choose among the one ninth of GALs that should have a band gap.

Several methods have been used to fabricate GALs experimentally, including e-beam lithography [44, 45, 47, 58], diblock copolymer templates [43, 46, 49], anodic aluminum oxide templates [51], nanosphere lithography [50], nanoim-

print lithography [56] and self-assembly of a precurser molecule [57]. The antidots range in size between subnanometer to several hundred nanometers in diameter, depending on the fabrication method. The antidots synthesized with top-down methods are often approximately round, but it has been demonstrated experimentally that armchair and zigzag edges in GALs are stable and can be synthesized selectively [48, 58–60], which can lead to ordered hexagonal or triangular antidots with well-defined edge chirality. Theoretical studies based on DFT show that the preferred edge chirality of GNRs is armchair in an oxygen-rich atmosphere and zigzag for water-saturated GNRs [61]. Although there may still remain some edge roughness, these findings show that the chirality of the edges of GNRs and GALs is controllable. Recent experimental studies of transport in GAL-based FETs have shown on/off ratios in the range between 4 and 100 [49, 51, 56]. These values are still too low for logic applications [62], but the results are important indicators that devices based on GALs could be used to make efficient transistors.

The electronic transport properties of GALs have also been studied theoretically. The transport through graphene antidot barriers (GABs), i.e. 1D periodic antidot structures in an otherwise pristine sheet of graphene, has previously been studied for small systems using a TB formalism [29, 37]. These studies showed that just a few antidots in the unit cell of the GAB is sufficient to suppress the transport within the band gap region. The electronic transmission of GABs can also be expressed on closed form using the DE [42] when the band gap is known in advance, which allows for easy calculation of the transport properties. Suppression of transport in antidot regions has also been used to model electronic waveguides [28], where a transport channel is kept pristine, while the rest of the structure is a GAL. Interestingly, their results show that GAL waveguides have higher conductance than corresponding graphene nanoribbons. Furthermore, Berreda *et al.* [63] have simulated three different graphene FETs based on GALs with band gaps of about 500 meV. They showed that their simulated devices had on/off ratios as high as 7400, which is close to that of silicon based MOSFETs that have on/off ratios on the order of 10^4 to 10^7 [62].

The remarkable electronic properties of graphene and its derivatives additionally make graphene interesting for spintronic applications. Carbon-based spintronic devices may have a distinct advantage over many other materials in that carbon has a very low spin-orbit coupling together with an absence of hyperfine interaction in the predominant ^{12}C isotope. This results in long spin lifetimes [64–66], as well as large spin relaxation lengths, which have been found to be on the order of several microns at room temperature [64–67] and

make graphene ideal for ballistic spin transport [68].

Pristine graphene is non-magnetic, but several suggestions on how to give graphene magnetic properties have been put forward. DFT calculations have shown that ferromagnetism can be introduced in graphene by e.g. semi-hydrogenation [69], adding vacancies [70, 71] or adding adatoms [71–76]. Semi-hydrogenating graphene sheets, where one sublattice is fully hydrogenated, while the other is not, leads to a sublattice imbalance, which induces a magnetic moment of 1 μ_B per unit cell [69]. Ferromagnetism can also be induced by transition metal adatoms on graphene or in graphene vacancies. For instance, Fe is a common magnetic impurity in graphene, which is introduced by left-over Fe residue on the graphene surface after a common process of transferring CVD-grown graphene from copper to another substrate. The Fe can then reside on the surface or be incorporated into graphene vacancies or perforations. Theoretical studies have shown that the spin moment of Fe is greatly reduced only when the Fe-C distance is short [73–75], but is largely unaffected by the presence of carbon otherwise [72–75, 77]. Trapping larger Fe clusters in graphene perforations will lead to a larger spin moment, which combined with the electrical properties of graphene, might make this a suitable system for graphene-based spintronics.

Experimentally, trapping of Fe atoms in graphene vacancies [76, 78] or perforations [79] have both been achieved by e-beam irradiation. The electron beam mobilizes Fe atoms on the graphene surface, which move until they are trapped by a vacancy or a perforation. Zhao *et al.* [79] showed that Fe atoms trapped in a graphene perforation form a monolayer Fe membrane with an approximately square lattice and a lattice constant of about 2.65 Å. This finding is surprising since the most stable arrangement of freestanding monolayer Fe is triangular with a lattice constant of about 2.45 Å. Therefore, the observed square lattice must form due to interaction with the surrounding graphene lattice.

Spin transport in graphene has attracted a lot of attention in recent years due to very long spin relaxation times and spin relaxation lengths predicted for this material [64, 80]. The spin relaxation length λ_s is related to spin lifetime τ_s by $\lambda_s = \sqrt{D_s \tau_s}$, where D_s is the spin diffusion coefficient. Theory predicts the spin lifetime in graphene to be approximately 1 μs [64] and a typical value of the spin diffusion coefficient in experiments is $D \gtrsim 2 \times 10^{-2}$ m^2/s [64, 81], which leads to a spin relaxation length of $\gtrsim$450 μm. Experimental values are typically much lower, with values of around 1–4 μm [67, 82–86], but has been observed as large as around 200 μm in short samples at low temperature [9] and 12 μm in encapsulated graphene at room temperature

[65]. It has been ruled out experimentally that this discrepancy is due to hyperfine interactions with the naturally occurring ^{13}C isotope in graphene [85]. Experimental measurements of graphene in the presence of a strong magnetic field show that the observed low spin relaxation length is, at least in part, due to magnetic impurities in graphene [87]. An attempt to explain the effects of magnetic impurities in graphene has been given by Kochan *et al.* [88]. They find that 0.36 ppm coverage of hydrogen adatoms is sufficient to obtain spin relaxation times that are in agreement with experiments. Their model is based on the Green's function of a single hydrogen adatom in an infinite graphene sheet and multiplying the results with the impurity concentration. In effect, their model does not include interference effects between scatterers and is thus only valid in the highly dilute limit. Spin transport in hydrogenated graphene was also considered by Soriano *et al.* [89, 90]. Their method is based on a mean-field Hubbard Hamiltonian and the real space Kubo-transport formalism. They find that a coverage of 15 ppm hydrogen adatoms gives the correct order of magnitude of the spin relaxation time [90], which is more than an order of magnitude larger than the prediction by Kochan *et al.* Additionally, the energy dependence of the two theoretical predictions for the spin relaxation time do not agree with the experimental findings.

Recent magnetotransport experiments have demonstrated that ballistic transport is possible in GALs [52, 53], which gives rise to interesting phenomena such as magnetoresistance oscillations due to cyclotron orbits that are commensurate with the antidot lattice. Ballistic transport in pristine graphene has been demonstrated several times and even at room temperature [8, 91–95], but ballistic transport in GALs has previously been hindered by defects introduced by top-down fabrication of the antidots. The recent demonstrations [52, 53] of ballistic transport in GALs were achieved by minimizing interaction with the substrate by using hexagonal boron nitride (hBN) substrates and by reducing edge roughness by encapsulating the graphene flake in hBN before etching the antidot lattice [53].

Previous theoretical studies on nanostructured graphene in magnetic fields have primarily focused on the DOS and optical properties [33, 96–98]. The DOS of a structure under a magnetic field reveals a self-similar structure known as Hofstadter's butterfly [99]. In particular, Hofstadter butterflies of GALs have revealed band gap quenching induced by perpendicular magnetic fields [33]. Transport calculations have yet to reveal if band gap quenching also gives rise to quenching of the transport gap. Using the DE, perforations in a graphene sheet are modeled as local mass terms rather than potentials. Within this description, it has been demonstrated that a single graphene antidot sup-

ports localized edge states in the presence of magnetic fields [98]. Magnetic edge states occur when the electron wave interferes constructively with itself in a pinned orbit around the antidot, which gives rise to Aharonov-Bohm-type oscillations. In conventional semiconductors, such as GaAs, Aharonov-Bohm oscillations due to antidots in two-dimensional electron gases have been studied theoretically [100–102] and observed experimentally [103–105]. Magnetic edge states are likewise predicted to be present in GALs and due to the long phase-coherence length in graphene, these are expected to be observable in experiments as well. Cyclotron orbits were recently imaged in pristine graphene using cooled scanning probe microscopy [106, 107]. It would be remarkable if this technique could be used for direct observation of magnetic edge states in graphene antidots.

1.1 This thesis

The main goal of this thesis is to obtain a theoretical understanding of nanostructured graphene, with a focus on transport properties. In the thesis work, there has been a great focus on numerical simulations of very large systems in order to close the gap between experiments and theory. To that end, a considerable effort is made on formulating methods based on the DE, which leads to calculations times that are scale invariant and as such allows for calculations on arbitrarily large structures. For the same reason, the computational complexity of the presented methods will also be discussed.

DFT is used for electronic structure calculations in paper IV and for structural relaxation of atomic systems in paper III. In DFT, the wave function is typically written in a basis of plane waves. The wave function is then computed self-consistently using the Kohn-Sham equations. DFT is an *ab initio* method, which means that prior knowledge of the system is, in principle, not necessary in order to perform the calculations. However, DFT is very computationally demanding and is therefore only used for relatively small systems in the thesis work, typically systems with less than 100 atoms.

In order to handle larger systems, TB is used to calculate electronic structure and electronic transport in papers I, II, IV and V. In the TB approximation, the wave function is written as a linear combination of atomic orbitals. Coupling is assumed only between nearby orbitals and it is common to only include interactions up to 1st nearest or 3rd nearest neighbors. TB is much faster than DFT, and the resulting Hamiltonian is typically extremely sparse, which often makes it possible to greatly reduce calculation time by using methods which utilize this fact. Using such methods, the TB formalism is capable

of handling systems with hundreds of thousands of atoms. Electronic transport calculations in the TB framework is carried out using the non-equilibrium Green's function (NEGF) formalism, which is a widely used method for calculating quantum transport in nanoscale devices [28, 29, 37, 38, 108–113]. In the thesis work, the NEGF formalism is coupled with the recursive Green's function (RGF) method [113], which greatly reduces calculation time, without sacrificing accuracy.

Experimentally feasible graphene antidot structures are typically too large to handle with traditional atomistic models, such as TB and DFT. For example, a 1 μm $\times$ 1 μm graphene device contains more than 30 million atoms. Models based on the DE are in the continuum regime and are therefore able to handle arbitrarily large structures. The feasibility of DE-based models is explored in papers I and II by comparing electronic band structures, optical conductivity and electronic transport in graphene antidot-based systems between the DE and TB models. In the DE-based models, the graphene antidot systems is modeled with a spatially varying mass term, which is non-zero only inside the antidot regions. The mass term makes it unfavorable for charge carriers to occupy the antidot regions. In order to differentiate between size related effects and edge chirality effects, the calculations are based on hexagonal antidots with edge chiralities that are either purely armchair or purely zigzag.

In order to calculate electronic band structures and optical properties in paper I, the wave function and mass term is written as Fourier series. This allows for formulating the problem as an eigenvalue problem that can be solved numerically, which can then be used to calculate electronic band structures, density of states and optical conductivity. Both the electronic band structure and the optical conductivity is found to be in good agreement with TB in absence of localized edge states, which occur for antidots with extended zigzag edges.

Electronic transport in GALs can be treated as a scattering problem, using techniques similar to those used in optics, where the scattering of an incident electron wave on a graphene antidot structure is calculated. This is done in in paper II by using a Green's function method, which is a method widely used to solve similar scattering problems in optics. The DE has previously been used to calculate scattering of Dirac electrons on a single circular mass barrier [114], a single circular electrostatic barrier [115] and simple 1-dimensional barriers of constant and finite mass [42]. The advantages of the presented approach are that it works for any antidot shape and for any arrangement of antidots, even periodic. The presented results are based on graphene antidot barriers (GABs), i.e., GAL barriers of infinite width and finite length, see Fig. 1.3. Calculating

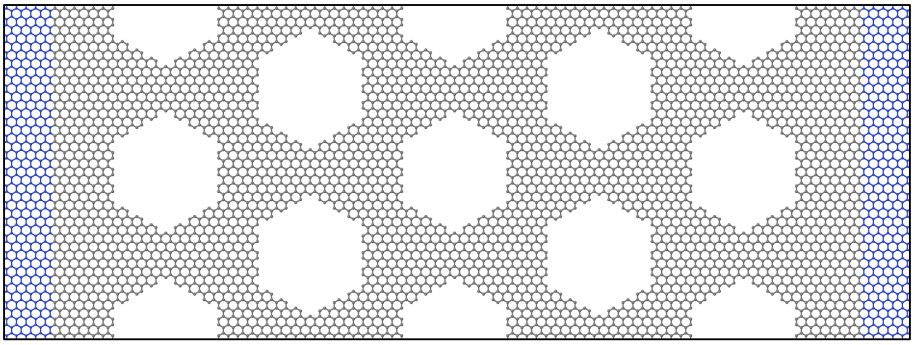

Fig. 1.3: Graphene antidot barrier, a GAL barrier of infinite width and finite length. All atoms are carbon. The gray atoms represents the barrier region and the blue atoms represents semi-infinite pristine graphene regions.

the scattering on a periodic system allows for determining the transmission probability, which is directly related to the conductance. Not surprisingly, the electronic transport in the DE is found to be in good agreement with TB in absence of localized edge states as was also found for the electronic structure. At the present time, the DE-based method of calculating electronic transport does include the possibility of an applied magnetic field, nor does it extend to include impurities. Therefore, the TB approximation is used instead in order to treat systems with magnetic defects in paper IV or graphene antidot lattices under a magnetic field in paper V. The magnetotransport properties of GABs in different lattice geometries is studied in paper V. The TB results are compared to both an ideal Dirac mass barrier (DMB) and a gapped graphene model. DMBs are found to provide a good description of the transport gap for GABs with small antidots provided the magnetic field is not too strong. Furthermore, evidence of magnetic edge states on the antidots is demonstrated. Simple scaling of these states allows for predictions for larger systems. Finally, the transmittance of disordered GABs is calculated and compared to the corresponding transmittance in ordered GABs.

The spin relaxation length in graphene is much lower than expected. It was determined experimentally that the low relaxation length is, at least in part, due to magnetic impurities. It is therefore important to understand the spin relaxation mechanism in graphene in the presence of magnetic impurities. One of the simplest and most common magnetic impurities in graphene are hydrogen adatoms, which carry a magnetic moment of 1 μB per atom. The spin-dependent electronic transport of graphene with hydrogen adatom is calculated in paper IV. The calculations are based on hydrogen adatoms, but

some the findings are expected to be general for magnetic defects in graphene. Spin relaxation due to random uncorrelated scattering events is referred to as Markovian spin relaxation and gives rise to an exponentially decaying spin polarization. It is demonstrated that the spin relaxation is not always Markovian and that inverse spin relaxation length scale nearly linearly with impurity concentration.

Another common type of magnetic impurities are Fe atoms, which are left over from the transfer technique commonly used to transfer CVD-grown graphene samples from a copper substrate to another substrate (typically a plastic, such as PMMA). It was shown experimentally by Zhao *et al.* that this left-over Fe can form monolayer membranes embedded in graphene perforations. A DFT analysis of the structural stability and magnetization of free-standing and graphene-embedded monolayer Fe is presented in paper III in an attempt to obtain a basic understanding of these as well as to explain the experimental findings. In particular, the stability of Fe in square and triangular lattice configurations is compared for both free-standing monolayer Fe and monolayer Fe embedded in graphene perforations. The Fe membranes are modeled as periodic systems, effectively giving rise to GALs, where the antidots are filled with Fe. It is possible that the embedding of Fe in graphene perforations in experiments can be scaled up to actual Fe filled GALs. The magnetization of the iron membranes coupled with the electronic properties of graphene may make this an interesting platform for spintronics.

Chapter 2

Theory and methods

This chapter will introduce the computational methods used in the thesis work, as well as introduce some of the used theory. The primary focus in this chapter is theory and methods that are only explained rudimentarily in the papers. Moreover, previously unpublished analytical approximations to the band gap and transport gap of graphene antidot lattices (GALs) will be derived. Many of the published results are based on electronic structure calculations using either density functional theory (DFT) or tight binding (TB). DFT is in general more accurate than TB, but the latter allows for calculations for considerably larger systems. In order to handle even larger systems, methods based on the Dirac equation are derived. The advantage of doing this is that computational complexity becomes scale invariant and therefore makes it possible to calculate properties of arbitrarily large systems.

2.1 Density functional theory

The theory of quantum mechanics was established already in the 1920s. At this time, the theory was rather limited, since no analytical solutions exist for the many-body system such as molecules and solid state matter. With the advent of transistor-based computers in the 1950s and 1960s, the search quickly went on to finding numerical approximations to this problem. Probably the most successful *ab initio* computational quantum mechanics method is DFT owing to its numerical performance. *Ab initio* refers to the property that a method does not depend on any external fitting parameters and therefore does not require any previous knowledge of the system. The groundwork for DFT was laid in the 1960s by Kohn and coworkers [116, 117]. First, the dimensionality

of the N-body problem is reduced from $3N$ to 3 by restating it in terms of the electronic density instead of the many-body wave function [116]. Second, all particle-particle interactions are replaced by an *exchange-correlation* potential [117], thereby drastically reducing the complexity of the problem. The functional form of the exchange-correlation potential is not known analytically and is therefore guessed upon and typically fitted to known solutions of the homogeneous electron gas. The quality of this functional is therefore paramount to the accuracy of the solution and it is therefore important to choose it carefully. The derivation of DFT relies on the variational principle, which means that only the ground state is accurate. Note that DFT is in principle exact given that the exact exchange-correlation is used and a self-consistent solution is found. In the thesis work, the freely available DFT package `ABINIT` [118, 119] is used for structural relaxation and electronic structure calculations.

2.2 Tight-binding

The TB model is a relatively simple model for quantum mechanics calculations. It can be used to extract properties like electronic structure, density of states, optical properties and electronic transport. It is computationally significantly faster than *ab initio* methods like DFT, which makes it possible to calculate properties of systems with size vastly exceeding what is possible within the DFT framework. Since TB is not *ab initio* it relies on external fitting parameters, which are often determined by fitting a band structure against DFT. If experimental data is available, these may also be used to aid the fit. A well-fitted TB model has a relatively high accuracy. A nearest-neighbor TB model can, for instance, accurately describe the low-energy electronic structure of graphene [120].

In the TB model, the molecular wave function is approximated by a linear combination of atomic orbitals centered around the atomic sites of the lattice. Most of the interesting properties of a material depend on the electronic states near the Fermi energy. This can be taken advantage of in TB by only including atomic orbitals that contribute to the energy spectrum near the Fermi level. In graphene, this means the model can be restricted to only one atomic orbital per atomic site, namely a single p_z orbital. The reason for this is that the p_z orbital is responsible for most observed quantities and it does not interact with the p_x, p_y and s orbitals due to symmetry.

In TB, the Hamiltonian $\hat{H}$ can be written in first quantization notation as

$$\hat{H} = \sum_{i<j} t_{ij}(|i\rangle\langle j| + \text{H.c.}) + \sum_i \varepsilon_i |i\rangle\langle i|, \tag{2.1}$$

where $|i\rangle$ is an orbital located on a given lattice site and t_{ij} is the hopping parameter between orbital $|i\rangle$ and $|j\rangle$, and ε_i is the on-site potential of orbital $|i\rangle$. In general, the notation $|i\rangle$ covers both lattices sites and orbital type. As stated earlier, the most common choice for graphene is to only take one p_z orbital for each atomic site. The Hamiltonian is inserted in the Schrödinger equation $\hat{H}\Psi = E\Psi$ and the eigenvalues are then solutions to the equation $\det(\boldsymbol{H} - \boldsymbol{S}E) = 0$, where $\boldsymbol{H}$ is the Hamiltonian on matrix form with matrix elements $H_{ij} = \langle i|\hat{H}|j\rangle$ and $\boldsymbol{S}$ is the overlap matrix with matrix elements $S_{ij} = \langle i|j\rangle$. In the low-energy regime, it is often sufficient to only let t_{ij} be non-zero for nearest neighbors, letting $S_{ij} = \delta_{ij}$ and letting $\varepsilon_i = 0$ [120, 121]. Common choices for the nearest neighbor hopping parameter are $t_{ij} = -3.033$ eV [121] and $t_{ij} = -2.7$ eV [120]. The computational complexity of calculating eigenvalues by direct diagonalization is $\mathcal{O}(N^3)$, where N is the total number of orbitals included in the model. This means that the calculation time scales cubicly with the number of atoms used in the model. However, the complexity can be decreased by taking advantage of the fact that the TB Hamiltonian typically is extremely sparse. Among these methods are the Haydock [122], the kernel polynomial [123, 124] and the recursive Green's function (RGF) [113] methods. The RGF method is used extensively in the thesis work and is described in more detail in Sec. 2.4.

2.3 Dirac equation-based models

In this section, the DE-based models to calculate electronic structure and transport of graphene antidot systems will be introduced. These models are based on a real-space representation of the Dirac equation, which in turn is based on a low-energy approximation to the TB Hamiltonian of graphene. The advantage of the DE models is that the computational complexity turns out to be scale invariant, thus allowing for calculations of arbitrarily large systems.

2.3.1 Gapped graphene

As mentioned earlier, there are several strategies to open a band gap in graphene. Gapped graphene is a simple mathematical model describing the behavior of graphene with a band gap. This is achieved by introducing a sublattice imbalance between the two carbon atoms in the graphene unit cell by shifting the on-site energies of the atoms by Δ on one sublattice and $-\Delta$ on the other.

In the nearest neighbor tight-binding description, this give rise to the following Hamiltonian

$$\boldsymbol{H} = \begin{pmatrix} \Delta & -\gamma h(\boldsymbol{k}) \\ -\gamma h(\boldsymbol{k})^* & -\Delta \end{pmatrix}, \tag{2.2}$$

where $h(\boldsymbol{k}) = e^{ik_x a_0/\sqrt{3}} + 2e^{-ik_y a_0/2\sqrt{3}} \cos(k_x \sqrt{3} a_0/2)$. In the orthogonal approximation (that is, the overlap integrals are $s_{ij} = \delta_{ij}$), this has eigenvalues

$$E = \pm\sqrt{|h(\boldsymbol{k})|^2 \gamma^2 + \Delta^2}. \tag{2.3}$$

At the K-point of the Brillouin-zone, $|h(\boldsymbol{K})| = 0$, so the energies are simply $E(\boldsymbol{K}) = \pm\Delta$, and the band gap is therefore $E_g = 2\Delta$. In the Dirac approximation, the first order series expansion of $\gamma h(\boldsymbol{k})$ around $\boldsymbol{K}$ is used, which is given by $\gamma h(\boldsymbol{k}) \approx \hbar v_F(-k_x + ik_y)$, where the redefinition $\boldsymbol{k} - \boldsymbol{K} \to \boldsymbol{k}$ has been used on the right-hand side. Here, $v_F = \sqrt{3} a_0 \gamma / 2\hbar$ is the Fermi velocity. The Hamiltonian then becomes

$$\boldsymbol{H} = \begin{pmatrix} \Delta & \hbar v_F(k_x - ik_y) \\ \hbar v_F(k_x + ik_y) & -\Delta \end{pmatrix} \tag{2.4}$$

with eigenvalues

$$E(\boldsymbol{k}) = \pm\sqrt{\hbar^2 v_F^2 k^2 + \Delta^2}, \tag{2.5}$$

where $k = |\boldsymbol{k}|$. The band gap is obviously still $E_g = 2\Delta$. It is straightforward to show that the density of states of the gapped graphene model is $D(E) = 2|E|\theta(|E| - \Delta)/\hbar^2 v_F^2 \pi$. Due to the simplicity of this model, it is often used for comparison against more rigorous models.

2.3.2 Electronic structure

As stated above, the gapped graphene model is only a mathematical method for introducing a band gap. A physical method for introducing a band gap is GALs, i.e., periodic perforations in an otherwise pristine graphene sheet as shown in Fig. 1.2. GALs can be modeled in several ways. Here, a continuum model is presented, where the antidot is taken into account by a spatially varying mass term, which is non-zero only inside the antidot regions. The mass term effectively excludes charge carriers from the antidot regions at energies near the Fermi level, and is thus reminiscent of actual antidots.

The model is based on the Dirac Hamiltonian, Eq. (2.4). Since the mass term is varying in real space, the Hamiltonian must be converted to real space, which is done by writing it on differential form

$$\hat{H} = \begin{pmatrix} \Delta(\boldsymbol{r}) & -\hbar v_F(i\partial_x - \partial_y) \\ -\hbar v_F(i\partial_x + \partial_y) & -\Delta(\boldsymbol{r}) \end{pmatrix}. \tag{2.6}$$

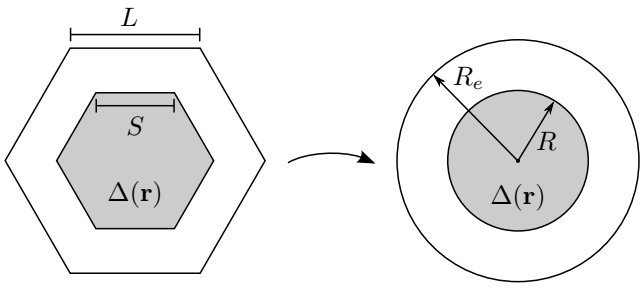

Fig. 2.1: The hexagonal unit cell and the antidot are replaced by circles of equivalent areas with radii of R_e and R, respectively.

The wave function must then satisfy the Dirac equation $\hat{H}\Psi = E\Psi$. This can be written on matrix form by writing both the mass term and the wave function as Fourier series expansions, which gives rise to the equation $\boldsymbol{H\Psi} = E\boldsymbol{\Psi}$ with matrix elements

$$\boldsymbol{H}_{\boldsymbol{G},\boldsymbol{G}'} = \begin{pmatrix} \Delta_{\boldsymbol{G}-\boldsymbol{G}'} & T_{\boldsymbol{G}}\delta_{\boldsymbol{G},\boldsymbol{G}'} \\ T^*_{\boldsymbol{G}}\delta_{\boldsymbol{G},\boldsymbol{G}'} & -\Delta_{\boldsymbol{G}-\boldsymbol{G}'} \end{pmatrix}, \tag{2.7}$$

where $\Delta_{\boldsymbol{G}-\boldsymbol{G}'}$ are the Fourier coefficients of the mass term and $T_{\boldsymbol{G}} = \hbar v_F[k_x + G_x - i(K - y + G_y)]$. The Fourier coefficients of arbitrary N-sided polygons are given in Ref. [125]. For a circular antidots with radius R, the Fourier coefficients are given by $\Delta_{\boldsymbol{G}} = 2\pi\Delta_0 R J_1(|\boldsymbol{G}|R)/A_{uc}|\boldsymbol{G}|$, where A_{uc} is the area of the unit cell and $J_1(x)$ is the first order Bessel function of the first kind. The electronic structure, density of states and optical conductivity of GALs can then be calculated by solving this as an eigenvalue problem. The computational complexity of the method is $\mathcal{O}(N_G^3)$, where N_G is the number of reciprocal lattice vectors used in the model. Importantly, the number of reciprocal lattice vectors needed for convergence does not increase with system size and the method is therefore scale invariant.

Further, the model is used to derive an analytical expression of the band gap of graphene antidot lattices. The derivation here is done in a slightly different way than in Paper I, which leads to a much nicer intermediate result. First, cylindrical symmetry is obtained by replacing both the unit cell and the antidot by circles of equivalent areas as shown in Fig. 2.1.

The radii of the unit cell and antidots are denoted $R_e = \sqrt{A_{tot}/\pi}$ and $R = \sqrt{A_{rem}/\pi}$, respectively. It was found in the paper that the energy (given by $E = \hbar v_F k$) should satisfy

$$J_1(kR_e)[Y_0(kR) + Y_1(kR)] - Y_1(kR_e)[J_0(kR) + J_1(kR)] = 0 \tag{2.8}$$

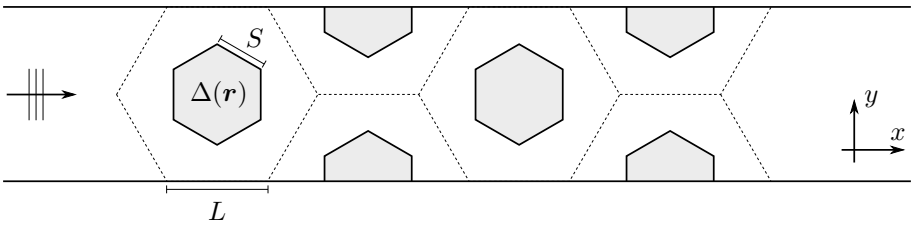

Fig. 2.2: Graphene antidot barrier unit cell used when calculating electronic transport with the DE-based approach. The mass term $\Delta(\boldsymbol{r})$ is set to Δ in the gray regions and is vanishing elsewhere. The dashed gray lines show an example of discretization of the system into small area elements.

at the Γ-point. In the paper, the first order series expansion of each of the Bessel function is taken individually[1]. Here, the series expansion of the entire equation is taken to 2nd order around $k = 0$, which gives rise to

$$4R + 2kR^2 - k^2R^3 - 2kR_e^2 + k^2RR_e^2 + 2k^2RR_e^2 \ln\frac{R}{R_e} = 0. \tag{2.9}$$

Solving this equation for the band gap $E_g = 2\hbar v_f k$ gives

$$E_g \simeq \frac{8\hbar v_F R}{R_e^2 - R^2 + \sqrt{5R^4 + R_e^4 - 2R^2R_e^2(3 + 4\ln R/R_e)}} \tag{2.10}$$

$$= \frac{8\hbar v_F\sqrt{\pi A_{rem}}}{A_{tot} - A_{rem} + \sqrt{5A_{rem}^2 + A_{tot}^2 - 2A_{rem}A_{tot}(3 + 2\ln A_{rem}/A_{tot})}}. \tag{2.11}$$

This expression turns out to be remarkably accurate, especially for armchair antidots. In the limit of small R, the expression reduces to

$$E_g \approx 4\hbar v_F \frac{R}{R_e^2} = 4\hbar v_F\sqrt{\pi}\frac{\sqrt{A_{rem}}}{A_{tot}}, \tag{2.12}$$

which is the same result found in the paper.

2.3.3 Electronic transport

The idea of using a spatially varying mass term to model graphene antidots is expanded to include scattering of charge carriers in paper II, with a strong focus on electronic transport properties of graphene antidot barriers (GABs). A GAB is a GAL barrier of infinite width and finite length as illustrated in

[1] giving rise to the equation $4R + 2kR^2 - 2kR_e^2 + k^2RR_e^2 + k^2RR_e^2(2 + kR)\ln\frac{R}{R_e} = 0$, which is third order in k and does therefore not lend itself to an elegant closed-form solution.

Figs. 1.3 and 2.2. Unlike the eigenvalue method described above, this method is not restricted to treating periodic systems. The formal theory of the method is established in the paper, but there is not much attention on how to solve the equations efficiently. This section will focus on how to solve the equations efficiently using a numerical method that takes advantage of fast Fourier transforms. The scattering problem is solved by using a Green's function method, which is a method often used to solve similar problems in optics [126, 127]. In this description, the wave function can be calculated as

$$\Psi(\boldsymbol{r}) = \Psi_0(\boldsymbol{r}) + \int_{A_{UC}} \tilde{\Delta}(\boldsymbol{r}')\boldsymbol{G}(\boldsymbol{r},\boldsymbol{r}')\sigma_z\Psi(\boldsymbol{r}')d^2r', \tag{2.13}$$

where Ψ_0 is the wave function in the absence of antidots, $\tilde{\Delta}(\boldsymbol{r}) = \Delta(\boldsymbol{r})/\hbar v_F$ is the reduced mass term and $\boldsymbol{G}(\boldsymbol{r},\boldsymbol{r}')$ is the Green's function of the system. The mass term is step-wise constant with a value of Δ inside the antidot and is vanishing elsewhere. A typical unit cell used for transport calculations is shown in Fig. 2.2. In the non-periodic case, the Green's function is given by

$$\boldsymbol{G}(\boldsymbol{r},\boldsymbol{r}') = \frac{k}{4i}\begin{pmatrix} H_0^{(1)}(kr) & -ie^{-i\theta}H_1^{(1)}(kr) \\ -ie^{i\theta}H_1^{(1)}(kr) & H_0^{(1)}(kr) \end{pmatrix}, \tag{2.14}$$

where $H_n^{(1)}$ is the n'th order Hankel function of the first kind, $k = E/\hbar v_f$, $r = |\boldsymbol{r} - \boldsymbol{r}'|$ and θ is the polar angle of $\boldsymbol{r} - \boldsymbol{r}'$. In the periodic case, the Green's function $\tilde{\boldsymbol{G}}$ is given by a sum of contributions from all unit cells

$$\tilde{\boldsymbol{G}}(\boldsymbol{r},\boldsymbol{r}') = \sum_{m=-\infty}^{\infty} \boldsymbol{G}(\boldsymbol{r},\boldsymbol{r}' - m\Lambda\hat{y}) \tag{2.15}$$

$$= \sum_{m=-M}^{M} \boldsymbol{G}(\boldsymbol{r},\boldsymbol{r}' - m\Lambda\hat{y}) + \frac{k}{4i}\sum_{n=-\infty}^{\infty} i^n J_n(kr)e^{-in\theta}\begin{pmatrix} S_n & -S_{n-1} \\ -S_{n+1} & S_n \end{pmatrix}, \tag{2.16}$$

where J_n is the n'th order Bessel function of the first kind and S_n is the lattice sum given by

$$S_n = \sum_{m=M+1}^{\infty} H_n^{(1)}(km\Lambda)(e^{ik_y m\Lambda} + (-1)^n e^{-ik_y m\Lambda}). \tag{2.17}$$

This sum is actually very slowly convergent, but it can be solved efficiently by restating it on integral form [128]. On integral form, it can be solved numerically very efficiently by using, e.g., the adaptive Simpson's quadrature. The contribution of M unit cells on either side of the zeroth unit cell is taken outside

the lattice sum, as these may not satisfy the condition required by Graf's theorem, which was used to rewrite the problem in terms of lattice sums. Graf's theorem is only satisfied when the maximum distance between area elements inside one unit cell is less than $(M+1)\Lambda$, where Λ is the period.

Equation (2.13) can be solved numerically by discretization of space into small area elements δA_i with centers $\boldsymbol{r}_i$. The integral is then approximated by assuming that the mass term and wave functions are constant inside each area element and by approximating the Green's function between element i and j as

$$\boldsymbol{G}_{ij} = \begin{cases} \frac{1}{\delta A_j} \int_{\delta A_j} \boldsymbol{G}(\boldsymbol{r}_i, \boldsymbol{r}') d^2 r' & \text{if } i = j \\ \boldsymbol{G}(\boldsymbol{r}_i, \boldsymbol{r}_j) & \text{if } i \neq j \end{cases}. \tag{2.18}$$

The equation can then be restated as

$$\begin{pmatrix} \Psi^{(A)}_{i_x i_y} \\ \Psi^{(B)}_{i_x i_y} \end{pmatrix} - \sum_{j_x, j_y} \begin{pmatrix} G^{(11)}_{i_x - j_x, i_y - j_y} & G^{(12)}_{i_x - j_x, i_y - j_y} \\ G^{(21)}_{i_x - j_x, i_y - j_y} & G^{(22)}_{i_x - j_x, i_y - j_y} \end{pmatrix} \begin{pmatrix} \Psi^{(A)}_{j_x j_y} \\ -\Psi^{(B)}_{j_x j_y} \end{pmatrix} \tilde{\Delta}_{j_x j_y} \delta A \approx \begin{pmatrix} \Psi^{(A)}_{0, i_x i_y} \\ \Psi^{(B)}_{0, i_x i_y} \end{pmatrix}. \tag{2.19}$$

A typical way of solving a system like this is to write it on matrix form $\boldsymbol{A}\boldsymbol{\Psi} = \boldsymbol{\Psi}_0$ and then simply inverting the matrix to find the self-consistent solution for $\boldsymbol{\Psi} = \boldsymbol{A}^{-1}\Psi_0$. This certainly works, but the computational complexity is quite bad. For a regular $N_x \times N_y$ grid, the matrix is of size $(2N_xN_y) \times (2N_xN_y)$ and the computational complexity is then $\mathcal{O}(N_x^3 N_y^3)$. In the following, it will be shown that the complexity of a conjugate gradient (CG) algorithm on this problem will have complexity of approximately $\mathcal{O}(N_x N_y \log(N_x N_y))$. There is a subtle detail to this complexity analysis, namely that the matrix inversion method only requires sampling of area elements inside the antidots, while the CG method requires uniform sampling in a rectangular region containing all the antidots in the unit cell. This means that N_x and N_y are smaller for the matrix inversion, but it does of course not fundamentally change the scaling behavior.

Equation 2.19 can be written as a matrix equation on the form $\boldsymbol{A}\boldsymbol{x} = \boldsymbol{b}$, which can be solved iteratively using, e.g., a CG method. Note the plain CG algorithm only works for real, symmetric matrices, and $\boldsymbol{A}$ in this case is neither. The specific CG method that will be used here is the BiConjugate Gradient STABilized (BiCGSTAB) algorithm, which is relatively fast, numerically stable and works for non-symmetric complex matrices. The algorithm is detailed in Refs. [129, 130] and will be outlined here. The algorithm starts with an initial guess $\boldsymbol{x}_0$, setting $\rho_0 = \alpha = \omega_0 = 1$ and $\boldsymbol{v}_0 = \boldsymbol{p}_0 = \boldsymbol{0}$. Then, the residual of the initial guess is calculated $\boldsymbol{r}_0 = \boldsymbol{b} - \boldsymbol{A}\boldsymbol{x}_0$. The following equations are then

looped until convergence ($i = 1, 2, 3, \ldots$)

$$\begin{aligned}
\rho_i &= \boldsymbol{r}_0^\dagger \boldsymbol{r}_{i-1} \\
\beta &= (\rho_i/\rho_{i-1})(\alpha/\omega_{i-1}) \\
\boldsymbol{p}_i &= \boldsymbol{r}_{i-1} + \beta(\boldsymbol{p}_{i-1} - \omega_{i-1}\boldsymbol{v}_{i-1}) \\
\boldsymbol{v}_i &= \boldsymbol{A}\boldsymbol{p}_i \\
\alpha &= \rho_i/(\boldsymbol{r}_0^\dagger \boldsymbol{v}_i) \\
\boldsymbol{s} &= \boldsymbol{r}_{i-1} - \alpha \boldsymbol{v}_i \\
\boldsymbol{t} &= \boldsymbol{A}\boldsymbol{s} \\
\omega_i &= (\boldsymbol{t}^\dagger \boldsymbol{s})/(\boldsymbol{t}^\dagger \boldsymbol{t}) \\
\boldsymbol{x}_i &= \boldsymbol{x}_{i-1} + \alpha \boldsymbol{p}_i + \omega_i \boldsymbol{s} \\
\boldsymbol{r}_i &= \boldsymbol{s} - \omega_i \boldsymbol{t}.
\end{aligned}$$

A typical error measure in CG methods is

$$\eta = \frac{\boldsymbol{r}_i^\dagger \boldsymbol{r}_i}{\boldsymbol{x}_i^\dagger \boldsymbol{x}_i}. \tag{2.20}$$

which is simply the Euclidean norm of the residual divided by the Euclidean norm of the current approximation to the solution. Convergence is then reached when η is below some tolerance, which is chosen as 10^{-6} in the calculations. In a previous implementation, the incomplete LU decomposition-conjugate gradient (ILUCG) method [131, 132] was used instead, but the convergence of this method on this problem was found to be erratic, especially at high energies[2]. This shows that the specific CG method used in the implementation can be very important for convergence speed and there may even exist variations which converge faster than the BiCGSTAB algorithm.

The best case complexity (convergence reached after one iteration) of this algorithm is $\mathcal{O}(N_x^2 N_y^2)$. While this certainly looks better than the matrix inversion complexity, the CG method may actually not improve a lot on the calculation time if convergence is slow.

The trick to make computation faster relies on the observation that the sum in Eq. (2.19) is simply a discrete convolution. A convolution $(f * g)(x)$ can be computed using Fourier transforms as

$$(f * g)(x) = \mathcal{F}^{-1}\{\mathcal{F}\{f\} \circ \mathcal{F}\{g\}\}, \tag{2.21}$$

[2]The typical number of iterations of a system with 4 antidots in the unit cell is about 40 – 60 for the BiCGSTAB algorithm and 300 – 5000 for the ILUCG algorithm for an antidot area fraction of 30 % and 70 – 130 compared to 700 – 35,000 for an area fraction of 50 %.

where $\mathcal{F}$ denotes the Fourier transform, $\mathcal{F}^{-1}$ denotes the inverse Fourier transform, "$*$" represents a discrete convolution and "$\circ$" represents element-wise multiplication. The Fourier transform can then be calculated very efficiently using the fast Fourier transform (FFT).

Equation (2.19) is restated in terms of discrete convolutions

$$\boldsymbol{A} * (\delta A \tilde{\boldsymbol{\Delta}} \boldsymbol{\Psi}) = \delta_A \begin{pmatrix} A^{(11)} * (\tilde{\boldsymbol{\Delta}} \boldsymbol{\Psi}_A) & A^{(12)} * (\tilde{\boldsymbol{\Delta}} \boldsymbol{\Psi}_B) \\ A^{(21)} * (\tilde{\boldsymbol{\Delta}} \boldsymbol{\Psi}_A) & A^{(22)} * (\tilde{\boldsymbol{\Delta}} \boldsymbol{\Psi}_B) \end{pmatrix} = \boldsymbol{\Psi}_0, \tag{2.22}$$

where

$$\boldsymbol{A}_{i_x, i_y} = \begin{pmatrix} \delta_{i_x} \delta_{i_y} - G^{(11)}_{i_x, i_y} & G^{(12)}_{i_x, i_y} \\ -G^{(21)}_{i_x, i_y} & \delta_{i_x} \delta_{i_y} + G^{(22)}_{i_x, i_y} \end{pmatrix}. \tag{2.23}$$

This means that the matrix-vector products in the CG algorithm can be computed using discrete convolutions, i.e., $\boldsymbol{A}\boldsymbol{p}_i \rightarrow \boldsymbol{A} * (\delta A \tilde{\boldsymbol{\Delta}} \boldsymbol{p}_i)$ and $\boldsymbol{A}\boldsymbol{s} \rightarrow \boldsymbol{A} * (\delta A \tilde{\boldsymbol{\Delta}} \boldsymbol{s})$. A convenient consequence of writing this in terms of convolutions is that the matrix size can be reduced to $(2N_x) \times (2N_y)$ instead of the $(2N_x N_y) \times (2N_x N_y)$ necessary for matrix inversion. The complexity of computing the 2-dimensional FFT is $\mathcal{O}(N_x N_y \log(N_x N_y))$. It was found that the number of iterations needed for convergence does not depend on the number of area elements used for the discretization and it is therefore concluded that the complexity of the iterative method is equal to the complexity of computing the FFT. However, the number of iterations does depend on the area fraction of antidots, as well as the number of antidots, in the unit cell. Both the number of area elements and the number of iterations needed for convergence was not found to increase with system size and it is therefore concluded that the computational complexity is scale invariant.

2.3.4 Dirac mass barrier

A GAB can also be approximated by a simple one-dimensional mass barrier, where the the mass term is non-zero only inside the barrier, with a value equal to half the band gap of the barrier, see Fig. 2.3. This is known as a Dirac mass barrier (DMB) and has transmittance at $k_y = 0$ given by [29, 42]

$$T(E) = \frac{E^2 - \Delta^2}{E^2 - \Delta^2 \cos^2\left(\dfrac{\sqrt{E^2 - \Delta^2} d}{\hbar v_F}\right)}, \tag{2.24}$$

where $\Delta = E_g/2$ is the mass term and d is the length of the barrier.

It can be useful to calculate the transport gap of a system, which is defined here as the energy region near the Fermi level, where the transmittance is

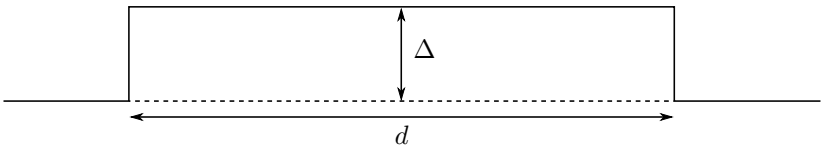

Fig. 2.3: Dirac mass barrier, a one-dimensional mass barrier of length d with a mass term of $\Delta = E_g/2$ inside the barrier and vanishing elsewhere.

strictly less than 1/2. In paper II, the transport gap of a DMB was calculated by solving Eq. (2.24) numerically. However, it is actually possible to derive an approximate analytical expression of the transport gap. The transmittance of a DMB can be estimated by the Padé approximant of order [1/1] around $E = \Delta$ of Eq. (2.24) giving

$$T(E) \approx \frac{\hbar^2 v_F^2 (15\hbar^2 v_F^2 (E-3\Delta) + 8d^2\Delta^2(\Delta - E))}{15\hbar^4 v_F^4 (E-3\Delta) + \hbar^2 v_F^2 d^2 (7E - 37\Delta)\Delta^2 + 12d^2(E-\Delta)\Delta^4}. \quad (2.25)$$

By solving for $T(\alpha) = 1/2$, the transport gap can be calculated as $E_T = 2\alpha$, which gives rise to the following expression[3]

$$E_T \approx \begin{cases} E_g + \frac{30\hbar^2 v_F^2 (d^2 E_g^3 - 4\hbar^2 v_F^2 E_g)}{23\hbar^2 v_F^2 d^2 E_g^2 + 3d^4 E_g^4 - 60\hbar^4 v_F^4}, & E_g \geq \frac{\sqrt{6(\sqrt{4969}-53)}\hbar v_F}{6d} \\ 0, & \text{otherwise} \end{cases}, \quad (2.26)$$

where the band gap E_g is given by Eq. (2.11). When $E_g < \sqrt{6(\sqrt{4969}-53)}\hbar v_F/6d$, the transmittance of the barrier never drops below 1/2 and the transport gap is therefore zero. This expression provides a rather good description of the transport gap, especially for armchair antidots.

2.4 Non-equilibrium Green's functions

The non-equilibrium Green's function (NEGF) formalism is a powerful tool for extracting physical observables from a model. An excellent introduction to the NEGF formalism is given by Datta [111] and an in-depth description of the formalism and the related recursive Green's function (RGF) method as used in graphene is given by Lewenkopf and Mucciolo [113]. An important reason for the popularity of the NEGF formalism is that it is often possible to obtain calculation times that are significantly faster than direct diagonalization by utilizing the RGF method [113]. As evident by its name, the NEGF formalism

[3] Amusingly, this only works because the approximation of the transmittance is quite bad, in the sense that it has a $1/E$ type singularity near the transport gap. However, the singularity ensures that the transmittance has a value crossing 1/2 given that $T(0) < 1/2$.

is based on Green's functions, which can be thought of as the inverse of an operator. The Green's function for the Schrödinger equation $(E - \hat{H})\Psi(r) = 0$ is the solution to the equation $(E - \hat{H})G(r, r') = \delta(r - r')$.

On matrix form and for a multilead system, as shown in Fig. 2.4, the Green's function is given by $G = (E + i\varepsilon - H - \sum_j \Sigma_j)^{-1}$, where E is the energy, $i\varepsilon$ is a small imaginary factor needed for numerical stability, H is the Hamiltonian of the system and Σ_j is known as the self-energy of lead j, which takes into account the effect of the lead on the system. It is common in the literature of the NEGF method to drop matrix notation for the symbols, but it should be understood that all symbols except E represents a matrix in the above expression. The advantage of taking the leads into account by means of self-energies makes it possible to describe a system with semi-infinite leads without having a Green's function with infinite dimensions. The self-energy of the leads are calculated using the very efficient decimation technique [113, 133]. In the thesis work, the NEGF formalism is used with a TB Hamiltonian, but it also applies, for instance, to DFT Hamiltonians.

Many important parameters can be extracted from the Green's function. Firstly, for a single orbital on each atomic site, the local (or atom-projected) density of states (LDOS) $L_i(E)$ on atom i is given by [113]

$$L_i(E) = -\frac{1}{\pi}\mathrm{Im}\{G_{ii}\} \tag{2.27}$$

and the full density of states (DOS) $D(E)$ is then the sum of all local contri-

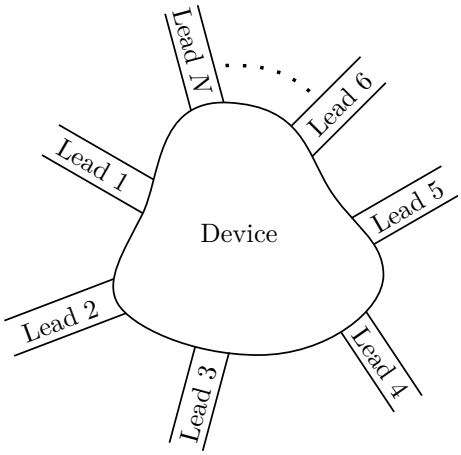

Fig. 2.4: A general device that can be modeled using the NEGF formalism, where a device region coupled to a number of leads.

butions [113]

$$D(E) = \sum_i L_i(E). \tag{2.28}$$

Further, the conductance between lead i and j of the system is given by the Landauer-Büttiker formula $G_{ij} = \frac{2e^2}{h} T_{ij}(E)$, where T_{ij} is the transmittance between lead i and j given by [113]

$$T_{ij}(E) = \mathrm{Tr}\{\Gamma_i G^\dagger \Gamma_j G\}. \tag{2.29}$$

Here, $\Gamma_i = i(\Sigma_i - \Sigma_i^\dagger)$ is the level width (or line width) function. For a two-terminal system with left (L) and right (R) leads, this give rise to a 2×2 transmittance tensor

$$\boldsymbol{T} = \begin{bmatrix} T_{L,L} & T_{L,R} \\ T_{R,L} & T_{R,R} \end{bmatrix}. \tag{2.30}$$

The elements of the transmittance tensor has exactly the meaning you would think: T_{ij} represents the number of the charge carriers injected in lead i which exists through lead j.

The terminal current at lead p is given by [111]

$$I_p = \frac{2e}{h} \int \sum_q [f_p(E) - f_q(E)] T_{pq}(E) dE, \tag{2.31}$$

where f_p is the Fermi distribution in lead p. For a two-terminal system, this simplifies to

$$I = \frac{2e}{h} \int [f_L(E) - f_R(E)] T_{L,R}(E) dE. \tag{2.32}$$

The Fermi function makes sure that there is no current when the applied bias is zero. Here, it is assumed that the left lead is grounded and there is an applied bias V_a on the right lead, such that $f_R(E) = f_L(E + eV_a)$. Further, for a two-terminal system, the bond current between site i and j may be calculated as [134]

$$I_{i\to j} = -\frac{4e}{\hbar} \int [f_L(E) - f_R(E)] \mathrm{Im}\left\{ H_{i,j} A^{(L)}_{j,i}(E) \right\} dE, \tag{2.33}$$

where H is the Hamiltonian and $A^{(L)} = G\Gamma_L G^\dagger$ is the left spectral function. A spin-degeneracy factor of two has been included. In the low temperature limit, the difference between Fermi functions becomes a top-hat function with a width of eV_a starting at E_F. If additionally the bias is low enough that the spectral function is approximately constant over the integration window, the bond current becomes

$$I_{i\to j} \simeq -\frac{4e^2 V_a}{\hbar} \mathrm{Im}\left\{ H_{i,j} A^{(L)}_{j,i}(E_F) \right\}. \tag{2.34}$$

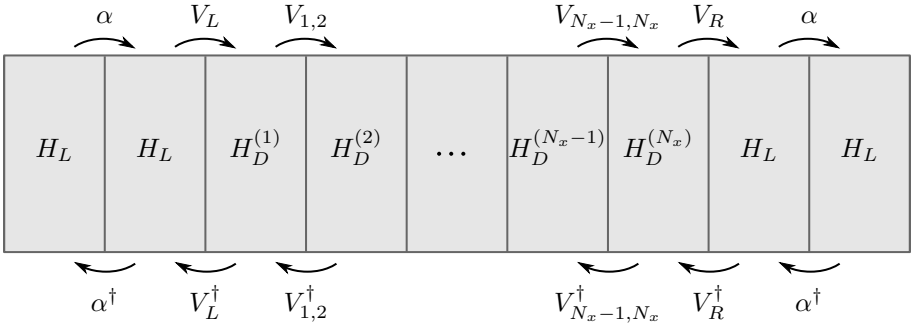

Fig. 2.5: Partitioning of the system into N_x slices as used in the RGF method. Each slice is characterized by a 1) local Hamiltonian ($H_D^{(i)}$ in the device region and H_L in the leads) that only describes couplings within the slice, and 2) coupling matrices V_{ij} that describe the coupling between slice i and j. The coupling to the leads is given by $V_{L/R}$ and the interlead coupling is given by α.

Calculating the Green's function has complexity $\mathcal{O}(N^3)$, where N is the number of atomic orbitals used in the model, which in the context of graphene is typically equal to the number of atoms. For most properties, the entire Green's function is actually not needed, just certain submatrices of it. This fact coupled with the sparsity of the TB Hamiltonian is used to extract different properties efficiently using the RGF method. Here, the unit cell is divided into N_x slices along the x-direction with N_y atoms in each slice. This is illustrated in Fig. 2.5 along with the sub-Hamiltonians and coupling matrices of the slices. By partitioning the system this way, the Hamiltonian becomes block tridiagonal, which is exactly the fact that is used to write up the RGF algorithms. The only requirement of the RGF method is that the atoms in each slice only couple to atoms in the same slice or its nearest neighbors. The complexity of calculating transmittance and DOS is reduced to $\mathcal{O}(N_x N_y^3)$ in the RGF method. This method is thus ideal for systems that are considerably longer (x-direction) than wide (y-direction). A rigorous description of the RGF method as used in graphene is given in Ref. [113].

2.5 Magnetotransport

In the presence of a magnetic field, the momentum operator is $\hat{\boldsymbol{p}} \to \hat{\boldsymbol{p}} + e\boldsymbol{A}$, where $\boldsymbol{A}$ is the vector potential of the magnetic field. The vector potential is related to the magnetic field by $\nabla \times \boldsymbol{A} = \boldsymbol{B}$. Many different choices can be made for $\boldsymbol{A}$, which gives rise to the same $\boldsymbol{B}$ and the specific choice of $\boldsymbol{A}$ is referred to as the gauge. The solution to the Schrödinger equation should of course be gauge invariant and the gauge is therefore chosen based on simplicity

of calculations. A common choice is the Landau gauge, which for a magnetic field pointing the z-direction, $\boldsymbol{B} = \hat{z}B$, reads $\boldsymbol{A} = \hat{y}Bx$. This gauge has the advantage that it is invariant in the y-direction, making it straightforward to treat systems that are periodic along this direction.

In TB, the magnetic field is introduced by the Peierls substitution [33, 99] $t_{ij} \to e^{i\phi_{ij}} t_{ij}$, where t_{ij} is the hopping parameter between atom i and j, $\phi_{ij} = (e/\hbar) \int_{\boldsymbol{R}_i}^{\boldsymbol{R}_j} \boldsymbol{A} \cdot d\boldsymbol{l}$ is the Peierls phase and $\boldsymbol{R}_i$ is the position of atom i. Since the hopping parameters are unchanged compared to the non-magnetic case, it is straightforward to include an applied magnetic field in a TB Hamiltonian. Once the Hamiltonian is correctly modified to account for the magnetic field, it is only a matter of using the NEGF formulas above to extract properties.

For magnetotransport calculations, the magnetic field is only applied in the device region, and the magnetic field in the leads is thus vanishing. In order to avoid discontinuities in the vector potential (which would give rise to an infinite magnetic field), the vector potential in the left (right) lead should be a constant equal to the vector potential on the left (right) side of the device. This means that the vector potential cannot be chosen to be zero in both leads simultaneously. However, since the magnetic field is simply the curl of the vector potential, a constant vector potential still gives rise to vanishing magnetic field. This concept is illustrated in Fig. 2.6 along with a unit cell of a GAB with a triangular antidot lattice.

In order to obtain a periodic Hamiltonian for 2D periodic systems, the Peierls phase between a pair of neighbors on either side of the unit cell is required to be an integer multiple of 2π. This limits the possible values of

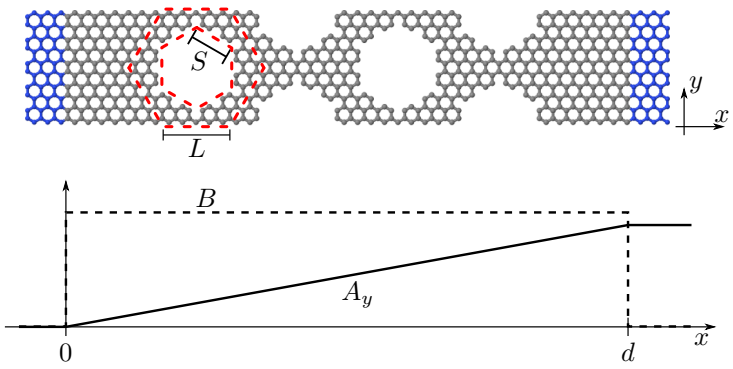

Fig. 2.6: Unit cell of a GAB with a triangular antidot lattice used in transport calculations and corresponding vector potential and magnetic field. The gray and blue atoms represent the system and semi-infinite leads, respectively. The dashed red lines outline the corresponding GAL unit cell.

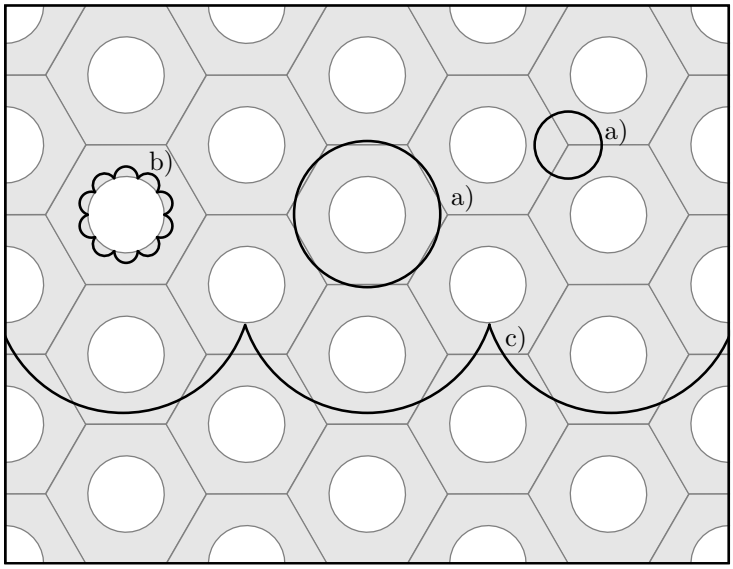

Fig. 2.7: Examples of non-chaotic cyclotron trajectories of classical charge carriers in an antidot lattice. a) pinned orbits, b) magnetic edge state, and c) skipping orbit.

applied magnetic fields to $B = nB_{min} \propto n/L$, where $B_{min} \propto 1/L$ is the smallest magnetic field that ensures periodicity and L is the length of the unit cell. For a single unit cell of a graphene antidot lattice, B_{min} would be quite large. By creating a supercell consisting of many replicas of the graphene antidot unit cell, the value of B_{min} can be reduced arbitrarily. Then, by appropriately choosing the length of the supercell, practically any magnetic field can be used in the calculations. The calculation time of course increases with increasing unit cell size and thus leads to the counter-intuitive result that it is computationally significantly harder to apply a small magnetic field than a large one. Note that this is only the case for 2D periodic systems and does not apply to transport in graphene antidot barriers, which are only 1D periodic.

It is well-known that the trajectory of charge carriers is curved in the presence of a magnetic field due to the Lorentz force. This will often lead to chaotic trajectories in antidot lattices, due to scattering in seemingly random directions. However, three different types of non-chaotic cyclotron trajectories of classical charge carriers can be identified in an antidot lattice, see Fig. 2.7. First, a pinned orbit can be identified, which is a non-scattering orbit either around or between antidots, which should give rise to very high resistance. Next, a magnetic edge state can be identified, where the charge carrier is confined to the periphery of the antidot due to repeated reflection on the antidot

edge. Intuitively, this should give rise to increased resistance, as these orbits are localized to the antidot edge. However, it will be shown that this is not always the case. Finally, a skipping orbit can be identified, for which each reflection on the antidot edge cause movement in the same direction, thus easing the transport through the system and thereby give rise to to low resistance. The focus in the thesis is on the magnetic edge states, as these give rise to periodic features in the transmittance spectrum and are thus easy to identity.

2.6 Spin transport

In TB, the molecular wave function is written as a linear combination of atomic orbitals. So far, a single non-spin-polarized orbital per atomic site has been used. In order to include spin effects, two spin-polarized orbitals per atomic site must be used instead. All the NEGF formulas above also work in the spin-polarized case, but introducing spin doubles the dimensions of the Hamiltonian and the Green's function and thus increases calculation time.

For a perfect graphene lead (with no impurities and thus no spin scattering), the two spin-channels are completely decoupled in the leads and each spin-channels can thus be viewed as a separate lead. Therefore, the transmittance between spin-channel σ in lead i to spin-channel σ' in lead j can trivially be written as

$$T_{i\sigma,j\sigma'} = \mathrm{Tr}\{\Gamma_{i\sigma} G^\dagger \Gamma_{j\sigma'} G\}. \tag{2.35}$$

Spin scattering inside the system is taken into account by the Green's function. For a two terminal system with left (L) and right (R) spin-polarized leads, this gives rise to a 4×4 transmittance tensor

$$\boldsymbol{T} = \begin{bmatrix} T_{L\uparrow,L\uparrow} & T_{L\uparrow,L\downarrow} & T_{L\uparrow,R\uparrow} & T_{L\uparrow,R\downarrow} \\ T_{L\downarrow,L\uparrow} & T_{L\downarrow,L\downarrow} & T_{L\downarrow,R\uparrow} & T_{L\downarrow,R\downarrow} \\ T_{R\uparrow,L\uparrow} & T_{R\uparrow,L\downarrow} & T_{R\uparrow,R\uparrow} & T_{R\uparrow,R\downarrow} \\ T_{R\downarrow,L\uparrow} & T_{R\downarrow,L\downarrow} & T_{R\downarrow,R\uparrow} & T_{R\downarrow,R\downarrow} \end{bmatrix}. \tag{2.36}$$

The spin-coherent transmittance is defined as $T_{sc} \equiv T_{\uparrow\uparrow} + T_{\downarrow\downarrow}$ and the spin-flipped transmittance is defined as $T_{sf} \equiv T_{\uparrow\downarrow} + T_{\downarrow\uparrow}$, where the shorthand notation $T_{\sigma\sigma'} \equiv T_{L\sigma,R\sigma'}$ has been used.

The spin-dependent transport of hydrogenated graphene is calculated in paper IV. It is found that graphene systems with hydrogen adatoms can be accurately described with a remarkably simple model. In particular, the hydrogen adatom (H) is coupled to the graphene backbone by allowing only a spin-independent hopping t' to the carbon site beneath it (C_0). Only the hydrogen on-site potential is taken as spin-dependent with of $\varepsilon_\uparrow$ and $\varepsilon_\downarrow$ for the

majority and minority spin channels, respectively. In case of a single hydrogen adatom, this means the Hamiltonian can be written as

$$\hat{H} = \hat{H}_0 + t'(|C_0\rangle\langle H| + |H\rangle\langle C_0|) + |H\rangle\langle H| \otimes (\varepsilon_\uparrow|\uparrow_{\boldsymbol{a}}\rangle\langle\uparrow_{\boldsymbol{a}}| + \varepsilon_\downarrow|\downarrow_{\boldsymbol{a}}\rangle\langle\downarrow_{\boldsymbol{a}}|), \quad (2.37)$$

where $\hat{H}_0$ is the graphene backbone part, $|H\rangle$ and $|C_0\rangle$ are the orbitals on the H and C_0 atoms, respectively, and $|\uparrow_{\boldsymbol{a}}\rangle$ and $|\downarrow_{\boldsymbol{a}}\rangle$ are the orthogonal spin basis vectors along the spin-quantization axis $\boldsymbol{a} = [\sin\theta\cos\phi, \sin\theta\sin\phi, \cos\theta]$. In this model, the quantization axes of the defect spin moments are considered as classical vectors that can be rotated individually. In the dilute limit, the interactions between the defects can be assumed small. Then a finite temperature or other environmental factors can break the magnetic ordering in a system with many hydrogen adatoms. In such a case, the same spin basis cannot be chosen simultaneously for all the defect spin moments. Additionally, in the limit of many nearby defects, frustration can result in a nontrivial spin moment configuration that can be difficult to estimate without explicitly including the defect spin-spin interactions.

In order to obtain spin directions that are distributed uniformly random on the Bloch sphere, it is insufficient to choose angles $\theta \in [0, \pi]$ and $\phi \in [0, 2\pi]$ uniformly random, as this would lead to an increased probability at the poles and thus lead to a non-uniform sampling. In order to obtain a uniform sampling, two numbers u and v are picked uniformly random in the interval $[0, 1]$. The angles are then calculated as $\theta = \cos^{-1}(2u - 1)$ and $\phi = 2\pi v$. The difference between these two methods is illustrated in Fig. 2.8.

In the model, the magnetic impurities (in this case H adatoms) are dispersed randomly across the device, as shown in Fig. 2.9. Electrons have a probability to flip their spin to the opposite spin channel at the impurity sites. If the probability of spin flipping does not depend on previous scattering events, the spin polarization will decay exponentially. This type of spin relaxation mechanism

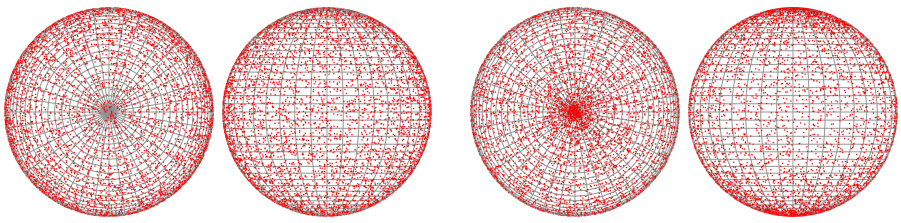

(a) Uniform sampling **(b)** Non-uniform sampling

Fig. 2.8: Random points chosen on Bloch sphere. Top- and side-view of (a) uniform and (b) non-uniform sampling.

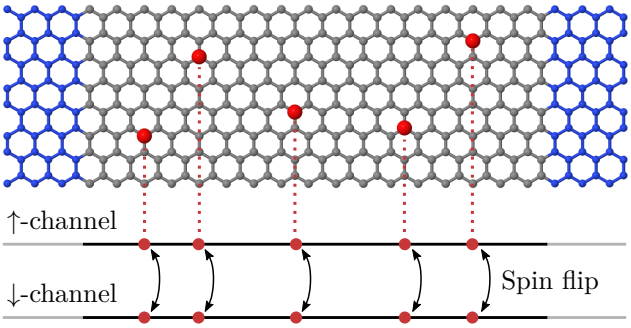

Fig. 2.9: Unit cell of a graphene device with a number of magnetic impurities scattered randomly across the device. The gray and blue atoms represent the system and the semi-infinite leads, respectively, while the red atoms represent the magnetic impurities. The spin of an electron only flips due to scattering at the magnetic impurities.

is known as Markovian spin relaxation. It is actually quite simple to set up a classical statistical model of the spin relaxation due to uncorrelated scattering events. The spin-resolved electron density is denoted as $\boldsymbol{n} = (n_\uparrow, n_\downarrow)^T$ and assume that the electron density is completely spin polarized in the ↑-channel, $\boldsymbol{n}_0 = (n_\uparrow^{(0)}, 0)^T$, before any scattering events. Upon encountering impurity m with probability κ to flip the spin, the electron density is equal to the number of electrons in the channel minus those that flipped plus those that flipped back from the other channel

$$\boldsymbol{n}_m = \boldsymbol{n}_{m-1} - \kappa \boldsymbol{n}_{m-1} + \kappa \begin{pmatrix} n_\downarrow^{(m-1)} \\ n_\uparrow^{(m-1)} \end{pmatrix} = \begin{pmatrix} 1-\kappa & \kappa \\ \kappa & 1-\kappa \end{pmatrix} \boldsymbol{n}_{m-1}. \tag{2.38}$$

By multiple application of this equation, it is easy to relate $\boldsymbol{n}_m$ to $\boldsymbol{n}_0$

$$\boldsymbol{n}_m = \begin{pmatrix} 1-\kappa & \kappa \\ \kappa & 1-\kappa \end{pmatrix}^m \boldsymbol{n}_0 = \begin{pmatrix} n_\uparrow^{(0)}/2\,(1+(1-2\kappa)^m) \\ n_\uparrow^{(0)}/2\,(1-(1-2\kappa)^m) \end{pmatrix}. \tag{2.39}$$

This is known as a Markov chain and is exactly where this type of spin relaxation mechanism derives its name.

The spin polarization is defined as

$$P = \frac{n_\uparrow - n_\downarrow}{n_\uparrow + n_\downarrow}. \tag{2.40}$$

With this definition, the spin polarization is 1 when the system is fully ↑-polarized and -1 when the system is fully ↓-polarized. The spin polarization

after m uncorrelated scattering events is thus

$$P_m = \frac{n_\uparrow^{(m)} - n_\downarrow^{(m)}}{n_\uparrow^{(0)}} = (1-2\kappa)^m = e^{m\ln(1-2\kappa)}, \tag{2.41}$$

where $\ln(1-2\kappa) < 0$ for all $\kappa \in [0; 0.5[$, which gives rise to a decaying exponential function. It is expected that $\kappa \ll 0.5$. If the scatterers are dispersed randomly across the device, m can be thought of as representing length L and the ln factor as representing spin relaxation length λ_s and as such give rise to a spin polarization on the form

$$P(L) = e^{-L/\lambda_s}. \tag{2.42}$$

It can thus be seen that the spin polarization decays exponentially with length. Markovian spin relaxation is therefore interpreted as classical behavior and deviations to this is interpreted as due to quantum effects. In the presence of quantum effects the spin relaxation can be much more complicated. For instance, a quantum mechanical model by Zurek *et al.* [135] show that spin relaxation can either be exponential or Gaussian, depending on the distribution of spin couplings to an environment. In order to include both cases as well as any intermediate relaxation mechanism, the spin polarizations obtained in the simulations are fitted to the following expression

$$P(L) = \frac{T_{sc} - T_{sf}}{T_{sc} + T_{sf}} = e^{(-L/\lambda_s)^n}, \tag{2.43}$$

where T_{sc} is the spin-conserved transmittance and T_{sf} is the spin-flipped transmittance. It then follows that the spin relaxation is exponential (Markovian) when the exponent is $n = 1$ and Gaussian when the exponent is $n = 2$.

Chapter 3

Summary of results

This chapter will present a collection of results from all five papers. First, results of the Dirac equation (DE) based models from papers I and II are presented. For these models, the new analytical results discussed in the previous chapter is additionally shown. Next, the spin- and magnetotransport results from papers IV and V are presented. Finally, the results of the study of the stability of Fe membranes in graphene perforations from paper III are presented.

3.1 Dirac equation-based models

In papers I and II the DE models are compared to tight-binding (TB) calculations. The computational complexity of the DE methods is scale invariant and as such allows for calculations on arbitrarily large structures. By contrast, the computational complexity of calculating eigenvalues of an N-atom system in TB is $\mathcal{O}(N^3)$. Thus, doubling the simulated area in TB increases the computational time by a factor of $(2^2)^3 = 64$. The presented DE models use a spatially varying mass term $\Delta(\boldsymbol{r})$ to model the antidots, with a value of Δ inside the antidots and vanishing elsewhere. Unless stated otherwise, a value of $\Delta = 170$ eV$/L$ is used in the calculations. The papers focuses, in particular, on the validity of the DE-based models compared to TB.

3.1.1 Electronic structure

A previous model of graphene antidot lattices using the DE with a spatially varying mass term was put forward by Fürst *et al.* [35]. In their model the mass term is explicitly taken to infinity, leading to a boundary condition on the wave function. This boundary condition becomes undefined in the limit

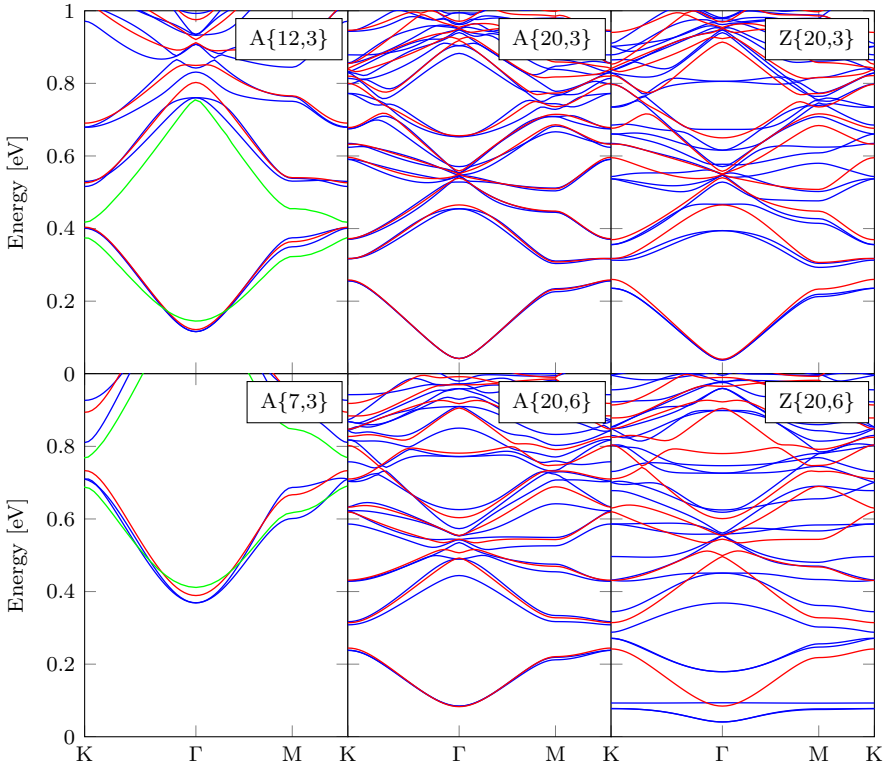

Fig. 3.1: Comparison of DE (red) and TB (blue) band structures for different GALs. The side lengths of the antidots in the DE has been chosen such that the antidot area is the same as in TB. The band structures of two of the systems is additionally compared to the scissor shifted DE (green) results by Fürst *et al.* [35].

of $R \to 0$, which causes the band gap to remain in this limit. They find that this error can be remedied somewhat by applying a scissor shift of the band structure of $1.02\gamma/L$.

In Fig. 3.1, the band structures calculated with the DE and TB is compared for 6 different systems. Here, the notation $\{L, S\}$ is used to refer to GALs with unit cell side length L and antidot side length S. Further, the antidot edge is either purely armchair (A) or purely zigzag (Z). Only positive energies are shown due to perfect electron-hole symmetry in the models. In the DE method there is of course no edge chirality, so it seems strange to distinguish between zigzag and armchair antidots. However, for hexagonal antidots, the chirality also gives rise to a rotation of 30° of the antidots in the unit cell, whereby antidots in a GAL lattice are either edge-to-edge for zigzag antidots or vertex-

to-vertex for armchair antidots. The orientation of the antidots is opposite for antidots in the RGAL lattice. For two of the systems, the band structures are additionally compared to the first two bands of the scissor shifted DE results by Fürst *et al.* There is a good agreement between the DE model and TB for armchair antidots GALs, especially for the lowest lying band. It makes sense that the accuracy increases with decreasing energy, as the Dirac approximation on which the model is based, is a low-energy approximation of the full TB result. The agreement is best when the area of the antidot is small compared to the total area of the unit cell. Additionally, the agreement is much better for the presented DE model than the DE model by Fürst and coworkers. For the systems with zigzag antidots, there is rather poor agreement between the DE model and TB. The discrepancy between the models turns out to be due to localized edge states, which occur for extended zigzag edges and which are absent in the Dirac model. The localized edge state is clearly visible in the band structure of the Z{10,6} as the near-dispersionless bands, which is the third conduction band in this case. A comparison of the electron probability density of the third conduction band between the zigzag and armchair antidot systems is shown in Fig. 3.2. For the zigzag antidot system, the probability density is completely confined to the periphery of the antidot. For the armchair antidot system, however, the probability density is distributed over the entire unit cell. This edge behavior is found to be common for zigzag antidots. Localized edge states in graphene due to extended zigzag edges have also been observed by other authors [136–138]. Since the DE is a continuum model, all atomistic features, such as chirality, are missing.

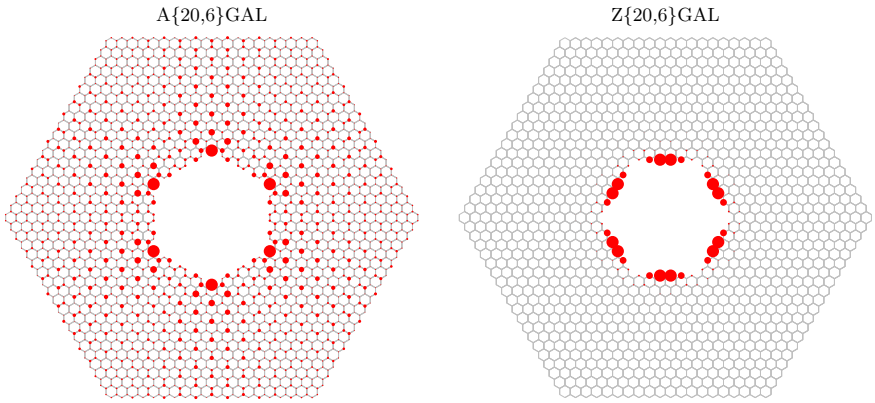

Fig. 3.2: Electron probability density of the third conduction band in one unit cell calculated used TB and averaged over the Brillouin zone. The radius of each circle is proportional to the absolute square of the eigenvector element for that atom.

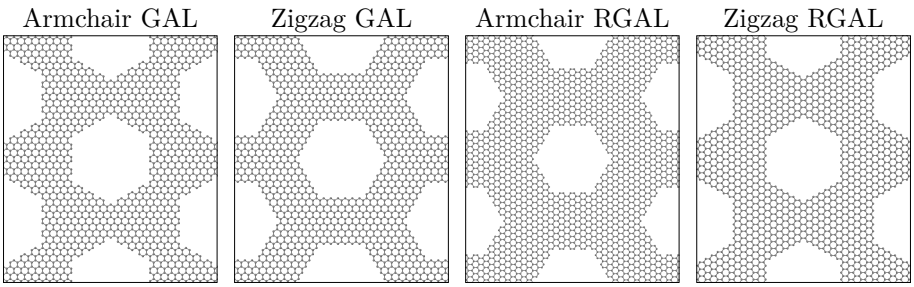

Fig. 3.3: Comparison between armchair and zigzag antidots in GAL and RGAL configurations. Notice that the underlying graphene lattice is rotated 30° between the GAL and RGAL lattices.

In order to highlight the accuracy of the DE model, the band gap obtained in DE is compared to TB in Fig. 3.4 for a large number of different structure realizations. The results are additionally compared to the approximate analytical expression for the band gap given by Eq. (2.11). The band gaps are shown for both GAL and rotated GAL (RGAL) lattices, where the underlying graphene lattice is rotated 30° degrees between the two lattice types, see Fig. 3.3. For armchair antidots in both GAL and RGAL configuration, there is very good agreement between DE and TB. However, some discrepancies emerge for large antidots in RGAL configuration. Armchair antidots in RGAL configuration resemble a connected network of graphene nanoribbons, since the antidots are oriented edge-to-edge. As the size of the antidot increases, the "nanoribbon width" decreases. It was noted by Brey and Fertig [137] that the DE band gap of narrow armchair graphene nanoribbons deviate more from TB than wide nanoribbons, which is consistent with the observations for armchair antidots in RGAL configuration. The band gap of zigzag and circular antidots are consistent with TB only when the area fraction of antidots in the unit cell is small, with large discrepancies emerging for larger antidots. These discrepancies occur primarily due to the presence of extended zigzag edges on the antidots, which lead to edge states that are not described in the DE model. It is interesting that the numerical DE results are almost invariant to the shape of the antidots even though there is a rather large geometrical difference between circular antidots, hexagonal antidots oriented edge-to-edge and hexagonal antidots oriented vertex-to-vertex. The largest possible area fraction for edge-to-edge hexagonal antidots is 1, while it is only 3/4 for vertex-to-vertex antidots and $\pi/2\sqrt{3} \approx 0.9$ for circular antidots. However, results indicate that in the DE model, the overwhelmingly most important parameter for the band gap is the area fraction of the antidot, not its shape.

From the band gap analysis, it can be concluded that the presented DE

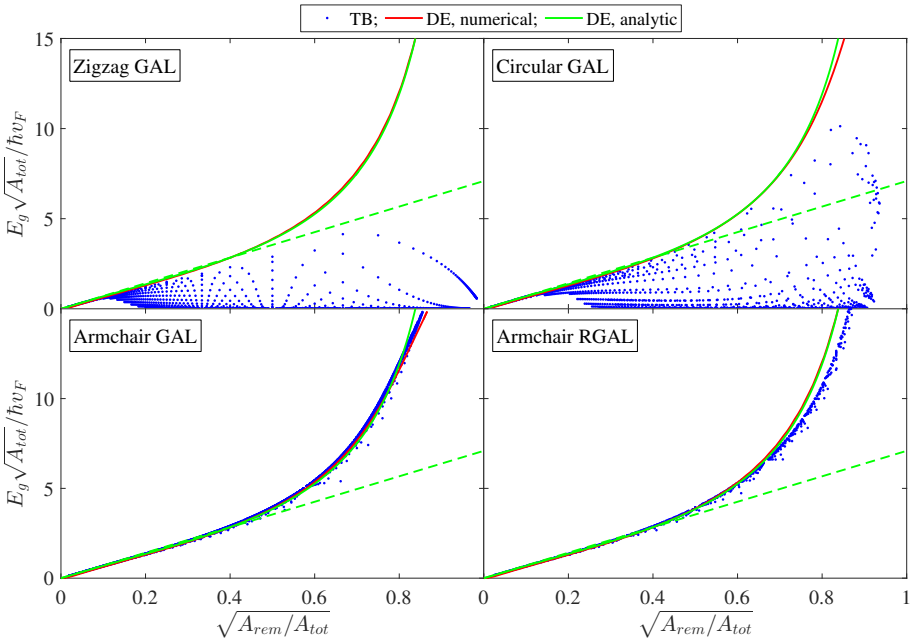

Fig. 3.4: Band gap of several different GALs and RGALs for armchair, zigzag and circular antidots. The points show the TB results and the lines represent the DE results. The solid green line is based on Eq. (2.11) and the dashed green line is based on Eq. (2.12)

model is in very good agreement with TB in the absence of localized edge states. It is reasonable to expect that localized edge states contribute very little to electronic transport, especially in the presence of disorder. Therefore, for electronic transport calculations, it may not be a major drawback that these are absent in the DE model.

3.1.2 Electronic transport

A method for calculating the scattering of charge carriers by graphene antidots was developed in paper II based on the DE using a Green's function method. This method is also suitable for calculating scattering of periodic structures, such as graphene antidot barriers (GABs) as shown in Fig. 2.2. The transmittance can be extracted by calculating the charge current in a GAB. The calculation time can be reduced significantly by employing an efficient iterative method, which is outlined in Sec. 2.3. In Fig. 3.5, the transmittance of different GABs calculated with the presented DE method is compared to the transmittance calculated using a tight-binding method. As with the electronic structure calculations, it is found that the DE method is in agreement with TB in ab-

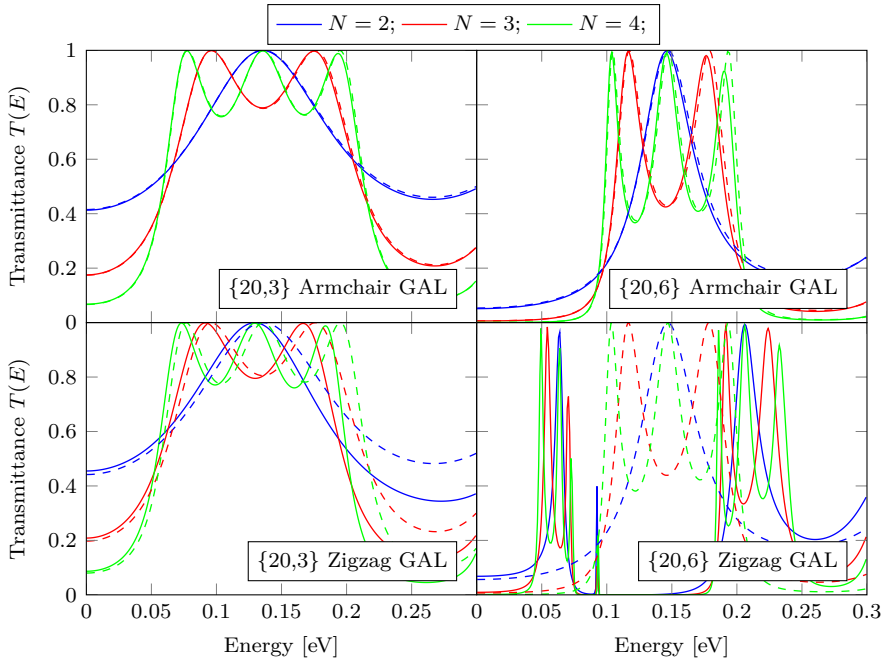

Fig. 3.5: Transmittance of GABs with N rows of antidots in the transport direction calculated with TB (solid) and the DE (dashed). The antidots are hexagonal with either armchair or zigzag edge chirality.

sence of localized edge states. Specifically, there is here excellent agreement between the DE method and TB for the two armchair antidot structures, as well as reasonable agreement for the system with the small zigzag antidots. For the structure with the larger zigzag antidots there is poor agreement, again due to localized edge states. An important thing to note is that, since the localized edge states are localized in both space and energy, small amounts of disorder is likely to suppress the electronic transport of these states. In fact, Power and Jauho [38] subsequently studied the electronic transport of finite graphene antidot structures and found the transmittance of these localized edge states to be greatly reduced in the presence of disorder.

A useful measure of a system is its transport gap, which is defined here as the energy region near the Fermi level, where the transmittance is strictly less than 1/2. It may be thought of as the transport equivalent of a band gap. In fact, for an infinitely wide and perfectly ordered barrier, the transport gap is equal to the band gap. Further, the definition of a transport gap makes it possible to compare the DE method to TB for a large number of structure realizations

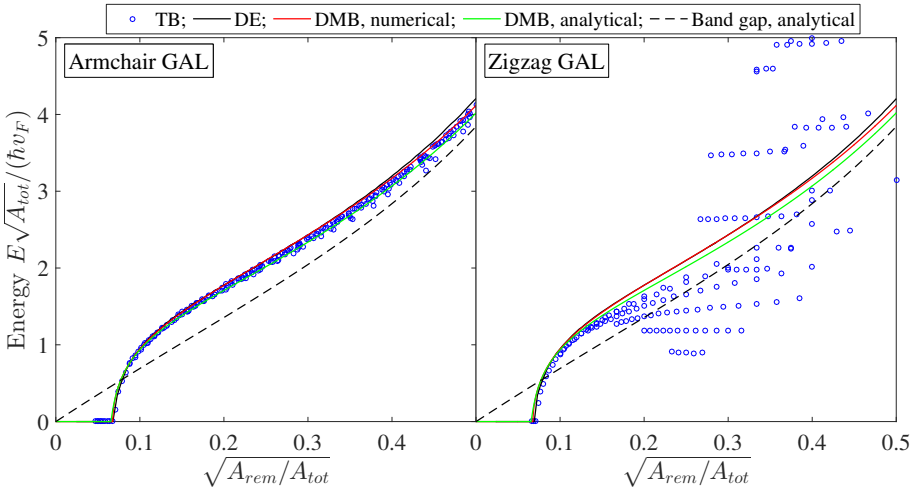

Fig. 3.6: Transport gap of GABs with 4 armchair or zigzag antidots. The mass term used in the DE is here twice the value used elsewhere, which slightly improves the agreement with TB near the onset of the transport gap. The Dirac mass barrier (DMB) results are based on numerical solutions to Eq. (2.24) and the analytical result given by Eq. (2.26).

as was also done for the band gap, see Fig. 3.6. The results are also compared to the transport gap of a Dirac mass barrier (DMB). The band gap used in the DMB calculations is taken as the band gap given by Eq. (2.11). The analytical expression of the band gap is based on the assumption of circular antidots, and is therefore invariant over edge chirality. As a consequence, the DMB, which relies on this expression, is also invariant over the edge chirality. As discussed before, the antidot chirality in the DE model only enters through a 30° rotation of the antidot in the unit cell and is therefore only purely geometrical. As with the band gap, the figure shows that this rotation makes very little difference on the results. The figure shows that the transport gap of the armchair antidots systems is in good agreement between all models. Note that the DMB is only in agreement with TB near the onset of the transport gap, while the DE model is in agreement with TB even at significantly higher energies. Of course, in the context of transport gap, this difference is not so important. As before, there is poor agreement between TB and the DE models for the zigzag antidots when the antidots takes up a significant fraction of the unit cell. However, the discrepancy of the zigzag results in the case of the transport gap is actually much lower than was the case of the band gap. This fact may increase the usability of the DE model to predict transport properties of experimental graphene antidot systems, especially if edge state effects diminish

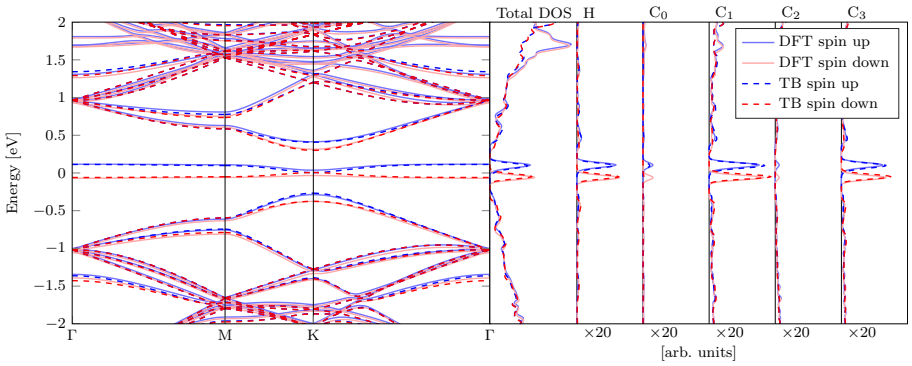

Fig. 3.7: Spin-polarized band structure, total DOS and LDOS of an 8×8 graphene supercell with a single hydrogen adatom. The DFT atom-projected DOS is compared to the TB LDOS at the hydrogen adatom (H), the carbon atom directly underneath (C_0) and its first-, second-, and third-nearest neighbors C_1, C_2 and C_3, respectively.

in the presence of disorder.

3.2 Spin transport

The spin relaxation mechanism in hydrogenated graphene was studied in paper IV. It turns out that hydrogen adatoms can be modeled with a remarkably simple Hamiltonian, where the only spin dependent parameter is the H on-site energy. The fitted band TB band structure, total density of states (DOS) and local DOS (LDOS) are shown in Fig. 3.7. The figure shows excellent agreement between the TB model and the DFT results.

In Fig. 3.8, the spin polarization as a function of device length is shown for different impurity concentrations. The spin polarization decays rapidly near the H adatom impurity bands, which are located near the charge neutrality point (CNP), for all impurity concentrations. As expected, the spin polarization decays faster with increasing impurity concentration. Note that the spin polarization also decay for energies away from the H defect bands, due to the small, but finite, spin splitting in the remaining band structure. The small energy-dependent oscillations in the figure arise due to finite seize effects originating from the finite width of the unit cell.

The spin polarization is expected to decay as $P(L) \simeq e^{-(L/\lambda_S)^n}$, where L is the device length, λ_S is the spin relaxation length and n is an exponent that depends on the spin relaxation mechanism. For Markovian spin relaxation, the spin polarization decays exponentially and the exponent is $n = 1$. λ_S and n can be extracted by fitting the spin polarization against this expression. The

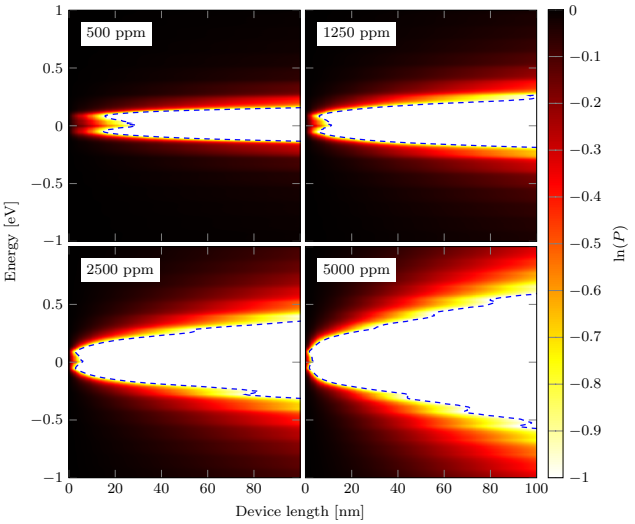

Fig. 3.8: Ensemble-averaged spin polarization as a function of energy and device length for different impurity concentrations. The dashed lines show the spin relaxation length.

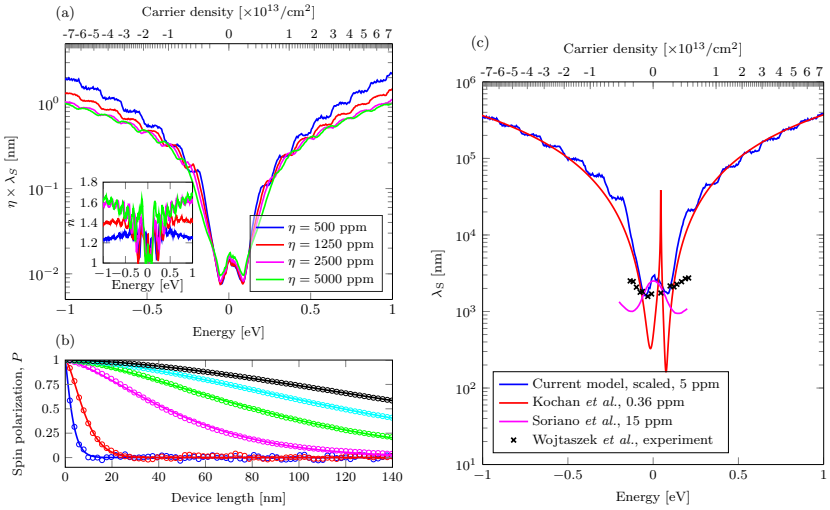

Fig. 3.9: (a) Normalized spin relaxation length $\eta \times \lambda_S$ and exponent n (inset) obtained by least squares fitting. The spin relaxation lengths are normalized with the defect concentration in order to illustrate that their inverse scale nearly linearly with respect to it. (b) Examples of spin relaxation fitting, where the circles are the ensemble averaged spin polarizations and the lines are the corresponding fitted functions. The energies are between 0.0 eV (fastest decay) and 1.0 eV (slowest decay) in steps of 0.2 eV. (c) Comparison of spin relaxation lengths obtained by different authors [82, 88, 90].

extracted spin relaxation length and exponent is shown in Fig. 3.9. Positive and negative carrier densities on the axis refer to electron and hole doping, respectively. The spin relaxation length is very short for energies near the H defect bands (close to the CNP). At these energies, the spin relaxation mechanism is predominantly exponential with an exponent of $n \simeq 1$. For higher energies, the exponent is increased, but it is seen that it converges towards $n \approx 1$, as the impurity concentration is decreased. This demonstrates that the spin relaxation mechanism is Markovian near the CNP, as well as in the highly dilute limit. That the spin relaxation mechanism approaches Markovian in the highly dilute limit is expected, as it intuitively becomes more unlikely that scattering events are correlated, when the impurities are separated by large distances. The figure also shows that there is a nearly linear dependence between the impurity concentration and spin relaxation length λ_S. Near the CNP, the spin relaxation length is 1–2 orders of magnitude lower than for other energies. Due to the nearly linear scaling of the results with the impurity concentration, the 500 ppm result can be scaled to fit with experimental results by Wojtaszek *et al.* [82]. The results are additionally compared to other recent theoretical calculations on hydrogenated graphene by Soriano *et al.* [90] and Kochan *et al.* [88]. None of the theoretical models are able to fully explain the experimental result, but the presented model is reasonably close.

3.3 Magnetotransport

In this section, the electronic transport in GALs under the presence of an applied magnetic field will be described. The magnetic field is only applied in the device region and is vanishing in the leads. Most of the calculations are based on a TB description of graphene antidots. The results are compared to a TB gapped graphene model, where the on-site energy is shifted by Δ on one sublattice and $-\Delta$ on the other, as well as a Dirac mass barrier (DMB). The transmittance of a DMB under an applied magnetic field is derived in paper V and is based on wave function boundary matching. The advantage of both the DMB and gapped graphene models compared to TB is that they are much faster: for a barrier of length d (transport direction) and width w, the computational complexity is $\mathcal{O}(dw^3)$ for full antidot model, $\mathcal{O}(d)$ for the gapped graphene model and $\mathcal{O}(1)$ for the DMB. One of the major problems with the simplified models is that they depend on knowing the effective band gap of the barrier, which may not be known in advance. In the DMB calculations, a look-up table of the band gap of infinite GALs based on the TB results from paper I has been used. Another approach would be to use an approximate

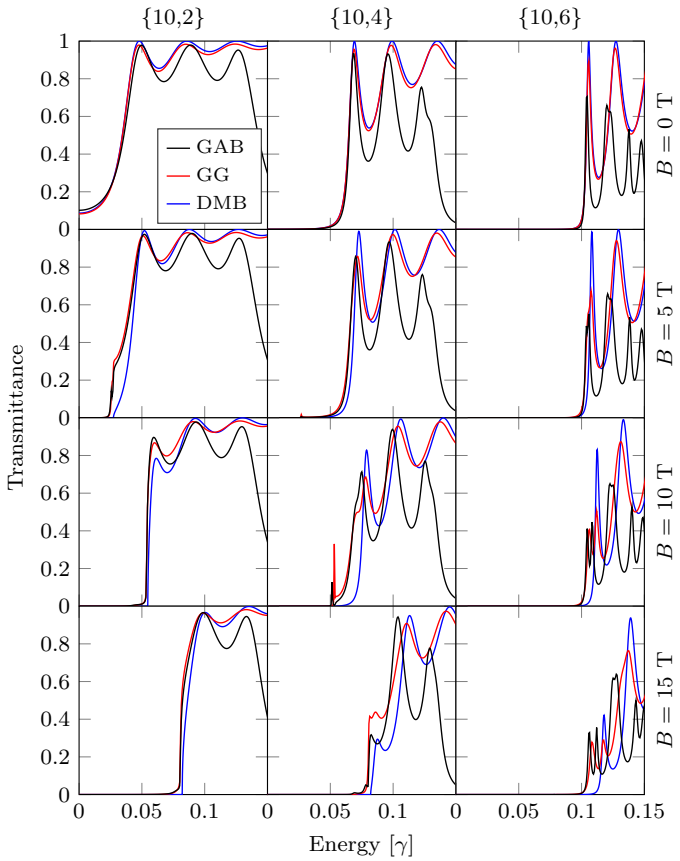

Fig. 3.10: Transmission through {10,S} triangular GABs containing 4 rows of armchair antidots in the transport direction, as well as gapped graphene (GG) and Dirac mass barriers (DMBs) with the same length and band gaps as the GABs.

band gap obtained by the analytical formula given by Eq. (2.11).

The transmittance obtained with these three models is compared in Fig. 3.10 for three different GAL barriers and four different values of the applied magnetic field. At these magnetic fields and especially near the onset of transmittance, the agreement between the models is quite good for the structure with the small antidots. The agreement seems to decrease a little with increasing size of the antidot and for increasing magnetic field. There is more deviation between the models, when the magnetic field is increased further (not shown). However, these results suggest that both the DMB and gapped graphene models are sufficient if one is primarily interested in the behavior near the onset of transport, for instance to determine the transport gap, of smaller

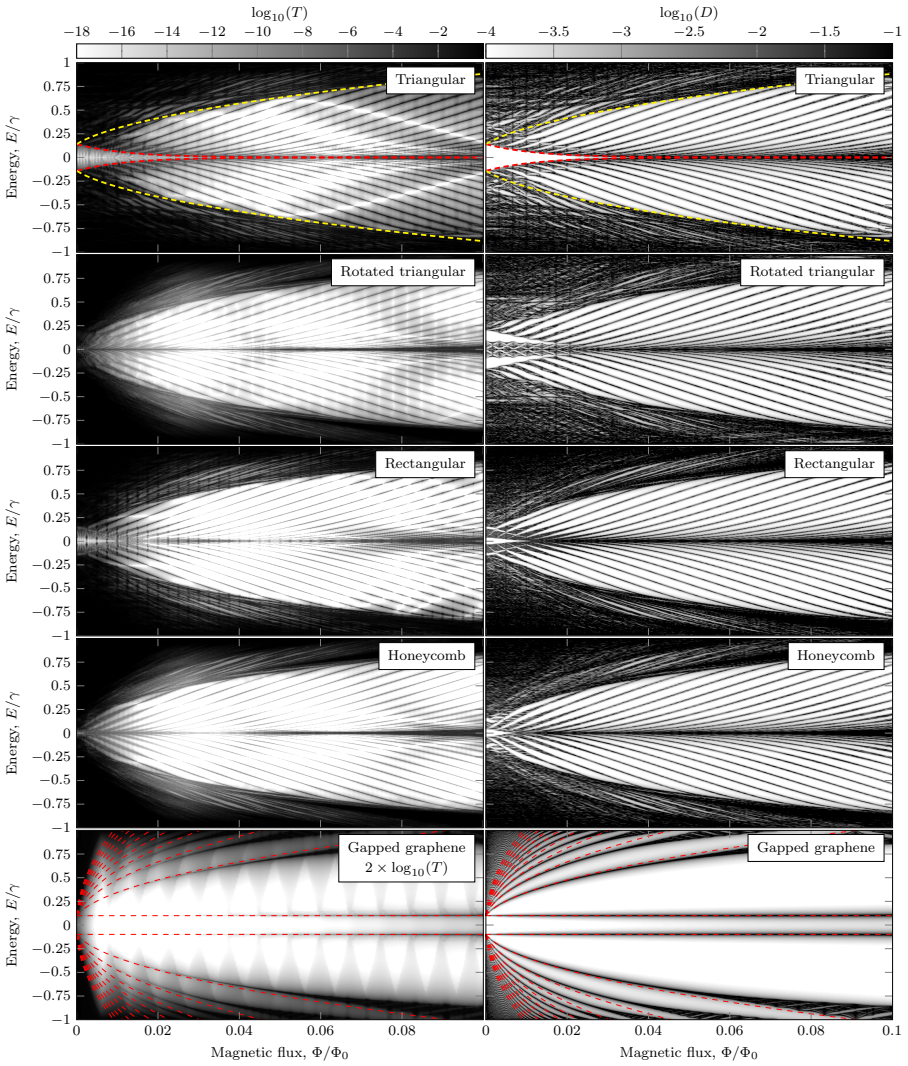

Fig. 3.11: Comparison between transmittance (left) and DOS (right) of {L,6} GABs with armchair antidots in different lattice configurations. The value of L was chosen to give all lattices a neck width of approximately 1.3 nm. For the triangular lattice, this corresponds to a {10,6} system. The transport calculations are made with 4 rows of antidots in the transport direction. The dashed lines in the top panels outline the geometric band gap (red) and the Landau level gap (yellow). The bottom panels show a $\Delta = 0.1\gamma$ gapped graphene system. The dashed red lines in the bottom panels show the first 10 Landau levels of massive Dirac fermions. For the gapped graphene model, $2 \times \log_{10}(T)$ is plotted due to the generally lower transmittance for this system.

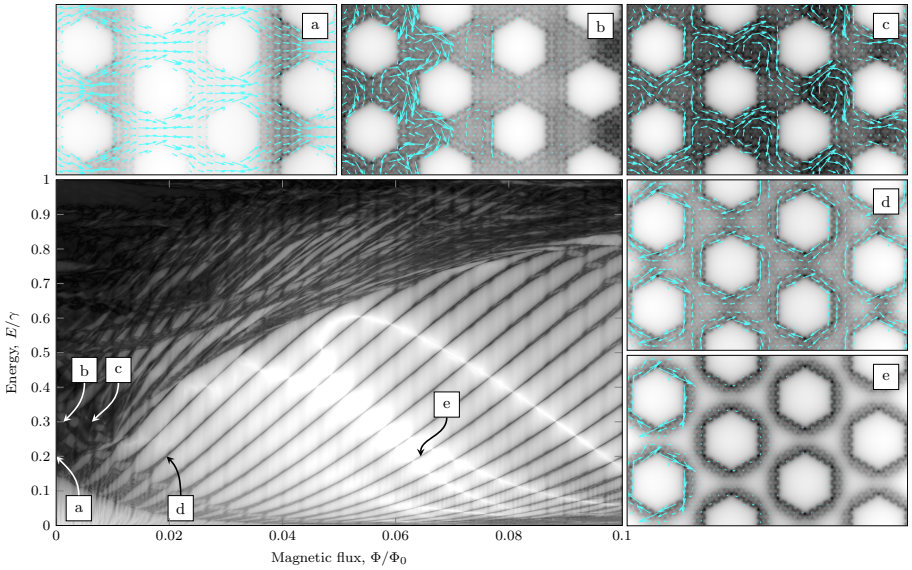

Fig. 3.12: LDOS (gray shading) and bond current (blue arrows) of a {10,6} triangular GAB for different B-field strengths at energies of $E = 0.2\gamma$ (a, d and e) or $E = 0.3\gamma$ (b and c). The main panel shows the transmittance of the system. Here, $\sqrt{|\log_{10} T|}$ is plotted in order to enhance the contrast.

antidots under not too strong applied magnetic fields.

It has been known for a long time that the DOS of a system under a magnetic field gives rise to a self-similar structure known as a Hofstadter butterfly [99]. Calculations of Hofstadter butterflies by Pedersen and Pedersen [33] have shown evidence of magnetically induced band gap quenching in GALs under applied magnetic fields. It is interesting to examine if this quenching also applies to the transport gap of GABs in magnetic fields. In Fig. 3.11, the transmittance and DOS spectra are compared for GABs in four different lattice configurations and for gapped graphene. It is seen that there is a very high degree of similarity between transmittance and DOS spectra. However, there are some deviations, especially near the zero-field band gap. Also, the DOS spectra does not offer much clue of the actual value of transmittance. Moreover, the magnetically induced band gap quenching does seem to apply to the transport gap as well. It is worth to note that the transmittance of these energies is significantly lower than the transmittance above the *Landau level gap* (note that the results are plotted on a log scale). Additionally, quenching does not occur in the gapped graphene model. This is because the band gap in gapped graphene was opened by sublattice imbalance rather than by geometrical effects.

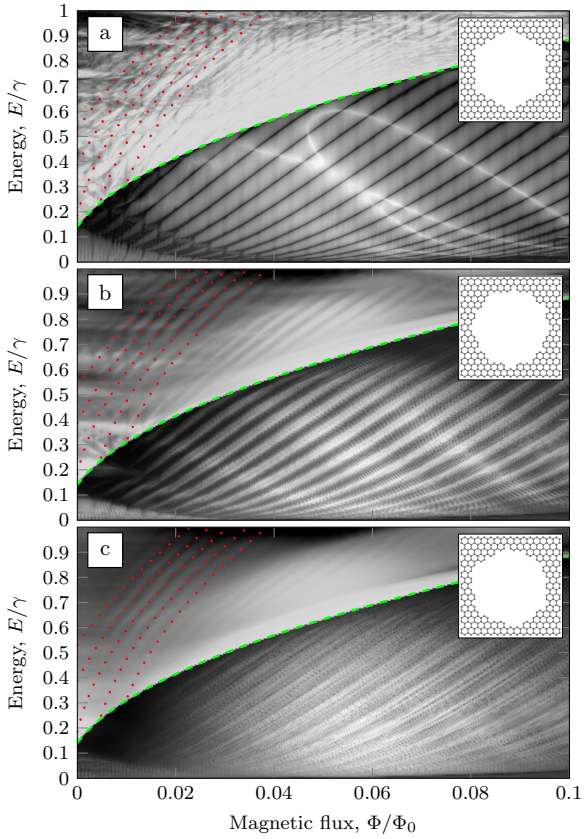

Fig. 3.13: Ensemble averaged transmittance of a) an ordered {10,6} triangular GAB and of disordered systems with b) small and c) large degree of disorder. An example of the disordered antidots in the two cases is shown as an inset. The dotted red lines are plotted according to $E_i/\gamma = \sqrt{a_i + b\Psi/\Psi_0}$, where a_i and b were determined by least squares fitting.

An intriguing property of these spectra are the narrow transmittance bands between the Landau level gap and the geometric band gap. These are examined further in Fig. 3.12, where the local DOS (LDOS) and the bond current at selected (E, B) values is plotted. The bond currents and LDOS are confined near the periphery of the antidots at the narrow bands, while they are not elsewhere. These narrow bands are therefore identified as magnetic edge states, which are defined here as states that are confined to the antidot edge by the presence of a magnetic field, not to be confused with spin-polarized edge states, such as those observed on extended zigzag edges [32].

There is a very rich substructure in both transmittance and DOS spectra. The question remains if any of this substructure is retained under the effects

of disorder. This is investigated in Fig. 3.13, which shows the transmittance of an ordered system, a moderately disordered system and a heavily disordered system. The disorder is created by removing atoms according to a Gaussian probability profile, which is why these antidots are more round than hexagonal. The figure shows that the magnetic edge states survive a moderate degree of disorder, but are destroyed by a large degree of disorder. Moreover, the figure shows that some of the substructure above the Landau level gap does survive both degrees of disorder and is highlighted by the red dotted lines on the figures.

3.4 Graphene-embedded monolayer Fe

In 2014, Zhao *et al.* [79] demonstrated experimentally that monolayer Fe membranes can be embedded in perforations in graphene. They found that the embedded Fe membranes form a square lattice with a bond length of about 2.65 Å. This finding was a bit surprising because 1) Fe has 6 valence electrons, which would tend favor a more tightly packed lattice, and 2) The bond length is much higher than in their own DTF calculations on free-standing monolayer Fe, which suggest a bond length of 2.35 Å. Inspired by these finding, a DFT analysis of the structural stability and magnetization of Fe systems is presented in an attempt to explain the experimental results, as well as to obtain a basic understanding of these systems.

The free-standing monolayer Fe system must be understood before it makes sense to try to understand the graphene-embedded Fe systems. The total energy and magnetization of free-standing monolayer Fe in ferromagnetic and antiferromagnetic ordering is shown in Fig. 3.14 for three different lattice configurations. The figure shows that ferromagnetic ordering is generally favored against antiferromagnetic ordering and that the triangular lattice is energetically favored at equilibrium, but with a crossover to square for compressive strain. At equilibrium, the bond lengths are 2.33 Å for the square lattice and 2.44 Å for the triangular lattice, both of which are significantly smaller than the experimental observation of 2.65 Å in graphene-embedded Fe membranes. Moreover, at tensile stress, the triangular lattice is even more energetically favored than at equilibrium. So what is happening in the experiments? Fe on the graphene surface is mobilized by e-beam irradiation. The Fe move until it is trapped in a perforation, thus forming the Fe membrane essentially one atom at a time. This means that during formation of membrane, the edge formation energy is very important. The edge formation energy is the energy cost of having an edge compared to being in bulk and can essentially be thought of as the energy cost of fracturing the membrane. The edge formation energy

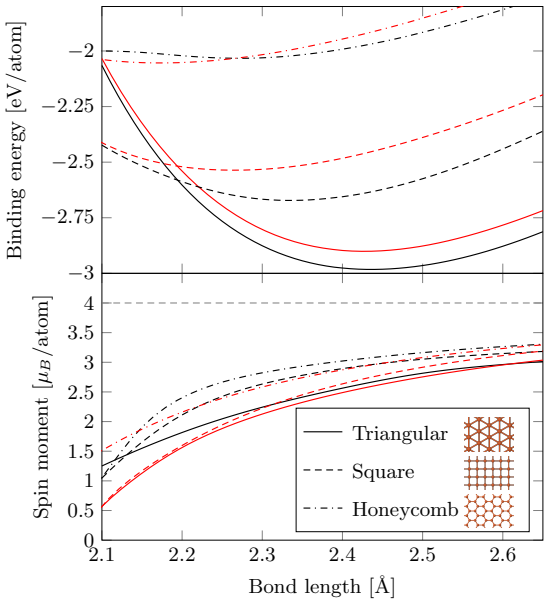

Fig. 3.14: Binding energy (upper panel) and spin moment (lower panel) of monolayer Fe as a function of bond length. The black and red lines are for ferromagnetic and antiferromagnetic ordering, respectively. The magnitude of the spin is shown in case of antiferromagnetic ordereing, as it has zero net spin. The dashed gray line indicates the spin of free Fe.

can be calculated by finding the total energy of an Fe nanoribbon E_{ribbon} and use the formula $E_{edge} = (E_{ribbon} - NE_{monolayer})/2l$, where l is the length of the unit cell in the direction of the ribbon edge, N is the number of atoms in the unit cell and $E_{monolayer}$ is the energy per atom of the monolayer system. The factor of $1/2$ comes from the fact that a nanoribbon has two edges. The edge formation energy of two rotations of both a square lattice and a triangular lattice is shown in Fig. 3.15b. The figure shows that the edge formation energy is significantly lower for the square lattice compared to the triangular lattice. At the start of the membrane formation, the edge constitutes a large part of the Fe, and it is therefore likely that the membrane is forced into a square lattice during formation and is then kinetically hindered to rearrange into a triangular lattice.

The formation of the square lattice is now more or less understood. The second issue was the bond length. In order to examine this, structural relaxation calculations are performed on small iron membranes embedded in graphene antidot lattices. The {4,2} and {5,3} GAL unit cells are used in the calculations, which should be large enough that the Fe membranes do not significantly inter-

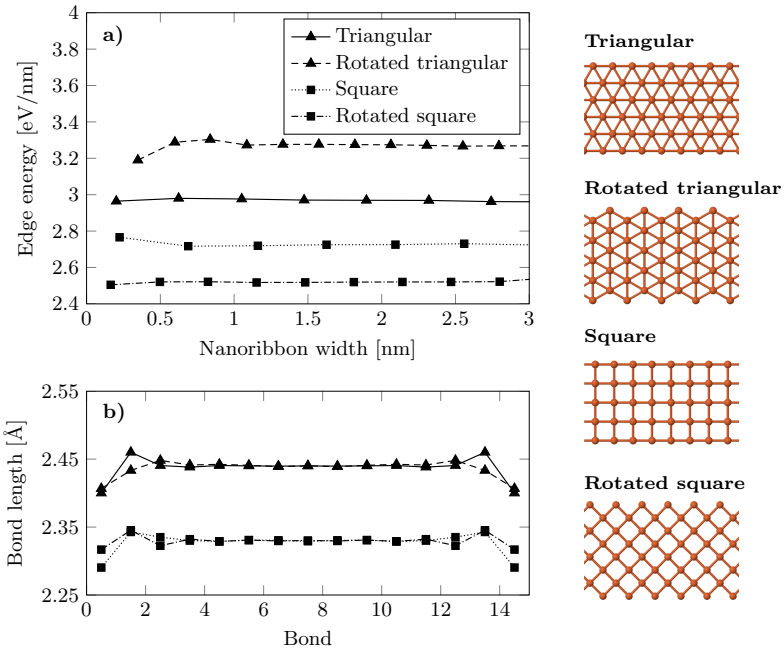

Fig. 3.15: (a) Edge formation energy for square and triangular Fe nanoribbons as a function of nanoribbon width. (b) bond lengths through a 16-atom-wide Fe nanoribbon with different orientations and edge rotations. The nanoribbon geometries are shown as reference.

act with each other. The structurally relaxed structures of 4 different structures are shown in Fig. 3.16. The relaxation was started with a symmetric square or triangular lattice. The symmetry of the unit cell is preserved during relaxation, which means that the relative stability of the square and triangular lattices in these antidots can be compared. The triangular lattice is energetically favored in the {4,2} unit cell and the square lattice is energetically favored in the {5,3} unit cell. The fact that the square lattice is favored in the large antidot, despite conforming worse to the graphene lattice, indicates that the square lattice has a larger binding energy to graphene than the triangular lattice. It is therefore assumed that the square lattice will have a greater advantage in larger antidots, where it conforms better to the graphene lattice. However, when the Fe membrane grows too large, the "bulk" 2D behavior should overcome edge or interface effects, which should lead to formation of the triangular Fe lattice. For the {5,3} unit cells, the average bond lengths are 2.7 Å and 2.6 Å for the square and triangular lattices, respectively. These bond lengths are quite close to the experimentally observed bond length of about 2.65 Å.

For magnetic applications, it is interesting to see how the magnetic moment

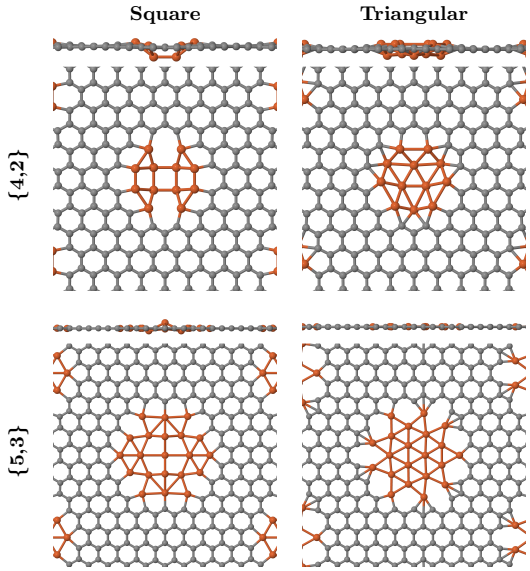

Fig. 3.16: Top and side view of structurally relaxed graphene antidots with embedded Fe. The relaxation was started with a symmetric square or triangular lattice. The symmetry of the unit cell is preserved under relaxation.

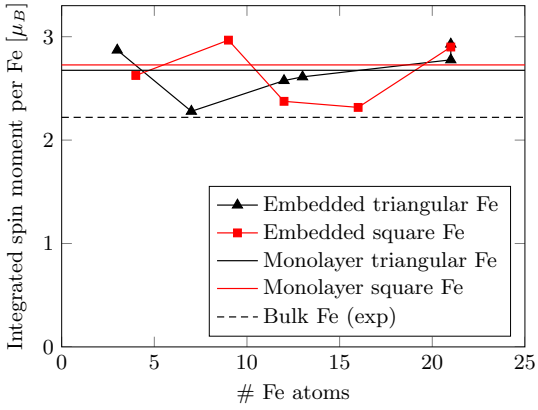

Fig. 3.17: Integrated spin moment per atom for Fe membranes embedded in graphene antidots.

of the Fe is affected by the proximity to carbon. The integrated spin moment per Fe atom is shown in Fig. 3.17 for a number of different embedded structures. Interestingly, the spin moment is always larger than for bulk Fe. In fact, the spin moment can even become larger than the freestanding monolayer system, due to the increased bond lengths in the membranes. The large magnetic moment coupled with the high conductivity of graphene as well as the experimental realization of these systems, could mean that these systems will be ideal for spintronic applications.

Chapter 4

Conclusions

Continuum models based on Dirac equation (DE) has been presented, which describes the electronic, optical and transport properties of graphene antidot lattices and graphene antidot barriers. The major advantage of the DE models are that the computational complexity is scale invariant, which allows for calculations on arbitrarily large geometries. The DE models are compared to tight-binding (TB) calculations of the corresponding atomistic structures in order to assess their accuracy. Comparisons of band structures, optical spectra and transport spectra show that the DE models are in quantitative agreement with TB for structures in the absence edge states, e.g., antidots without extended zigzag edges. The presented DE models are unable to predict edge states as they are continuum models and are therefore not able to distinguish between subtle atomistic features such as zigzag and armchair edge chirality. The presented DE models are very general as they do not impose any symmetry restrictions on the antidots. In addition, the transport model does not even require the system to be periodic; it can calculate the scattering of any arrangement of antidots. An analytical expression of the band gap of a graphene antidot lattice was derived from the DE and a linearization of this result reveals a scaling constant in good agreement with previously obtained values obtained from atomistic models. The analytic result provides a very fast way of estimating the band gap of a graphene antidot lattice without edge states, even if the antidot makes up a large fraction of the unit cell. Additionally, an analytical expression of the transport gap of graphene antidot barriers has been derived from the DE. In conclusion, the DE-based models are ideal for calculating the properties of arbitrarily large structures, but only when the effects of edge states is negligible.

It was just concluded that a DE method is able to accurately describe the electronic transport for graphene antidot systems in the absence of localized edge states. However, due to the limitations of the Dirac equation method, the TB approximation is used instead to treat systems with magnetic defects or graphene antidot lattices under a magnetic field, respectively.

Electronic transmission of graphene antidot barriers and density of states of graphene antidot lattices under an applied magnetic field have been calculated. There is, in general, a high degree of similarity between the electronic transmission and density of states spectra. However, the density of states does not offer much clue with regard to the magnitude of transmittance. Additionally, an expression of the transmittance of Dirac mass barriers in magnetic fields has been derived. It is found that this is in good agreement with TB near the onset of the transport gap of graphene antidot barriers for small antidot sizes and low to moderate field strengths. It is found that antidots support magnetic edge states, which are states that are confined to the periphery of the antidot due to an applied magnetic field. These states are found to be robust against variations in lattice configuration, antidot edge chirality, periodicity and number of antidots. Moreover, it is observed that the edge states survive a modest degree of disorder. The robustness of these states suggests that they will also be observable in experiments even in the presence of disorder. Recent experiments have found that it is possible to image electron trajectories in graphene-based systems under a magnetic field using cooled scanning probe microscopy [106, 107]. It would be remarkable if this technique could be used for direct observation of magnetic edge states. Moreover, it was found that the results scale in a simple manner with system size, thus allowing calculations on small structures to generalize to larger structures.

Spin-dependent transport of hydrogenated graphene has also been studied in the TB approximation. Hydrogen adatoms are magnetic and carries a magnetic moment of 1 μB per adatom. A simple model is used to describe hydrogen adatoms on graphene, where the only spin-dependent parameter is the on-site energy of the H adatom. As the model is simple, some of the results are expected to extend qualitatively to other magnetic impurities in graphene. By calculating the spin-dependent transmittance as a function of device length, properties such as spin relaxation length, localization length and sheet resistance can be extracted. It is demonstrated that the spin relaxation length is very short for energies around the hydrogen-induced defect bands and that the spin relaxation mechanism is exponential (Markovian) near the charge neutrality point and non-exponential (non-Markovian) otherwise. It is additionally demonstrated that the inverse spin relaxation length scale nearly linearly with

impurity concentration.

Hydrogen adatoms are only one possibility for magnetic impurities in graphene. Another common magnetic impurity is Fe, which comes from leftover residue from a common transfer process used in CVD-grown graphene. Recent experiments have shown that monolayer Fe membranes can be formed in graphene perforations. The stability of free-standing monolayer Fe and graphene-embedded Fe membranes has been studied through *ab initio* calculations in an attempt to understand the experimental results. It is found that the most stable configuration of monolayer Fe is the ferromagnetic triangular lattice with a lattice constant of 2.44 Å. This is in contrast to experimental results of graphene-embedded Fe, which show that these structures have a square lattice configuration with a bond length of 2.65 Å. However, the calculations show that the square lattice has a lower edge formation energy, which means that, during formation, it might be favorable to form the square lattice and the structure may then be kinetically hindered from subsequently rearranging to the triangular lattice. Furthermore, the stability of the square and triangular Fe lattices embedded in two different graphene antidot lattices has been compared. In the larger one of these, the square lattice is, in fact, more stable than the triangular lattice, with a mean Fe-Fe bond length of 2.7 Å. This result is in very close agreement with the experimental results. The results show that both monolayer Fe and graphene embedded Fe membranes have a larger magnetic moment per Fe than does bulk Fe. This observation, along with electronic properties of graphene, could make iron-filled GALs interesting for spintronic applications.

References

[1] L. D. Landau, Phys. Z. Sowjet. **11**, 26 (1937).

[2] L. D. Landau and E. M. Lifshitz, *Statistical physics*, 3rd ed. (Butterworth-Heinemann (Oxford), 1980).

[3] P. R. Wallace, Phys. Rev. **71**, 622 (1947).

[4] H. P. Boehm, A. Clauss, G. O. Fischer, and U. Hofmann, Z. Naturforsch. **17**, 150 (1962).

[5] H. P. Boehm, A. Clauss, G. O. Fischer, and U. Hofmann, Z. Anorg. Allg. Chem. **316**, 119 (1962).

[6] K. S. Novoselov, a. K. Geim, S. V. Morozov, D. Jiang, Y. Zhang, S. V. Dubonos, I. V. Grigorieva, and A. A. Firsov, Science **306**, 666 (2004).

[7] Nobel Media AB, "The 2010 nobel prize in physics – press release," `http://www.nobelprize.org/nobel_prizes/physics/laureates/2010/press.pdf` (2010).

[8] L. Wang, I. Meric, P. Y. Huang, Q. Gao, Y. Gao, H. Tran, T. Taniguchi, K. Watanabe, L. M. Campos, D. A. Muller, J. Guo, P. Kim, J. Hone, K. L. Shepard, and C. R. Dean, Science **342**, 614 (2013).

[9] B. Dlubak, M.-B. Martin, C. Deranlot, B. Servet, S. Xavier, R. Mattana, M. Sprinkle, C. Berger, W. A. De Heer, F. Petroff, *et al.*, Nat. Phys. **8**, 557 (2012).

[10] L. Yang, C.-H. Park, Y.-W. Son, M. L. Cohen, and S. G. Louie, Phys. Rev. Lett. **99**, 186801 (2007).

[11] B. Obradovic, R. Kotlyar, F. Heinz, P. Matagne, T. Rakshit, M. D. Giles, M. A. Stettler, and D. E. Nikonov, Appl. Phys. Lett. **88**, 142102 (2006).

[12] Y.-W. Son, M. L. Cohen, and S. G. Louie, Phys. Rev. Lett. **97**, 216803 (2006).

[13] M. Y. Han, B. Özyilmaz, Y. Zhang, and P. Kim, Phys. Rev. Lett. **98**, 206805 (2007).

[14] E. V. Castro, K. S. Novoselov, S. V. Morozov, N. M. R. Peres, J. M. B. L. Dos Santos, J. Nilsson, F. Guinea, A. K. Geim, and A. H. C. Neto, Phys. Rev. Lett. **99**, 216802 (2007).

[15] Y. Zhang, T.-T. Tang, C. Girit, Z. Hao, M. C. Martin, A. Zettl, M. F. Crommie, Y. R. Shen, and F. Wang, Nature **459**, 820 (2009).

[16] K. F. Mak, C. H. Lui, J. Shan, and T. F. Heinz, Phys. Rev. Lett. **102**, 256405 (2009).

[17] C. H. Lui, Z. Li, K. F. Mak, E. Cappelluti, and T. F. Heinz, Nat. Phys. **7**, 944 (2011).

[18] J. G. Pedersen and T. G. Pedersen, Phys. Rev. B **85**, 235432 (2012).

[19] Z. H. Ni, T. Yu, Y. H. Lu, Y. Y. Wang, Y. P. Feng, and Z. X. Shen, ACS nano **2**, 2301 (2008).

[20] G. Gui, J. Li, and J. Zhong, Phys. Rev. B **78**, 075435 (2008).

[21] R. Balog, B. Jørgensen, L. Nilsson, M. Andersen, E. Rienks, M. Bianchi, M. Fanetti, E. Lægsgaard, A. Baraldi, S. Lizzit, Z. Sljivancanin, F. Besenbacher, B. Hammer, T. G. Pedersen, P. Hofmann, and L. Hornekær, Nat. Mater. **9**, 315 (2010).

[22] G. Giovannetti, P. A. Khomyakov, G. Brocks, P. J. Kelly, and J. van den Brink, Phys. Rev. B **76**, 073103 (2007).

[23] S. Y. Zhou, G.-H. Gweon, A. V. Fedorov, P. N. First, W. A. De Heer, D.-H. Lee, F. Guinea, A. H. C. Neto, and A. Lanzara, Nat. Mat. **6**, 770 (2007).

[24] T. G. Pedersen, C. Flindt, J. Pedersen, N. A. Mortensen, A.-P. Jauho, and K. Pedersen, Phys. Rev. Lett. **100**, 136804 (2008).

[25] J. A. Fürst, T. G. Pedersen, M. Brandbyge, and A.-P. Jauho, Phys. Rev. B **80**, 115117 (2009).

[26] T. G. Pedersen, A. P. Jauho, and K. Pedersen, Phys. Rev. B **79**, 113406 (2009).

[27] T. G. Pedersen, C. Flindt, J. Pedersen, A.-P. Jauho, N. A. Mortensen, and K. Pedersen, Phys. Rev. B **77**, 245431 (2008).

[28] J. G. Pedersen, T. Gunst, T. Markussen, and T. G. Pedersen, Phys. Rev. B **86**, 245410 (2012).

[29] T. G. Pedersen and J. G. Pedersen, J. Appl. Phys. **112**, 113715 (2012).

[30] F. Ouyang, S. Peng, Z. Liu, and Z. Liu, ACS nano **5**, 4023 (2011).

[31] R. Petersen and T. G. Pedersen, Phys. Rev. B **80**, 113404 (2009).

[32] M. L. Trolle, U. S. Møller, and T. G. Pedersen, Phys. Rev. B **88**, 195418 (2013).

[33] J. G. Pedersen and T. G. Pedersen, Phys. Rev. B **87**, 235404 (2013).

[34] S. Yuan, R. Roldán, A.-P. Jauho, and M. Katsnelson, Phys. Rev. B **87**, 085430 (2013).

[35] J. A. Fürst, J. G. Pedersen, C. Flindt, N. A. Mortensen, M. Brandbyge, T. G. Pedersen, and A.-P. Jauho, New J. Phys. **11**, 095020 (2009).

[36] X. Liu, Z. Zhang, and W. Guo, Small , 1405 (2013).

[37] T. Gunst, T. Markussen, A.-P. Jauho, and M. Brandbyge, Phys. Rev. B **84**, 155449 (2011).

[38] S. R. Power and A.-P. Jauho, Phys. Rev. B **90**, 115408 (2014).

[39] R. Petersen, T. G. Pedersen, and A.-P. Jauho, ACS Nano **5**, 523 (2010).

[40] M. Dvorak, W. Oswald, and Z. Wu, Sci. Rep. **3** (2013).

[41] H. Karamitaheri, M. Pourfath, R. Faez, and H. Kosina, J. Appl. Phys. **110**, 054506 (2011).

[42] J. V. Gomes and N. M. R. Peres, J. Phys: Condens. Matter **20**, 325221 (2008).

[43] M. Kim, N. S. Safron, E. Han, M. S. Arnold, and P. Gopalan, Nano Lett. **10**, 1125 (2010).

[44] Q. Xu, M.-Y. Wu, G. F. Schneider, L. Houben, S. K. Malladi, C. Dekker, E. Yucelen, R. E. Dunin-Borkowski, and H. W. Zandbergen, ACS Nano **7**, 1566 (2013).

[45] A. J. M. Giesbers, E. C. Peters, M. Burghard, and K. Kern, Phys. Rev. B **86**, 045445 (2012).

[46] M. Kim, N. S. Safron, E. Han, M. S. Arnold, and P. Gopalan, ACS Nano **6**, 9846 (2012).

[47] J. Eroms and D. Weiss, New J. Phys. **11**, 095021 (2009).

[48] F. Oberhuber, S. Blien, S. Heydrich, F. Yaghobian, T. Korn, C. Schüller, C. Strunk, D. Weiss, and J. Eroms, Appl. Phys. Lett. **103**, 143111 (2013).

[49] J. Bai, X. Zhong, S. Jiang, Y. Huang, and X. Duan, Nat. Nanotechnol. **5**, 190 (2010).

[50] M. Wang, L. Fu, L. Gan, C. Zhang, M. Rümmeli, A. Bachmatiuk, K. Huang, Y. Fang, and Z. Liu, Sci. Rep. **3**, 1238 (2013).

[51] Z. Zeng, X. Huang, Z. Yin, H. Li, Y. Chen, H. Li, Q. Zhang, J. Ma, F. Boey, and H. Zhang, Adv. Mater. **24**, 4138 (2012).

[52] R. Yagi, R. Sakakibara, R. Ebisuoka, J. Onishi, K. Watanabe, T. Taniguchi, and Y. Iye, Phys. Rev. B **92**, 195406 (2015).

[53] A. Sandner, T. Preis, C. Schell, P. Giudici, K. Watanabe, T. Taniguchi, D. Weiss, and J. Eroms, Nano Lett. **15**, 8402 (2015).

[54] R. K. Paul, S. Badhulika, N. M. Saucedo, and A. Mulchandani, Anal. Chem. **84**, 8171 (2012).

[55] S. Heydrich, M. Hirmer, C. Preis, T. Korn, J. Eroms, D. Weiss, and C. Schüller, Appl. Phys. Lett. **97**, 043113 (2010).

[56] X. Liang, Y.-S. Jung, S. Wu, A. Ismach, D. L. Olynick, S. Cabrini, and J. Bokor, Nano Lett. **10**, 2454 (2010).

[57] M. Bieri, M. Treier, J. Cai, K. Aït-Mansour, P. Ruffieux, O. Gröning, P. Gröning, M. Kastler, R. Rieger, X. Feng, *et al.*, Chem. Commun. , 6919 (2009).

[58] Z. Shi, R. Yang, L. Zhang, Y. Wang, D. Liu, D. Shi, E. Wang, and G. Zhang, Adv. Mater. **23**, 3061 (2011).

[59] X. Jia, M. Hofmann, V. Meunier, B. G. Sumpter, J. Campos-Delgado, J. M. Romo-Herrera, H. Son, Y.-P. Hsieh, A. Reina, J. Kong, *et al.*, Science **323**, 1701 (2009).

[60] Ç. Ö. Girit, J. C. Meyer, R. Erni, M. D. Rossell, C. Kisielowski, L. Yang, C.-H. Park, M. Crommie, M. L. Cohen, S. G. Louie, *et al.*, Science **323**, 1705 (2009).

[61] A. P. Seitsonen, A. M. Saitta, T. Wassmann, M. Lazzeri, and F. Mauri, Phys. Rev. B **82**, 115425 (2010).

[62] F. Schwierz, Nat. Nanotechnol. **5**, 487 (2010).

[63] S. Berrada, V. H. Nguyen, D. Querlioz, J. Saint-Martin, A. Alarcón, C. Chassat, A. Bournel, and P. Dollfus, Appl. Phys. Lett. **103**, 183509 (2013).

[64] W. Han, R. K. Kawakami, M. Gmitra, and J. Fabian, Nat. Nanotechnol. **9**, 794 (2014).

[65] M. H. D. Guimarães, P. J. Zomer, J. Ingla-Aynés, J. C. Brant, N. Tombros, and B. J. van Wees, Phys. Rev. Lett. **113**, 086602 (2014).

[66] M. Drögeler, F. Volmer, M. Wolter, B. Terrés, K. Watanabe, T. Taniguchi, G. Güntherodt, C. Stampfer, and B. Beschoten, Nano Lett. (2014).

[67] N. Tombros, C. Jozsa, M. Popinciuc, H. T. Jonkman, and B. J. Van Wees, Nature **448**, 571 (2007).

[68] M. Weser, E. N. Voloshina, K. Horn, and Y. S. Dedkov, Phys. Chem. Chem. Phys. **13**, 7534 (2011).

[69] J. Zhou, Q. Wang, Q. Sun, X. Chen, Y. Kawazoe, and P. Jena, Nano Lett. **9**, 3867 (2009).

[70] P. O. Lehtinen, A. S. Foster, Y. Ma, A. V. Krasheninnikov, and R. M. Nieminen, Phys. Rev. Lett. **93**, 187202 (2004).

[71] S. Haldar, B. S. Pujari, S. Bhandary, F. Cossu, O. Eriksson, D. G. Kanhere, and B. Sanyal, Phys. Rev. B **89**, 205411 (2014).

[72] I. Zanella, S. B. Fagan, R. Mota, and A. Fazzio, J. Phys. Chem. C **112**, 9163 (2008).

[73] A. V. Krasheninnikov, P. O. Lehtinen, A. S. Foster, P. Pyykkö, and R. M. Nieminen, Phys. Rev. Lett. **102**, 126807 (2009).

[74] E. J. G. Santos, A. Ayuela, and D. Sánchez-Portal, New J. Phys. **12**, 053012 (2010).

[75] Z. He, K. He, A. W. Robertson, A. I. Kirkland, D. Kim, J. Ihm, E. Yoon, G.-D. Lee, and J. H. Warner, Nano Lett. **14**, 3766 (2014).

[76] J. A. Rodrígues-Manzo, O. Cretu, and F. Banhart, ACS nano **4**, 3422 (2010).

[77] S. B. Fagan, R. Mota, A. J. R. da Silva, and A. Fazzio, Phy. Rev. B **67**, 205414 (2003).

[78] A. W. Robertson, B. Montanari, K. He, J. Kim, C. S. Allen, Y. A. Wu, J. Olivier, J. Neethling, N. Harrison, A. I. Kirkland, *et al.*, Nano Lett. **13**, 1468 (2013).

[79] J. Zhao, Q. Deng, A. Bachmatiuk, G. Sandeep, A. Popov, J. Eckert, and M. H. Rümmeli, Science **343**, 1228 (2014).

[80] D. Huertas-Hernando, F. Guinea, and A. Brataas, Phys. Rev. Lett. **103**, 146801 (2009).

[81] P. Zhang and M. Wu, Phys. Rev. B **84**, 045304 (2011).

[82] M. Wojtaszek, I. J. Vera-Marun, T. Maassen, and B. J. van Wees, Phys. Rev. B **87**, 081402 (2013).

[83] N. Tombros, S. Tanabe, A. Veligura, C. Jozsa, M. Popinciuc, H. T. Jonkman, and B. J. Van Wees, Phys. Rev. Lett. **101**, 046601 (2008).

[84] W. Han and R. K. Kawakami, Phys. Rev. Lett. **107**, 047207 (2011).

[85] M. Wojtaszek, I. J. Vera-Marun, E. Whiteway, M. Hilke, and B. J. van Wees, Phy. Rev. B **89**, 035417 (2014).

[86] P. J. Zomer, M. H. D. Guimaraes, N. Tombros, and B. J. van Wees, Phys. Rev. B **86**, 161416 (2012).

[87] S. Lara-Avila, S. Kubatkin, O. Kashuba, R. Yakimova, T. J. B. M. Janssen, A. Tzalenchuk, and V. Fal'ko, arXiv:1507.03841 (2015).

[88] D. Kochan, M. Gmitra, and J. Fabian, Phys. Rev. Lett. **112**, 116602 (2014).

[89] D. Soriano, N. Leconte, P. Ordejón, J.-C. Charlier, J.-J. Palacios, and S. Roche, Phys. Rev. Lett. **107**, 016602 (2011).

[90] D. Soriano, D. Van Tuan, S. M.-M. Dubois, M. Gmitra, A. W. Cummings, D. Kochan, F. Ortmann, J.-C. Charlier, J. Fabian, and S. Roche, arXiv:1504.01591 (2015).

[91] T. Taychatanapat, K. Watanabe, T. Taniguchi, and P. Jarillo-Herrero, Nat. Phys. **9**, 225 (2013).

[92] K. S. Novoselov, Z. Jiang, Y. Zhang, S. V. Morozov, H. L. Stormer, U. Zeitler, J. C. Maan, G. S. Boebinger, P. Kim, and A. K. Geim, Science **315**, 1379 (2007).

[93] C. R. Dean, A. F. Young, P. Cadden-Zimansky, L. Wang, H. Ren, K. Watanabe, T. Taniguchi, P. Kim, J. Hone, and K. L. Shepard, Nature Phys. **7**, 693 (2011).

[94] X. Du, I. Skachko, F. Duerr, A. Luican, and E. Y. Andrei, Nature **462**, 192 (2009).

[95] J. Baringhaus, M. Settnes, J. Aprojanz, S. R. Power, A.-P. Jauho, and C. Tegenkamp, Phys. Rev. Lett. **116**, 186602 (2016).

[96] S. İslamoğlu, M. Ö. Oktel, and O. Gülseren, Phys. Rev. B **85**, 235414 (2012).

[97] Z. Z. Zhang, K. Chang, and F. M. Peeters, Phys. Rev. B **77**, 235411 (2008).

[98] J. G. Pedersen and T. G. Pedersen, Phys. Rev. B **85**, 035413 (2012).

[99] D. R. Hofstadter, Phys. Rev. B **14**, 2239 (1976).

[100] Y. Takagaki and D. K. Ferry, Surf. Sci. **305**, 669 (1994).

[101] E. N. Bogachek and U. Landman, Phys. Rev. B **52**, 14067 (1995).

[102] S. Ishizaka and T. Ando, Phys. Rev. B **55**, 16331 (1997).

[103] D. Weiss, M. L. Roukes, A. Menschig, P. Grambow, K. von Klitzing, and G. Weimann, Phys. Rev. Lett. **66**, 2790 (1991).

[104] F. Nihey and K. Nakamura, Physica B **184**, 398 (1993).

[105] R. Schuster, K. Ensslin, D. Wharam, S. Kühn, J. P. Kotthaus, G. Böhm, W. Klein, G. Tränkle, and G. Weimann, Phys. Rev. B **49**, 8510 (1994).

[106] S. Bhandari, G. Lee, A. Klales, K. Watanabe, T. Taniguchi, E. Heller, P. Kim, and R. Westervelt, Nano Lett. **16**, 1690 (2016).

[107] S. Morikawa, Z. Dou, S.-W. Wang, C. G. Smith, K. Watanabe, T. Taniguchi, S. Masubuchi, T. Machida, and M. R. Connolly, Appl. Phys. Lett. **107**, 243102 (2015).

[108] H. Xu, T. Heinzel, M. Evaldsson, and I. V. Zozoulenko, Phys. Rev. B **77**, 245401 (2008).

[109] M. R. Thomsen, S. J. Brun, and T. G. Pedersen, J. Phys.: Condens. Matter **26**, 335301 (2014).

[110] M. R. Thomsen, M. M. Ervasti, A. Harju, and T. G. Pedersen, Phys. Rev. B **92**, 195408 (2015).

[111] S. Datta, *Electronic transport in mesoscopic systems* (Cambridge University Press, Cambridge, UK, 1995).

[112] T. Markussen, R. Rurali, M. Brandbyge, and A.-P. Jauho, Phys. Rev. B **74**, 245313 (2006).

[113] C. H. Lewenkopf and E. R. Mucciolo, J. Comput. Electron. **12**, 203 (2013).

[114] M. R. Masir, A. Matulis, and F. M. Peeters, Phys. Rev. B **84**, 245413 (2011).

[115] R. L. Heinisch, F. X. Bronold, and H. Fehske, Phys. Rev. B **87**, 155409 (2013).

[116] P. Hohenberg and W. Kohn, Phys. Rev. **136**, B864 (1964).

[117] W. Kohn and L. J. Sham, Phys. Rev. **140**, A1133 (1965).

[118] X. Gonze, B. Amadon, P. M. Anglade, J. M. Beuken, F. Bottin, P. Boulanger, F. Bruneval, D. Caliste, R. Caracas, M. Cote, T. Deutsch, L. Genovese, P. Ghosez, M. Giantomassi, S. Goedecker, D. Hamann, P. Hermet, F. Jollet, G. Jomard, S. Leroux, M. Mancini, S. Mazevet, M. J. T. Oliveira, G. Onida, Y. Pouillon, T. Rangel, G. M. Rignanese, D. Sangalli, R. Shaltaf, M. Torrent, M. J. Verstraete, G. Zérah, and J. W. Zwanziger, Comput. Phys. Commun. **180**, 2582 (2009).

[119] X. Gonze, J.-M. Beuken, R. Caracas, F. Detraux, M. Fuchs, G.-M. Rignanese, L. Sindic, M. Verstraete, G. Zerah, F. Jollet, M. Torrent, A. Roy, M. Mikami, P. Ghosez, J. Y. Raty, and D. C. Allan, Comput. Mater. Sci. **25**, 478 (2002).

[120] S. Reich, J. Maultzsch, C. Thomsen, and P. Ordejon, Physical Review B **66**, 035412 (2002).

[121] R. Saito, G. Dresselhaus, and M. S. Dresselhaus, *Physical properties of carbon nanotubes*, Vol. 35 (World Scientific, 1998).

[122] R. Haydock, Comput. Phys. Commun. **20**, 11 (1980).

[123] A. Weiße, G. Wellein, A. Alvermann, and H. Fehske, Rev. Mod. Phys. **78**, 275 (2006).

[124] Z. Fan, A. Uppstu, T. Siro, and A. Harju, Comput. Phys. Commun. **185**, 28 (2014).

[125] S.-W. Lee and R. Mittra, IEEE T. Antenn. Propag. **31**, 99 (1983).

[126] L. Novotny and B. Hecht, *Principles of nano-optics* (Cambridge University Press, 2006).

[127] T. Søndergaard, Phys. Stat. Sol. **244**, 3448 (2007).

[128] K. Yasumoto and K. Yoshitomi, IEEE T. Antenn. Propag. **47**, 1050 (1999).

[129] H. A. Van der Vorst, SIAM Journal on scientific and Statistical Computing **13**, 631 (1992).

[130] H. C. Elman, D. J. Silvester, and A. J. Wathen, (2005).

[131] B. T. Draine, Astrophys. J. **333**, 848 (1988).

[132] M. Petravic and G. Kuo-Petravic, J. Comput. Phys. **32**, 263 (1979).

[133] M. P. L. Sancho, J. M. L. Sancho, and J. Rubio, J. Phys. F: Met. Phys. **15**, 851 (1985).

[134] T. N. Todorov, J. Phys.: Cond. Mat. **14**, 3049 (2002).

[135] W. H. Zurek, F. M. Cucchietti, and J. P. Paz, Acta Phys. Pol. B **38**, 1685 (2007).

[136] M. Fujita, K. Wakabayashi, K. Nakada, and K. Kusakabe, J. Phys. Soc. Jap. **65**, 1920 (1996).

[137] L. Brey and H. A. Fertig, Phys. Rev. B **73**, 235411 (2006).

[138] M. Vanević, V. M. Stojanović, and M. Kindermann, Phys. Rev. B **80**, 045410 (2009).

Publications

List of publications

[I] S. J. Brun, **M. R. Thomsen** and T. G. Pedersen, *Electronic and optical properties of graphene antidot lattices: comparison of Dirac and tight-binding models*, J. Phys. Condens. Matter **26**, 335301 (2014).

[II] **M. R. Thomsen**, S. J. Brun and T. G. Pedersen, *Dirac model of electronic transport in graphene antidot barriers*, J. Phys. Condens. Matter **26**, 265301 (2014).

[III] **M. R. Thomsen**, S. J. Brun and T. G. Pedersen, *Stability and magnetization of free-standing and graphene-embeded iron membranes*, Phys. Rev. B **91**, 125439 (2915).

[IV] **M. R. Thomsen**, M. M. Ervasti, A. Harju and T. G. Pedersen, *Spin transport in hydrogenated graphene*, *Phys. Rev. B* **92**, 195408 (2015).

[V] **M. R. Thomsen**, S. R. Power, A.-P. Jauho and T. G. Pedersen, *Magnetic edge states and magnetotransport in graphene antidot barriers*, Phys. Rev. B **94**, 045438 (2016).

Publication I

Electronic and optical properties of graphene antidot lattices: comparison of Dirac and tight-binding models

Søren Jacob Brun, Morten Rishøj Thomsen and Thomas Garm Pedersen

The paper has been published in
Journal of Physics: Condensed matter **26**, 265301 (2014).

IOP Publishing Journal of Physics: Condensed Matter
J. Phys.: Condens. Matter **26** (2014) 265301 (8pp) doi:10.1088/0953-8984/26/26/265301

Electronic and optical properties of graphene antidot lattices: comparison of Dirac and tight-binding models

S J Brun, M R Thomsen and T G Pedersen

Department of Physics and Nanotechnology, Aalborg University, Skjernvej 4A, DK-9220 Aalborg Øst, Denmark
Center for Nanostructured Graphene (CNG), DK-9220 Aalborg Øst, Denmark

E-mail: sjb@nano.aau.dk

Received 3 March 2014, revised 21 April 2014
Accepted for publication 25 April 2014
Published 9 June 2014

Abstract
The electronic properties of graphene may be changed from semimetallic to semiconducting by introducing perforations (antidots) in a periodic pattern. The properties of such graphene antidot lattices (GALs) have previously been studied using atomistic models, which are very time consuming for large structures. We present a continuum model that uses the Dirac equation (DE) to describe the electronic and optical properties of GALs. The advantages of the Dirac model are that the calculation time does not depend on the size of the structures and that the results are scalable. In addition, an approximation of the band gap using the DE is presented. The Dirac model is compared with nearest-neighbour tight-binding (TB) in order to assess its accuracy. Extended zigzag regions give rise to localized edge states, whereas armchair edges do not. We find that the Dirac model is in quantitative agreement with TB for GALs without edge states, but deviates for antidots with large zigzag regions.

Keywords: graphene, antidot lattice, band gap, Dirac equation

(Some figures may appear in colour only in the online journal)

1. Introduction

Graphene has been the subject of intense research since it was discovered a decade ago [1]. This novel two-dimensional material has remarkable electronic [2, 3], optical [4] and mechanical [5] properties. Consequently, it finds potential applications within e.g. electronics and optoelectronics [6]. The excellent electronic properties of graphene, especially its very high mobility, make it ideally suited for new smaller and faster nanoelectronic devices [1–3]. Due to its semi-metallic nature, pristine graphene is not well-suited for semiconductor applications. Several strategies for introducing a band gap have been proposed, including graphene nanoribbons (GNRs) [7–9], gated bilayer graphene [10] and periodic gating [11]. Alternatively, an energy gap may be created using graphene quantum dots, or graphene nanodisks, which also show promising results as hosts for spin qubits [12–15]. Another method is to introduce perforations in a periodic pattern, called a graphene antidot lattice (GAL) [16, 17]. This provides a controllable band gap that depends on the geometry of the antidot lattice [16]. Previously, tight-binding (TB) calculations have been made for relatively small unit cells [16–18]. Trolle *et al* [19] have used density functional theory (DFT) and Hubbard TB to show that localized edge states emerge in GALs containing hexagonal antidots with zigzag edges. However, realistic structures are typically much larger than the ones studied theoretically, and the calculation time scales badly with the size of the structures. Fürst *et al* [18] have previously presented an analysis based on the Dirac equation (DE), in which they used finite-element analysis to calculate the electronic properties of GALs with circular antidots. The computational time of their method depends only on the ratio between the radius of the antidot and the size of the unit cell, but their method only qualitatively predicts the band structure.

Recently, GALs with circular antidots have been fabricated by several groups [20–23]. Such structures are fabricated either by e-beam lithography [20, 21] or using diblock copolymer templates [22, 23]. Moreover, Oberhuber *et al* [24] have fabricated

GALs with hexagonal antidots. They used an etching technique that selectively etches armchair edges, which produces hexagonal antidots with zigzag edges. Xu *et al* [25] have demonstrated that it is possible to create antidots with diameters down to 2 nm using a scanning transmission electron microscope. When subsequently heating the sample, the curved edges of the antidots were observed to reconstruct into armchair edges. It has also been shown that Joule heating reconstructs graphene edges into zigzag or armchair configurations [26]. Theoretical studies based on DFT show that the preferred edge chirality of GNRs is armchair in an oxygen-rich atmosphere and zigzag for water-saturated GNRs [27]. Although there may still remain some edge roughness, these findings show that the chirality of the edges of GNRs and GALs is controllable.

In this paper, we present a continuum model of GALs based on the DE. In this method, the antidot lattice is modelled by a spatially varying mass term that is only nonzero inside the antidots. This makes the antidot regions increasingly unfavourable for electrons as the mass term increases. The major advantage of the Dirac model is that the calculation time does not depend on the size of the structure that is being studied. In fact, for energies much smaller than the mass term, the results are scalable. This means that, for example, a given band structure can be used to describe a geometry where all lengths are scaled by some factor if the energies are divided by the same factor. The Dirac model is compared with nearest-neighbour TB in order to assess its accuracy. The two models will mainly be compared for GALs containing hexagonal antidots with zigzag or armchair edges. Furthermore, the DE is used to derive an approximation of the band gap of GALs, which is compared with TB for a wide range of structures. We demonstrate that the Dirac model is in quantitative agreement with TB for GALs containing antidots with armchair edges. However, for other antidot geometries, the models only agree for small antidots. We use TB to calculate the band gap of a large range of geometries, and obtain gaps ranging between practically zero and 2.25 eV. However, experimentally feasible structures result in a band gap on the order of 100 meV.

2. Theory and methods

In the present work, we will model GALs using the DE and compare the results with nearest-neighbour TB. We use the notation GAL to describe structures where the antidot lattice vectors are parallel to the carbon–carbon bonds. By rotating the lattice $\pi/6$, the antidot lattice vectors are perpendicular to the carbon–carbon bonds. These structures will be denoted rotated GALs (RGALs) as in [28]. We will focus on GALs containing hexagonal antidots with zigzag and armchair edges, which we will refer to as zigzag and armchair antidots throughout the paper. Figure 1 shows examples of GALs with zigzag and armchair antidots used in TB and the Dirac model. GALs with circular antidots and RGALs with armchair antidots will also be considered. The structures are described by the side length L of the unit cell and the side length S of the antidot, where all distances are in units of the graphene lattice constant a. Circular antidots are correspondingly

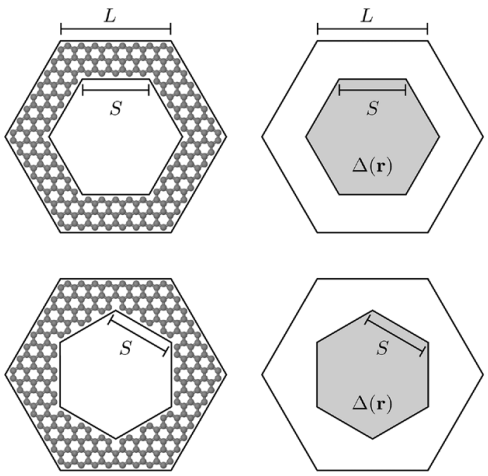

Figure 1. Unit cells used in TB (left) and DE (right) for hexagonal antidots with zigzag (top) and armchair (bottom) edges in triangular antidot lattices. The atomic structures shown are Z{8, 5}GAL and A{8, 5}GAL.

characterized by the radius R. The unit cells for TB are generated by removing all atoms within the antidot region and subsequently removing dangling bonds. The notations Z{L, S}GAL and A{L, S}GAL will be used to describe the geometry of GALs with zigzag and armchair antidots, respectively. Furthermore, the notations C{L, R}GAL and A{L, S}RGAL will describe GALs with circular antidots and RGALs with armchair antidots, respectively.

The Dirac Hamiltonian for a graphene lattice with a spatially varying mass term $\Delta(\mathbf{r})$ has the form [18]

$$\mathbf{H} = \begin{pmatrix} \Delta(\mathbf{r}) & -\hbar v_{\mathrm{F}}\left(\mathrm{i}\partial_x - \partial_y\right) \\ -\hbar v_{\mathrm{F}}\left(\mathrm{i}\partial_x + \partial_y\right) & -\Delta(\mathbf{r}) \end{pmatrix}, \tag{1}$$

where the mass term has a constant value of Δ_0 inside the antidot and is vanishing elsewhere. The wave function Ψ will satisfy the Bloch condition if $\Psi(\mathbf{r}) = \mathrm{e}^{\mathrm{i}\mathbf{k}\cdot\mathbf{r}}u(\mathbf{r})$, where the function $u(\mathbf{r})$ is a lattice-periodic spinor containing the components $u^A(\mathbf{r})$ and $u^B(\mathbf{r})$. We then express $\Delta(\mathbf{r})$ and $u(\mathbf{r})$ as Fourier series, as they are both periodic with the antidot lattice

$$\Delta(\mathbf{r}) = \sum_{\mathbf{G}} \Delta_{\mathbf{G}} e^{\mathrm{i}\mathbf{G}.\mathbf{r}}, \quad u(\mathbf{r}) = \sum_{\mathbf{G}} u_{\mathbf{G}} \mathrm{e}^{\mathrm{i}\mathbf{G}.\mathbf{r}}, \tag{2}$$

where $u_{\mathbf{G}}$ is a spinor containing the Fourier coefficients $u_{\mathbf{G}}^A$ and $u_{\mathbf{G}}^B$, $\mathbf{G} = p\mathbf{g}_1 + q\mathbf{g}_2$ is the reciprocal lattice vector, p and q are integers, and $\mathbf{g}_1$ and $\mathbf{g}_2$ are the primitive reciprocal lattice vectors of the antidot lattice. The geometry of the antidot is then solely described by the Fourier coefficients $\Delta_{\mathbf{G}}$ and the geometry of the unit cell is solely described by $\mathbf{g}_1$ and $\mathbf{g}_2$. The expression for $\Delta_{\mathbf{G}}$ for an arbitrary N-sided polygon was derived in [29]. Inserting the expressions for $\Delta(\mathbf{r})$ and $\Psi(\mathbf{r})$ in the Dirac equation $\mathbf{H}\Psi = E\Psi$ leads to the expression

$$\sum_{\mathbf{G}'} \mathbf{H}_{\mathbf{G},\mathbf{G}'} u_{\mathbf{G}'} = E u_{\mathbf{G}}, \tag{3}$$

$$\mathbf{H}_{\mathbf{G},\mathbf{G}'} = \begin{pmatrix} \Delta_{\mathbf{G}-\mathbf{G}'} & T_{\mathbf{G}}\delta_{\mathbf{G},\mathbf{G}'} \\ T^{*}_{\mathbf{G}}\delta_{\mathbf{G},\mathbf{G}'} & -\Delta_{\mathbf{G}-\mathbf{G}'} \end{pmatrix}, \quad (4)$$

where $T_{\mathbf{G}} = \hbar v_{\mathrm{F}}[k_x + G_x - \mathrm{i}(k_y + G_y)]$. This may be set up as a matrix equation and solved as an eigenvalue problem through numerical diagonalization. Electrons are excluded more and more from the antidot region as the mass term increases, and in the limit of an infinite mass term, the electrons are completely excluded. Therefore, convergence is obtained by using a sufficiently large mass term. However, convergence must also be ensured by choosing a basis that is large enough. Throughout the paper we use a mass term given by $\Delta_0 = 170$ eV L^{-1}. The reciprocal lattice vectors used for the basis are created by letting $p, q \in [-N, N]$, where we use $N = 20$ and $N = 16$ for hexagonal and circular antidots, respectively. These parameters were found to provide adequately converged results.

Our method is different from the one used by Fürst *et al* [18], who studied GALs with circular antidots using the DE. They used the commercially available finite-element solver COMSOL Multiphysics for their calculations. They studied the case of an infinite mass term by imposing the boundary condition that the current normal to the edge of the antidot is vanishing. This method was shown to provide results that agree qualitatively, but not quantitatively, with TB. Their boundary condition states that $\Psi_A(\mathbf{r}) = \mathrm{i}\mathrm{e}^{-\mathrm{i}\phi}\Psi_B(\mathbf{r})$, where $\Psi_{A/B}(\mathbf{r})$ are the two spinor components of the wave function and ϕ is the polar angle of the normal vector at a given point on the edge of the antidot. This was shown to be problematic in the limit of vanishing antidots where the angle ϕ becomes completely undetermined. In this case, the band gap was non-vanishing and approached a value of approximately $1.02\gamma/L$, where γ is the transfer integral of nearest-neighbour TB. Our method uses a finite mass term. However, in the limit of an infinite mass term, the two approaches should be equivalent, and in this case our method should also show a finite band gap in the limit of vanishing antidots. In practice, we cannot use an infinite mass term, as this would require an infinite basis. Because our model uses a finite mass term, we do not encounter the same problem in the limit of vanishing antidots.

We have focused our attention on hexagonal antidots, although other geometries may easily be considered by adjusting the Fourier coefficients of the mass term accordingly. An approximation of the band gap of a GAL is derived in appendix A from the DE by assuming cylindrical symmetry in the unit cell.

The atomistic model used for comparison is nearest-neighbour TB in the orthogonal approximation (assuming no overlap between atomic wave functions) with a transfer integral of $\gamma = 3.033$ eV.

3. Results

In this section, we present the results of our Dirac model and compare them with TB. Only positive energies of band structures will be shown, as the valence bands follow from exact electron-hole symmetry. We will present results for GALs with zigzag and armchair antidots, as well as GALs with circular antidots and RGALs with armchair antidots.

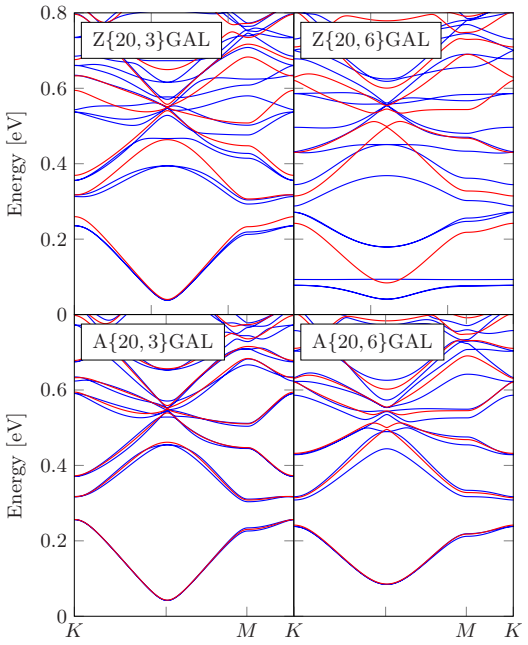

Figure 2. Comparison of DE (red) and TB (blue) band structures for GALs with zigzag and armchair antidots.

Band structures calculated using the DE and TB are compared in figure 2 for four different geometries. The geometries used for the Dirac model are created such that the area of the antidot equals the total area of the removed atoms. For all four geometries shown, a band gap opens up at the Γ-point both for the DE and TB calculations. In the case of zigzag antidots, the Dirac model agrees well with the band structure from TB when the antidot is very small, e.g. for the Z{20, 3}GAL geometry. However, large discrepancies are observed for the Z{20, 6}GAL geometry. The band structures agree much better for armchair antidots. For the A{20, 3}GAL geometry, the DE band structure almost coincides with the TB band structure, and the two models are in excellent agreement in this case. Even the band structures for the A{20, 6}GAL with a larger antidot agree very well. This tendency continues for larger antidots, where the band structures from the two models remain very similar.

The lowest bands of the Z{20, 6}GAL geometry are very flat, especially the third conduction band near 0.09 eV, which is almost completely dispersionless. For larger zigzag antidots, even more bands become dispersionless, and the band structures agree even worse. Dispersionless bands are associated with localized states. The localization of the electrons may be visualized by plotting the electron probability density on each atom in the unit cell. Figure 3 shows the probability density of the third conduction band for the Z{20, 6}GAL and A{20, 6}GAL geometries within one unit cell. The plots are

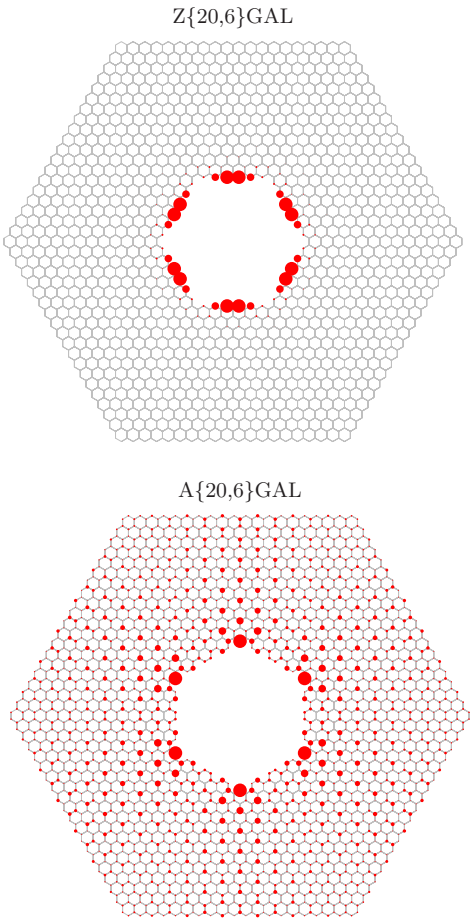

Figure 3. Electron probability density of the third conduction band in one unit cell. The radius of each circle is proportional to the absolute square of the eigenvector element for that atom and chosen such that the radius of the largest circle is the same in both plots.

generated by averaging over the Brillouin zone. It is clear that the electrons of the Z{20, 6}GAL are confined to the edge of the antidot, whereas the electrons in the A{20, 6}GAL are generally spread out over the entire unit cell and only slightly localized in the corners of the antidot. Such localized edge states are generally observed when the antidot contains long zigzag regions. The existence of localized edge states was studied by Fujita *et al* [30], who showed that edge states appear for semi-infinite graphene with zigzag termination, whereas armchair termination does not lead to edge states. Brey and Fertig [31] have used the DE to study the electronic states of GNRs, and by using appropriate boundary conditions, they arrived at the same conclusion. Localized edge states in GALs have previously been studied by Vanević *et al* [32]. They showed that triangular antidots with zigzag edges lead to dispersionless bands where the electrons are localized at the edge of the antidot, which is in good agreement with our results. Recently, Trolle *et al* [19] used DFT and Hubbard TB to investigate localized edge states in GALs with zigzag antidots. Furthermore, they showed that the edge states become spin polarized when $S \geqslant 6$. Edge states have also been observed experimentally using scanning tunnelling spectroscopy on GNRs fabricated by 'unzipping' carbon nanotubes [33]. Edge states modify the electronic properties of GNRs and figure 2 shows that they also modify the electronic properties of GALs. As the size of the antidot increases, edge states appear for zigzag antidots and the electrons become more and more confined to the edges of the antidot. The Dirac model is a continuum model, and consequently all atomistic features are missing. With no boundary conditions, the Dirac model is unable to predict the localized edge states appearing for zigzag edges.

The size of the band gap is highly dependent on the lattice geometry. Generally, the band gap increases as the ratio of antidot to unit-cell area (fill factor) increases. A linear scaling law for GALs with circular antidots was proposed by Pedersen *et al* [16] suggesting that the band gap scales as $E_g \approx K \cdot N_{\text{removed}}^{1/2} / N_{\text{total}}$ for small values of $N_{\text{removed}}^{1/2} / N_{\text{total}}$, where N_{removed} is the number of removed atoms and N_{total} is the total number of atoms in the unit cell before the antidot was created. They determined the scaling constant as $K \simeq 25$ eV, whereas a more exact quasiparticle TB model has revealed a slightly larger constant of $K \simeq 29$ eV [34]. The DE band structures in figure 2 show that the band gap increases as the size of the antidot increases, which is expected from the scaling law. The size of the band gap may be estimated by replacing the hexagonal unit cell with an approximated unit cell with full cylindrical symmetry and by assuming an infinite mass term. This means that both the unit cell and the antidot are replaced by circles of equivalent areas, see appendix A for a derivation. The band gap then only depends on the total area of the unit cell A_{total} and the area of the antidot A_{removed}. The approximation of the band gap (given by equation (A.6)) may be used to calculate the band gap scaled by $A_{\text{total}}^{1/2}$ as a function of $A_{\text{removed}}^{1/2} / A_{\text{total}}^{1/2}$, which becomes the universal curve shown in figure 4. The scaling law predicts a linear correlation on these axes, and a linear approximation of equation (A.6) (given by equation (A.8)) is also shown in the figure. The scaling constant for the DE, obtained from equation (A.8), is $K = 4 \cdot 3^{1/4} \sqrt{\pi} \gamma \simeq 28.3$ eV, which is very close to the scaling constants determined from atomistic models.

Band gap energies of a wide range of structures have been calculated using TB and are compared with the results of the Dirac model in figure 4. The approximation of the band gap using the DE is also included in the figure. The values of A_{total} and A_{removed} in TB are calculated directly from N_{total} and N_{removed}, respectively. The approximated band gap is seen to be a very good estimate as it is very close to the curve obtained from the numerical diagonalization method. Furthermore, the Dirac model predicts that the band gap increases linearly in the regime $A_{\text{removed}}^{1/2} / A_{\text{total}}^{1/2} < 0.4$. For GALs with zigzag antidots, the TB results are close to the results from the Dirac model when the antidots are fairly small. However, edge states appear for larger antidots, which cause the band gap to shrink. Furthermore, the band gaps from TB for zigzag antidots are

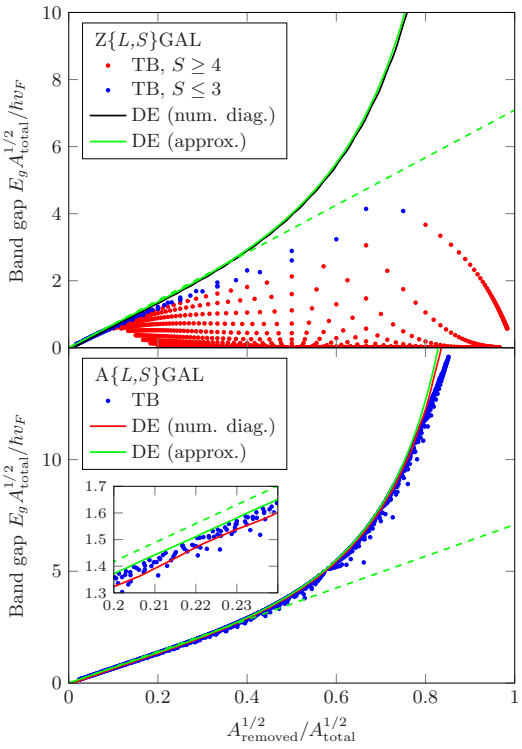

Figure 4. Band gap of GALs with zigzag and armchair antidots calculated using TB and the DE. The green dashed line is a linearization of the approximated Dirac curve. The inset shows a zoom of the linear region.

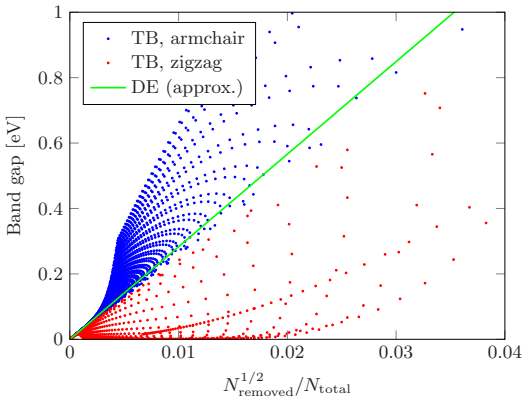

Figure 5. Comparison of the band gap in units of eV for the same data as shown in figure 4.

always lower than the linear Dirac result. For the A{*L*, *S*} GAL structures, the band gaps calculated from TB are all very close to the curves from the DE. Moderate deviations are only observed in the region $A_{\text{removed}}^{1/2}/A_{\text{total}}^{1/2} > 0.8$. The absence of localized edge states in the case of armchair edges means that the band gap does not vanish for large antidots. The inset in the figure shows a zoom, where it is seen that the approximation of the band gap from the DE serves as an upper limit for the TB band gap calculations. The band gap obtained from the numerical diagonalization method shows lower values than the approximated version. This is partly because the numerical diagonalization uses a finite mass term, and partly because the approximated band gap is calculated using an approximate geometry (assumes cylindrical symmetry). Clearly, the results of figure 4 show that the DE is able to accurately predict the band gap of GALs with armchair antidots.

The band gaps in figure 4 are scaled by the area of the unit cell. To provide values of achievable gaps in absolute units, we convert the gaps of armchair and zigzag GALs in figure 4 to eV and compare them in figure 5. It is expected that the band gap of armchair GALs is generally larger than that of zigzag GALs. Figure 5 shows that this is true for all values of $N_{\text{removed}}^{1/2}/N_{\text{total}}$, and it is seen that the approximate band gap from the DE is close to being a separation line between the band gaps of the two types of GALs. At present, state of the art fabrication, using diblock copolymer templates, has resulted in GALs with circular antidots arranged in a triangular pattern with a diameter of 18.7 nm and a period of 36.4 nm [22]. Using these parameters, our Dirac model predicts a band gap of 66 meV, which is close to the measured effective transport gap of 102 meV. This level of discrepancy is reasonable bearing in mind that the transport gap of a disordered structure is expected to deviate somewhat from the band gap of a perfectly periodic model.

The approximation of the band gap using the DE seems to be the better choice, as it is computationally much faster than numerical diagonalization. However, the numerical diagonalization method is necessary in order to calculate band structures and may also be used to calculate other properties such as the density of states and optical conductivity. A comparison of the optical conductivity calculated using the DE and TB is shown in figure 6 for four GALs. The method for calculating the optical conductivity was adopted from [17]. We reach the same conclusion as for the band structures in figure 2. The optical conductivity from the Dirac model agrees very well with the TB results for armchair antidots. For zigzag antidots, the results agree for low energies when the antidot is small, but the optical spectra are very different for larger antidots, e.g. the Z{20, 6}GAL. The optical properties of gapped graphene, i.e. using a spatially invariant mass term, have previously been presented in a closed-form expression and compared with TB [35]. The conductivity spectra $\sigma(\omega)$ were shown to always increase abruptly at the band gap energy to $\sigma(\omega_g) = 2\sigma_0$, where $\sigma_0 = e^2/4\hbar$ is the conductivity of pristine graphene. Gapped graphene was shown to be a good approximation at energies near the band gap for a GAL with a small circular antidot. The spectra from our Dirac model follow the spectra from TB very well in the case of armchair antidots, and even capture features at energies far from the band gap.

Until now, we have only considered GALs with hexagonal antidots, but other geometries may easily be compared with the Dirac model. Figure 7 shows a comparison of the band gap calculated using the DE and TB for GALs with circular

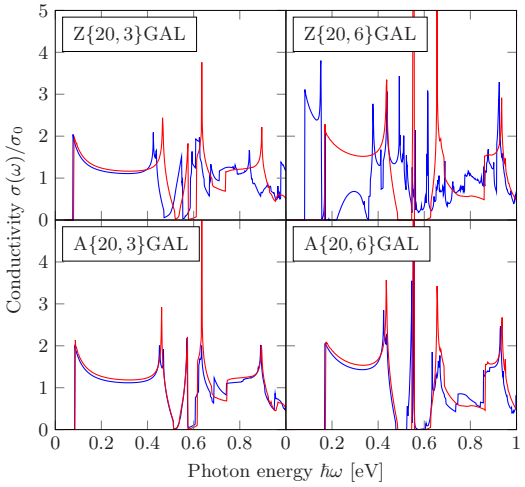

Figure 6. Optical conductivity in units of the pristine graphene conductivity $\sigma_0 = e^2/4\hbar$ calculated using the DE (red) and TB (blue) for the GALs shown in figure 2.

antidots and RGALs with armchair antidots. The edge of circular antidots will consist of both zigzag and armchair edges when the antidot is not very small. The zigzag parts of the edge will support localized edge states when the antidot is large, which cause the band gap to shrink as observed in the figure. However, for small antidots ($R \leqslant 5$), the Dirac model predicts the band gap reasonably well, as the localization is weak.

The band gap calculations of A{*L*, *S*}RGAL structures show the same tendency as the A{*L*, *S*}GAL structures in figure 4. RGALs were found to provide a band gap only for every third value of *L*. This is consistent with previous findings [28], and also obeys a universal band gap opening rule by Dvorak *et al* [36]. The Dirac model predicts that the band gap increases dramatically for $A^{1/2}_{\text{removed}}/A^{1/2}_{\text{total}} > 0.8$. TB shows somewhat lower values of the band gap in this region, but these also increase dramatically as for the Dirac model. Again, the inset shows that the approximation of the band gap from the DE seems to be the upper limit of TB.

It should be noted that while all structures considered in this paper are perfectly ordered, realistic structures from experiments will to some extent contain disorder. Theoretical studies have shown that the band gap of GALs is robust against a considerable amount of disorder [37]. The band gap was found to initially shrink and eventually vanish as the amount of disorder increased. Other calculations have shown that the properties of graphene waveguide structures based on GALs are also robust against structural disorder [38].

We have shown that the Dirac model is in good agreement with TB in the absence of edge states. However, in the case of zigzag or circular antidots, edge states cause the band gap to shrink. If the electrons of edge states are completely confined to the edges of the antidot, they will not be able to contribute to the electronic transport of the GAL. The lowest conduction bands of GALs with large zigzag antidots are almost

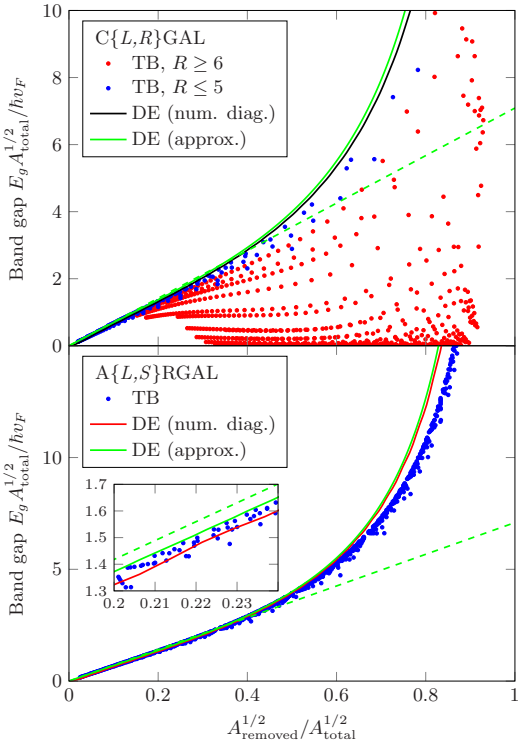

Figure 7. Same as figure 4, but for GALs with circular antidots and RGALs with armchair antidots.

completely dispersionless, which suggests that the transport gap in such cases may be larger than the band gap.

4. Conclusion

We have presented a continuum model based on the Dirac equation, which describes the electronic and optical properties of graphene antidot lattices. The major advantages of the Dirac model are that the computational time does not depend on the size or geometry of the structures, and that the results are scalable. The Dirac model is compared with tight-binding calculations of the corresponding atomistic structures in order to determine its accuracy. A comparison of band structures shows that the Dirac model is in quantitative agreement with tight-binding for structures with no edge states, e.g. antidots with armchair edges. The present Dirac model is unable to predict edge states as it does not distinguish between zigzag and armchair edges. Comparing band gap calculations and optical spectra also shows quantitative agreement between the models for structures with no edge states.

An approximation of the band gap of a graphene antidot lattice was derived from the Dirac equation. A linearization revealed a scaling constant in good agreement with previously suggested values obtained from atomistic models. The approximation provides a very fast way of estimating the band

gap of a graphene antidot lattice with no edge states even if the antidot makes up a large part of the unit cell.

Acknowledgments

The authors gratefully acknowledge the financial support from the Center for Nanostructured Graphene (project no. DNRF58) financed by the Danish National Research Foundation. We thank A-P Jauho for useful comments on the manuscript.

Appendix A. Estimate of band gap

In this appendix, we present an approximation of the band gap of GALs derived using the DE. The hexagonal unit cell is replaced by one with full cylindrical symmetry, i.e. a circle of radius R_e, see figure A1. This approach is inspired by [39]. The area of the circle is equal to the area of the hexagonal unit cell, such that $A_{\text{total}} = \pi R_e^2$. If the antidot is not circular, this is also replaced by a circle with radius R of equivalent antidot area, $A_{\text{removed}} = \pi R^2$.

The Dirac Hamiltonian in cylindrical coordinates is

$$\mathbf{H} = \hbar v_{\text{F}} \begin{pmatrix} \widetilde{\Delta}(r) & -\mathrm{i}\mathrm{e}^{-\mathrm{i}\theta}\left(\partial_r - \frac{\mathrm{i}}{r}\partial_\theta\right) \\ -\mathrm{i}\mathrm{e}^{\mathrm{i}\theta}\left(\partial_r + \frac{\mathrm{i}}{r}\partial_\theta\right) & -\widetilde{\Delta}(r) \end{pmatrix}, \quad \text{(A.1)}$$

where $\widetilde{\Delta}(r) = \frac{\Delta_0}{\hbar v_{\text{F}}} H(R-r) = \widetilde{\Delta}_0 H(R-r)$ and H is the Heaviside step function. The wave function is of the form

$$\Psi(r,\theta) = \frac{1}{\sqrt{2}} \begin{pmatrix} \mathrm{i}^m f(r)\,\mathrm{e}^{\mathrm{i}m\theta} \\ \mathrm{i}^{m+1} g(r)\,\mathrm{e}^{\mathrm{i}(m+1)\theta} \end{pmatrix}, \quad \text{(A.2)}$$

which is inserted in the DE together with the Hamiltonian. For a piecewise constant mass term, the solutions for f and g are

$$f(r) = \begin{cases} J_m(kr) + B_m Y_m(kr) & r > R \\ C_m I_m(qr) & r < R \end{cases}, \quad \text{(A.3)}$$

$$g(r) = \begin{cases} J_{m+1}(kr) + B_m Y_{m+1}(kr) & r > R \\ -C_m \sqrt{\dfrac{\widetilde{\Delta}_0 - k}{\widetilde{\Delta}_0 + k}}\, I_{m+1}(qr) & r < R \end{cases}, \quad \text{(A.4)}$$

where J_m and Y_m are the m'th order Bessel functions of the first and second kind, respectively, I_m is the m'th order modified Bessel function of the first kind, $k = E/\hbar\, v_{\text{F}}$ and $q = (\widetilde{\Delta}_0^2 - k^2)^{1/2}$. Both f and g must be continuous at $r = R$, which is used to determine B_m and C_m. For the lowest state ($m = 0$) and in the limit of large $\widetilde{\Delta}_0$, the coefficients become

$$B_0 \approx -\frac{J_0(kR) + J_1(kR)}{Y_0(kR) + Y_1(kR)}, \qquad C_0 \approx 0. \quad \text{(A.5)}$$

This derivation is generally carried out using a finite mass term, and the band gap may also be calculated in this case. The wave functions inside and outside the antidot are matched at the edge of the antidot in the case of a finite mass term, which is used to determine B_m and C_m. Subsequently the limit of a large mass term is applied for which the coefficients listed above are valid. This approach does not lead to boundary conditions that cause problems in the limit of small antidots as observed in [18].

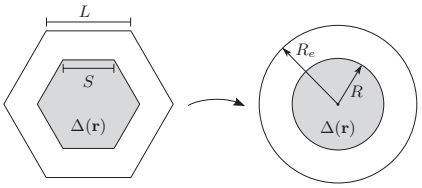

Figure A1. The hexagonal unit cell and the antidot are replaced by circles of equivalent areas. This approximated geometry has cylindrical symmetry.

We restrict our analysis to the Γ-point of the Brillouin zone, as this is where the band gap opens. We still require that the wave function is Bloch-periodic when using the approximated geometry. However, at the Γ-point it is merely periodic. Periodicity implies a vanishing derivative of f at the outer boundary ($r = R_e$), meaning that $J_1(kR_e) + B_0 Y_1(kR_e) = 0$. This yields the equation

$$J_1(kR_e)\,[\,Y_0(kR) + Y_1(kR)\,] - Y_1(kR_e)\,[\,J_0(kR) + J_1(kR)\,] = 0, \quad \text{(A.6)}$$

which may be solved numerically for k to obtain the band gap given by $E_g = 2\hbar v_{\text{F}} k$. f is used to solve for the lowest energy of the conduction bands. Equivalently, g may be solved for negative energies using $m = -1$ which leads to the highest energy of the valence bands. The Bessel functions in equation (A.6) are approximated by assuming small k, such that the equation becomes

$$\frac{4}{kR_e} + kR_e - \frac{2R_e}{R} + \frac{2R}{R_e} + kR_e(2 + kR)\ln\left(\frac{R}{R_e}\right) = 0. \quad \text{(A.7)}$$

In the limit of small R, the solution becomes the simple expression $k \approx 2R/R_e^2$, meaning that

$$E_g = 4\hbar v_{\text{F}} \frac{R}{R_e^2} = 4\sqrt{\pi}\,\hbar v_{\text{F}} \frac{A_{\text{removed}}^{1/2}}{A_{\text{total}}}. \quad \text{(A.8)}$$

This shows that at small k, the band gap is directly proportional to the square root of the removed area and inversely proportional to the area of the unit cell, which is consistent with previously suggested scaling laws [16, 34].

References

[1] Novoselov K S, Geim A K, Morozov S V, Jiang D, Zhang Y, Dubonos S V, Grigorieva I V and Firsov A A 2004 *Science* **306** 666

[2] Novoselov K S, Jiang D, Schedin F, Booth T J, Khotkevich V V, Morozov S V and Geim A K 2005 *Proc. Natl Acad. Sci. USA* **102** 10451

[3] Bolotin K I, Sikes K, Jiang Z, Klima M, Fudenberg G, Hone J, Kim P and Stormer H 2008 *Solid State Commun.* **146** 351

[4] Nair R R, Blake P, Grigorenko A N, Novoselov K S, Booth T J, Stauber T, Peres N M R and Geim A K 2008 *Science* **320** 1308
[5] Lee C, Wei X, Kysar J W and Hone J 2008 *Science* **321** 385
[6] Geim A K 2009 *Science* **324** 1530
[7] Obradovic B, Kotlyar R, Heinz F, Matagne P, Rakshit T, Giles M, Stettler M and Nikonov D 2006 *Appl. Phys. Lett.* **88** 142102
[8] Son Y W, Cohen M L and Louie S G 2006 *Phys. Rev. Lett.* **97** 216803
[9] Han M Y, Özyilmaz B, Zhang Y and Kim P 2007 *Phys. Rev. Lett.* **98** 206805
[10] Zhang Y, Tang T T, Girit C, Hao Z, Martin M C, Zettl A, Crommie M F, Shen Y R and Wang F 2009 *Nature* **459** 820
[11] Pedersen J G and Pedersen T G 2012 *Phys. Rev.* B **85** 235432
[12] Recher P and Trauzettel B 2010 *Nanotechnology* **21** 302001
[13] Molitor F, Güttinger J, Stampfer C, Dröscher S, Jacobsen A, Ihn T and Ensslin K 2011 *J. Phys.: Condens. Matter* **23** 243201
[14] Güttinger J, Molitor F, Stampfer C, Schnez S, Jacobsen A, Dröscher S, Ihn T and Ensslin K 2012 *Rep. Prog. Phys.* **75** 126502
[15] Kandemir B S and Omer G 2013 *Eur. Phys. J.* B **86** 299
[16] Pedersen T G, Flindt C, Pedersen J G, Mortensen N A, Jauho A P and Pedersen K 2008 *Phys. Rev. Lett.* **100** 136804
[17] Pedersen T G, Flindt C, Pedersen J, Jauho A P, Mortensen N A and Pedersen K 2008 *Phys. Rev.* B **77** 245431
[18] Fürst J A, Pedersen J G, Flindt C, Mortensen N A, Brandbyge M, Pedersen T G and Jauho A P 2009 *New J. Phys.* **11** 095020
[19] Trolle M L, Møller U S and Pedersen T G 2013 *Phys. Rev.* B **88** 195418
[20] Eroms J and Weiss D 2009 *New J. Phys.* **11** 095021
[21] Giesbers A J M, Peters E C, Burghard M and Kern K 2012 *Phys. Rev.* B **86** 045445
[22] Kim M, Safron N S, Han E, Arnold M S and Gopalan P 2010 *Nano Lett.* **10** 1125
[23] Kim M, Safron N S, Han E, Arnold M S and Gopalan P 2012 *ACS Nano* **6** 9846
[24] Oberhuber F, Blien S, Heydrich S, Yaghobian F, Korn T, Schüller C, Strunk C, Weiss D and Eroms J 2013 *Appl. Phys. Lett.* **103** 3111
[25] Xu Q, Wu M Y, Schneider G F, Houben L, Malladi S K, Dekker C, Yucelen E, Dunin-Borkowski R E and Zandbergen H W 2013 *ACS Nano* **7** 1566
[26] Jia X *et al* 2009 *Science* **323** 1701
[27] Seitsonen A P, Saitta A M, Wassmann T, Lazzeri M and Mauri F 2010 *Phys. Rev.* B **82** 115425
[28] Petersen R, Pedersen T G and Jauho A P 2010 *ACS Nano* **5** 523
[29] Lee S W and Mittra R 1983 *IEEE Trans. Antennas Propag.* **31** 99
[30] Fujita M, Wakabayashi K, Nakada K and Kusakabe K 1996 *J. Phys. Soc. Japan* **65** 1920
[31] Brey L and Fertig H 2006 *Phys. Rev.* B **73** 235411
[32] Vanević M, Stojanović V M and Kindermann M 2009 *Phys. Rev.* B **80** 045410
[33] Tao C *et al* 2011 *Nat. Phys.* **7** 616
[34] Petersen R and Pedersen T G 2009 *Phys. Rev.* B **80** 113404
[35] Pedersen T G, Jauho A P and Pedersen K 2009 *Phys. Rev.* B **79** 113406
[36] Dvorak M, Oswald W and Wu Z 2013 *Sci. Rep.* **3** 02289
[37] Yuan S, Roldán R, Jauho A P and Katsnelson M I 2013 *Phys. Rev.* B **87** 085430
[38] Pedersen J G, Gunst T, Markussen T and Pedersen T G 2012 *Phys. Rev.* B **86** 245410
[39] Mortensen N A 2006 *J. Eur. Opt. Soc.—Rapid* **1** 06009

Publication II

Dirac model of electronic transport in graphene antidot barriers

Morten Rishøj Thomsen, Søren Jacob Brun and Thomas Garm Pedersen

The paper has been published in
Journal of Physics: Condensed matter **26**, 335301 (2014).

IOP Publishing Journal of Physics: Condensed Matter
J. Phys.: Condens. Matter **26** (2014) 335301 (8pp) doi:10.1088/0953-8984/26/33/335301

Dirac model of electronic transport in graphene antidot barriers

M R Thomsen, S J Brun and T G Pedersen

Department of Physics and Nanotechnology, Aalborg University, Skjernvej 4A, DK-9220 Aalborg Øst, Denmark
Center for Nanostructured Graphene (CNG), DK-9220 Aalborg Øst, Denmark

E-mail: mrt@nano.aau.dk

Received 30 April 2014, revised 26 June 2014
Accepted for publication 30 June 2014
Published 29 July 2014

Abstract

In order to use graphene for semiconductor applications, such as transistors with high on/off ratios, a band gap must be introduced into this otherwise semimetallic material. A promising method of achieving a band gap is by introducing nanoscale perforations (antidots) in a periodic pattern, known as a graphene antidot lattice (GAL). A graphene antidot barrier (GAB) can be made by introducing a 1D GAL strip in an otherwise pristine sheet of graphene. In this paper, we will use the Dirac equation (DE) with a spatially varying mass term to calculate the electronic transport through such structures. Our approach is much more general than previous attempts to use the Dirac equation to calculate scattering of Dirac electrons on antidots. The advantage of using the DE is that the computational time is scale invariant and our method may therefore be used to calculate properties of arbitrarily large structures. We show that the results of our Dirac model are in quantitative agreement with tight-binding for hexagonal antidots with armchair edges. Furthermore, for a wide range of structures, we verify that a relatively narrow GAB, with only a few antidots in the unit cell, is sufficient to give rise to a transport gap.

Keywords: graphene, antidot, dirac equation, electronic transport

(Some figures may appear in colour only in the online journal)

1. Introduction

Graphene has been the subject of intense research since its discovery in 2004 [1]. Especially the ultrahigh mobility [2–4] of pristine graphene makes it a promising platform for novel nanoelectronic devices. Pristine graphene does not have a band gap, which makes it ill-suited for semiconductor applications, such as transistors with high on/off ratios for logic applications. Band gaps in graphene have been demonstrated experimentally in graphene nanoribbons [5], gated bilayer graphene [6, 7] and patterned adsorption of hydrogen on graphene [8]. Another promising method for creating a tunable band gap in graphene is by introducing nanoscale perforations in a periodic fashion, known as graphene antidot lattices (GALs) or graphene nanomeshes [9–11]. The magnitude of the band gap depends on the size of the antidots, size of the unit cell and on edge chirality [9, 12–15]. It has been shown that the band gap of GALs with relatively small antidots follows a simple scaling rule proposed by Pedersen *et al* [9].

Several methods have been used to produce GALs experimentally, including e-beam lithography [16–18], diblock copolymer templates [19–21], anodic aluminum oxide templates [22], nanosphere lithography [23] and nanoimprint lithography [24]. The antidots range in size between a few nanometers and several hundred nanometers, depending on the fabrication method. The antidots synthesized with these methods are often round, but it has been demonstrated experimentally that armchair and zigzag edges in GALs are stable and can be synthesized selectively [25–27]. Recent experimental studies of transport in GALs have shown on/off ratios in the range between 4 and 100 [19, 22, 24]. These values are still too low for logic applications [28], but the results are important indicators that devices based on GALs could be used to make efficient transistors. The electronic transport properties of GALs have also been studied theoretically. The transport through graphene antidot barriers (GABs), i.e. 1D periodic antidot structures in an otherwise pristine sheet of graphene, has previously been studied for small systems using

a tight-binding (TB) formalism [29, 30]. These studies showed that just a few antidots in the unit cell of the GAB is sufficient to suppress the transport within the band gap region. Suppression of transport in antidot regions has also been used to model electronic waveguides [31], where a transport channel is kept pristine, while the rest of the structure is a GAL. Their results show that GAL waveguides have higher conductance than corresponding graphene nanoribbons. Furthermore, Berreda *et al* [32] have simulated three different graphene field-effect transistors based on GALs with band gaps of about 500 meV. They showed that their simulated devices had on/off ratios as high as 7400, which is close to that of silicon based MOSFETs that have on/off ratios on the order of 10^4 to 10^7 [28].

Experimentally feasible GALs are typically too large to handle with traditional atomistic models, such as TB and DFT. However, models based on the Dirac equation (DE) are in the continuum regime and are therefore able to handle arbitrarily large structures. In this paper, we will use the Dirac equation (DE) with a spatially varying mass term to calculate the scattering of Dirac electrons in GABs that are periodic in one dimension. It has previously been shown that the DE on this form can be used to calculate the band structure of GALs [11, 12]. In addition, the DE has previously been used to calculate scattering of Dirac electrons on a single circular mass barrier [33], a single circular electrostatic barrier [34] and simple barriers of constant and finite mass [35]. The advantages of our approach are that it works for any antidot shape and for an arbitrary arrangement of antidots. Furthermore, our method can easily be extended to a 1D periodic case. Another advantage that arises from using the DE is that all results are scalable, i.e., the results are invariant when all lengths are scaled up by some factor and all energies are scaled down by the same factor. We use a Green's tensor area integral equation method (AIEM) in order to solve the DE. We will focus on the transport of a plane electron wave through GABs with two different types of hexagonal antidots, namely antidots with zigzag edges and antidots with armchair edges. We compare the results of our Dirac model with results obtained with TB.

2. Theory and methods

In this section, we will set up a Green's tensor AIEM to calculate the scattering of Dirac electrons on arbitrary graphene antidot structures, where an electron wave is incident on the structure and the resulting total wave function is calculated. Once this general method has been set up, we will specialize to scattering of Dirac electrons on GABs as shown in figure 1(*b*). The idea of using an AIEM to solve inhomogeneous differential equations is not new. In fact, it has been used extensively to solve scattering problems in optics [36, 37] and we utilize several of the same techniques to calculate scattering of electron waves in graphene.

The DE for a graphene sheet with a spatially varying mass term $\Delta(\vec{r})$ has the form [11]

$$(v_F\boldsymbol{\sigma}\cdot\vec{p}+\Delta(\vec{r})\sigma_z-\boldsymbol{I}E)\Psi=0, \tag{1}$$

$$(v_F\boldsymbol{\sigma}\cdot\vec{p}-\Delta(\vec{r})\sigma_z-\boldsymbol{I}E)\Psi'=0, \tag{2}$$

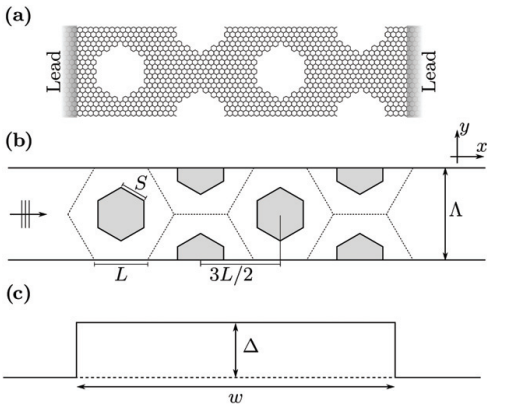

Figure 1. Unit cells of a GAB with four rows of armchair antidots. (*a*) Geometry used in TB. (*b*) Geometry used with the DE, where the mass term has a constant value of Δ_0 inside the shaded areas and is vanishing elsewhere. (*c*) Dirac mass barrier (DMB) with height Δ and width w.

where $\Psi=\{\psi_A,\psi_B\}$ and $\Psi'=\{\psi'_B,\psi'_A\}$ are the wave functions associated with the K and K' valleys, respectively, $\boldsymbol{\sigma}=\{\sigma_x,\sigma_y\}$ and σ_z are the Pauli matrices, $\boldsymbol{p}=\{\hat{p}_x,\hat{p}_y\}$ is the momentum operator, and v_F is the Fermi velocity. The mass term has a constant value of Δ_0 inside the antidots and is vanishing elsewhere. This effectively makes electrons massive inside the antidots, making it energetically unfavorable to enter them. The mass term should be sufficiently large in order to model actual holes in graphene. It should generally be much larger than the electron energy $\Delta_0\gg|E|$. We use $\Delta_0=170\,\mathrm{eV}/L$ in all our calculations, which is identical to the value used in [12]. Due to the similarity of the K and K' equations, we can restrict our analysis to one of them. The wave function of the incident wave Ψ_0 must be a solution to the case without a scatterer (pristine graphene), i.e. the case where $\Delta(\vec{r})=0$ everywhere. This simply reduces equation (1) to the DE without a mass term. We will use incident plane waves on the form $\Psi_0=2^{-1/2}(1,\mathrm{e}^{\mathrm{i}\varphi})^T\mathrm{e}^{\mathrm{i}\vec{k}\cdot\vec{r}}$, where φ is the polar angle of $\vec{k}$.

The Green's tensor $\boldsymbol{G}$ between an observation point $\vec{r}$ and a source point $\vec{r}'$ is defined as the solution to the equation

$$(v_F\boldsymbol{\sigma}\cdot\vec{p}-\boldsymbol{I}E)\boldsymbol{G}(\vec{r},\vec{r}')=-\boldsymbol{I}\delta(\vec{r}-\vec{r}'). \tag{3}$$

The solution must obey the radiation condition, which states that the solution should asymptotically tend towards an outward propagating wave proportional to $\mathrm{e}^{\mathrm{i}kr}/\sqrt{kr}$. This uniquely specifies the Green's tensor as

$$\boldsymbol{G}(\vec{r},\vec{r}')=\frac{k}{4\mathrm{i}}\begin{pmatrix}H_0^{(1)}(kr) & -\mathrm{i}\mathrm{e}^{-\mathrm{i}\theta}H_1^{(1)}(kr)\\ -\mathrm{i}\mathrm{e}^{\mathrm{i}\theta}H_1^{(1)}(kr) & H_0^{(1)}(kr)\end{pmatrix}, \tag{4}$$

where $H_n^{(1)}$ is the n'th order Hankel function of the first kind, $k=E/\hbar v_F$, $r=|\vec{r}-\vec{r}'|$ and θ is the polar angle of $\vec{r}-\vec{r}'$. By subtracting the DE without a mass term from equation (1) we get

$$(v_F\boldsymbol{\sigma}\cdot\vec{p}-\boldsymbol{I}E)(\Psi-\Psi_0)=-\Delta(\vec{r})\sigma_z\Psi, \tag{5}$$

which has the solution

$$\Psi(\vec{r}) = \Psi_0(\vec{r}) + \int \widetilde{\Delta}(\vec{r}')\sigma_z \boldsymbol{G}(\vec{r},\vec{r}')\Psi(\vec{r}')d^2r', \qquad (6)$$

where $\widetilde{\Delta}(\vec{r}) = \Delta(\vec{r})/\hbar v_F$. This is the central equation for the Green's tensor AIEM, which we will use to calculate the scattering of Dirac electrons on antidot structures. It can be demonstrated that the equation is invariant when all lengths are scaled up by some factor and all energies and mass terms are scaled down by the same factor. This effectively means that the computational time is scale invariant.

The main advantage of this approach is that we only need to consider points $\vec{r}'$ where $\Delta(\vec{r}') \neq 0$, i.e. inside the antidot. Once we know the wave function inside the antidot, it is a simple matter to use equation (6) to calculate the wave function at any other position. We solve this self-consistently by discretizing the area inside the antidots into a number of small areas δA_i with centers $\vec{r}_i$. The integral is then completed by assuming that the mass term and the wave function are constant inside each area element and by approximating the Green's tensor between element i and j as

$$\boldsymbol{G}_{ij} \simeq \begin{cases} (\delta A_j)^{-1}\int_{\delta A_j} \boldsymbol{G}(\vec{r}_i,\vec{r}')d^2r' & \text{if } i = j \\ \boldsymbol{G}(\vec{r}_i,\vec{r}_j) & \text{if } i \neq j. \end{cases} \qquad (7)$$

The self-interaction element $i = j$ may be calculated by approximating the area element with a circle, with radius r_{eq}, of equivalent area, i.e. $\delta A_j = \pi r_{\mathrm{eq}}^2$, and integrating in polar coordinates

$$\boldsymbol{G}_{ii} \simeq [1/(\pi r_{\mathrm{eq}}^2 k) - i H_1^{(1)}(kr_{\mathrm{eq}})/(2r_{\mathrm{eq}})]\boldsymbol{I}. \qquad (8)$$

We now have all the ingredients necessary to solve the scattering problem. It is then a simple matter of using matrix inversion or some efficient iterative scheme to solve for the wave function inside the antidots.

We will specialize to the case of GABs, where the antidot structure is periodic along the y-direction with period Λ as shown in figure 1(b). We will focus on hexagonal antidots arranged in a GAL configuration, meaning that the antidot lattice vectors are parallel to the carbon-carbon bonds of the graphene lattice as shown in figure 1(a). The antidots are chosen, such that they have either armchair edges (denoted armchair antidots) or zigzag edges (denoted zigzag antidots). The structures are described by the side length L of the GAL unit cell, the side length S of the antidot and the number of antidots N in the GAB unit cell, see figure 1(b). All distances are in units of the graphene lattice constant a. The notation N−A$\{L, S\}$GAL and N−Z$\{L, S\}$GAL will be used to describe barriers with N armchair and zigzag antidots, respectively, in GAL a configuration.

In the periodic case, the scattered part of the wave function is given by an infinite sum of integrals over unit cells. By shifting all integrals to the zeroth unit cell, we can take the sum inside the integral and, thus, only integrate over the area of the zeroth unit cell A_0. All shifted wave functions are related to the wave function in the zeroth unit cell by the Bloch condition $\Psi(\vec{r} + m\Lambda\hat{y}) = \Psi(\vec{r})\mathrm{e}^{\mathrm{i}mk_y\Lambda}$, where m is an integer, $\Lambda = \sqrt{3}L$ is the period, $k_y = k\sin(\varphi)$ and φ is the angle of incidence. We may then write the wave function as

$$\Psi(\vec{r}) = \Psi_0(\vec{r}) + \int_{A_0} \widetilde{\Delta}(\vec{r}')\sigma_z \widetilde{\boldsymbol{G}}(\vec{r},\vec{r}')\Psi(\vec{r}')d^2r', \qquad (9)$$

where $\widetilde{\boldsymbol{G}}$ is a modified Green's tensor given by

$$\widetilde{\boldsymbol{G}}(\vec{r},\vec{r}') = \sum_{m=-\infty}^{\infty} \boldsymbol{G}(\vec{r},\vec{r}' - m\Lambda\hat{y})e^{\mathrm{i}k_y m\Lambda}. \qquad (10)$$

This sum is extremely slowly convergent. However, once it has been determined, the problem of finding the wave function is no harder than in the non-periodic case. Using Graf's theorem [38] the Green's tensor may be restated as

$$\widetilde{\boldsymbol{G}}(\vec{r},\vec{r}') = \sum_{m=-M}^{M} \boldsymbol{G}(\vec{r},\vec{r}' - m\Lambda\hat{y}) + \frac{k}{4\mathrm{i}}\sum_{n=-\infty}^{\infty} \mathrm{i}^n J_n(kr)e^{-in\theta}\begin{pmatrix} S_n & -S_{n-1} \\ -S_{n+1} & S_n \end{pmatrix}, \qquad (11)$$

where J_n is the n'th order Bessel function of the first kind and S_n is the n'th order *lattice sum* given by

$$S_n = \sum_{m=M+1}^{\infty} H_n^{(1)}(km\Lambda)\left(\mathrm{e}^{\mathrm{i}k_y m\Lambda} + (-1)^n \mathrm{e}^{-\mathrm{i}k_y m\Lambda}\right). \qquad (12)$$

We have taken the contribution of M unit cells on either side of the zeroth unit cell outside the lattice sum as they may not satisfy the condition for using Graf's theorem. In fact, Graf's theorem is only satisfied when the largest distance between area elements within one unit cell is smaller than $(M + 1)\Lambda$. Therefore, M is chosen to be the smallest integer that satisfies this condition. The lattice sum is actually also extremely slowly convergent, but there are two advantages of writing $\widetilde{\boldsymbol{G}}$ using the lattice sum: 1) The lattice sum does not depend on the observation point, so it needs only be calculated once for a given choice of $k\Lambda$ and angle of incidence φ, and 2) it can be calculated efficiently using the integral representation described in [39].

The transmittance $T(E)$ of an electron with energy E through the barrier is simply the transmitted current $I(E)$ at that energy divided by the incident current I_0. The current is calculated by integrating the x-component of the current density over one period $I = \int_{uc} j_x\, dy$, where the current density is given by $j_x = \Psi^\dagger \hat{j}_x \Psi$ using the current density operator $\hat{j}_x = -ev_F\sigma_x$. The experimentally relevant quantity is the total current I expressed as a function of bias voltage V_B given by [40]

$$I(V_B) = \frac{2e}{h}\int_{-\infty}^{\infty} T(E)[f(E, E_F + eV_B) - f(E, E_F)]\,\mathrm{d}E, \qquad (13)$$

where $f(E, E_F) = (1 + \exp[(E - E_F)/kT])^{-1}$ is the Fermi-Dirac distribution. The only unknown quantity in this expression is the transmittance function $T(E)$. The transmittance function has more distinct features than the current and we therefore show this quantity instead

of the current in most cases. In the limit of vanishing bias, the conductance is $G = G_0 T$, where $G_0 = 2e^2/h$ is the conductance quantum.

In order to assess the accuracy of our model, we compare our results with spectra calculated using the Landauer approach with a nearest-neighbor TB Hamiltonian, as outlined in [29]. We use a hopping integral of $\gamma = 3.033$ eV and, for numerical stability, we add a small imaginary part to the energy, such that $E \to E + i\varepsilon$, where we use $\varepsilon = 10^{-5}$ eV. In the Dirac models, we average over valleys in order to obtain the transmittance per valley. All TB spectra are therefore divided by a factor of two in order to directly compare with the DE.

In order to make a quantitative comparison between the models for a wide range of structures, we define a transport gap using the lowest positive energy, at which the transmittance rises above 1/2. Due to exact electron-hole symmetry, the transport gap will then be twice this energy. Long zigzag edges give rise to very localized states in TB. However, in a real device with even a small amount of disorder, we do not expect these states to support electronic transport. This effect can be introduced heuristically by convolving the TB transmittance spectra with a Gaussian or by using a larger imaginary part of the energy $i\varepsilon$. Therefore, in our calculations of the transport gap we convolve with a Gaussian having a full width at half maximum of $0.1\,\text{eV}/L$.

The transport gap of a GAB may be approximated by replacing the actual structure with a simple barrier as shown in figure 1(*c*). This type of barrier is referred to as a Dirac mass barrier (DMB) and was shown by Pedersen *et al* to be in good agreement with tight-binding in the gap region [29]. In this approach, we define the width of the barrier as $w = N(3L/2)$ and take the barrier height Δ to be half the band gap of the fully periodic case. We use the approximation of the band gap given by equation A6 in [12]. This approach thus offers a quick way to estimate the transport gap.

3. Results and discussion

In this section, we present the results of our Dirac model and compare them with TB. Furthermore, we compare transport gap spectra with the DMB model. Results are presented for both armchair and zigzag antidots. The geometries used in our Dirac model are created such that the total area of the antidots equals the total area of the removed atoms of the corresponding structure used in TB.

3.1. Armchair antidots

We start out by considering GABs in GAL configuration containing armchair antidots. The transmittance spectra of two different barriers with armchair antidots is shown in figure 2. The results are only displayed for positive energies, as the results for negative energies follow from exact electron-hole symmetry in the models. There is excellent agreement between TB and our Dirac model. Furthermore, it is seen that there are always $N - 1$ subpeaks in the transmittance peak, which is consistent with previous calculations for graphene nanoribbons with antidot arrays [41]. This means that as the number of

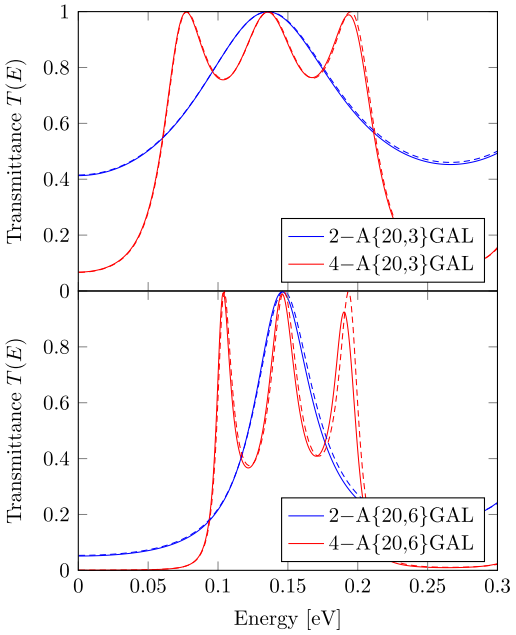

Figure 2. Transmittance of GABs with armchair antidots calculated with TB (solid) and the DE (dashed).

antidots in the unit cell increases, the subpeaks will come closer to each other and eventually merge into a single step-like plateau.

In order to gain insight into the electronic transport through a GAB, we compute the electron probability density for a 4−A{20, 6}GAL barrier at two different electron energies, as shown in figure 3. The two lowest bands in the electronic band structure for the fully periodic structure have energies in the intervals [0.09; 0.24] eV and [0.31; 0.50] eV as given in [12]. We expect low transmittance in the band gap regions of the fully periodic structure and high transmittance elsewhere. At $E = 0.15$ eV, the electron has an energy within the first band, and the probability density inside the barrier is therefore quite high, which results in a very high transmittance of $T \simeq 0.91$. However, at $E = 0.3$ eV, the electron has an energy within a band gap, and the probability density inside the barrier is therefore rather low, which results in a much lower transmittance of $T \simeq 0.02$. This means that the transmittance is low for energies at which the barrier region does not support any electron states.

Armchair antidots do not support localized edge states, which means that, in the limit of very wide barriers, the transport gap should equal the band gap of the fully periodic structure. It is interesting, however, to see if a barrier with only a few antidots in the unit cell is able to block electron transport in the band gap region. Figure 4 shows the transport gap of a large range of GABs with just 4 antidots in the unit cell. In accordance with [12], the results are scaled with the total area of the GAL unit cell $A_{\text{tot}} = 3\sqrt{3}L^2/2$ and the area of a single antidot A_{rem}. It is seen that the transport

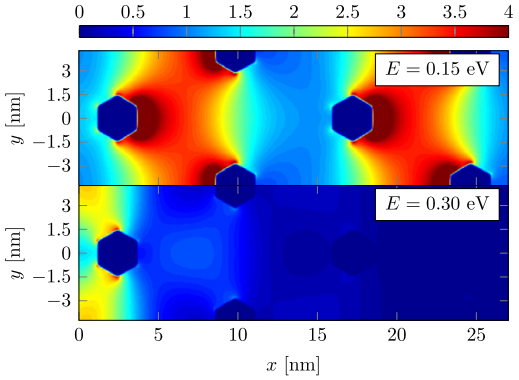

Figure 3. Probability density of electrons in a 4−A{20,6}GAL barrier calculated using the DE. The probability density is measured relative to the incident wave.

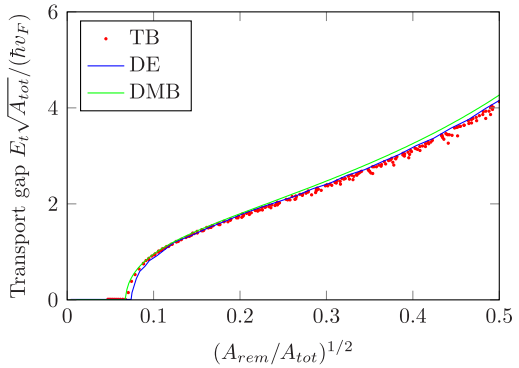

Figure 4. Transport gap of 4−A{L, S}GAL barriers calculated using TB, the DE and the DMB model.

gap opens up for antidots with a size $(A_{\text{rem}}/A_{\text{tot}})^{1/2} > 0.07$. The transport gap is exactly zero for small antidots, as the transmittance is higher than $1/2$ at vanishing energy. The abrupt opening of the transport gap is due to the horizontal slope of the transmittance as a function of energy at small energies. This means that as soon as the structure is large enough for the transmittance at vanishing energy to fall below $1/2$, the transport gap will increase rapidly. The exact location of the onset of the transport gap is, thus, sensitive to the choice of transport gap definition. However, the remaining values are not too sensitive to the exact definition of the transport gap, since the slope of the transmittance spectrum is typically very large near the transport gap. It is seen that both Dirac models are in excellent agreement with TB.

3.2. Zigzag antidots

Transmittance spectra calculated with our Dirac model for two different barriers with zigzag antidots are shown in figure 5 and compared to TB. There is a fairly good agreement between the models for the smaller antidots, but the agreement is very poor for the larger structure. These deviations arise due to the

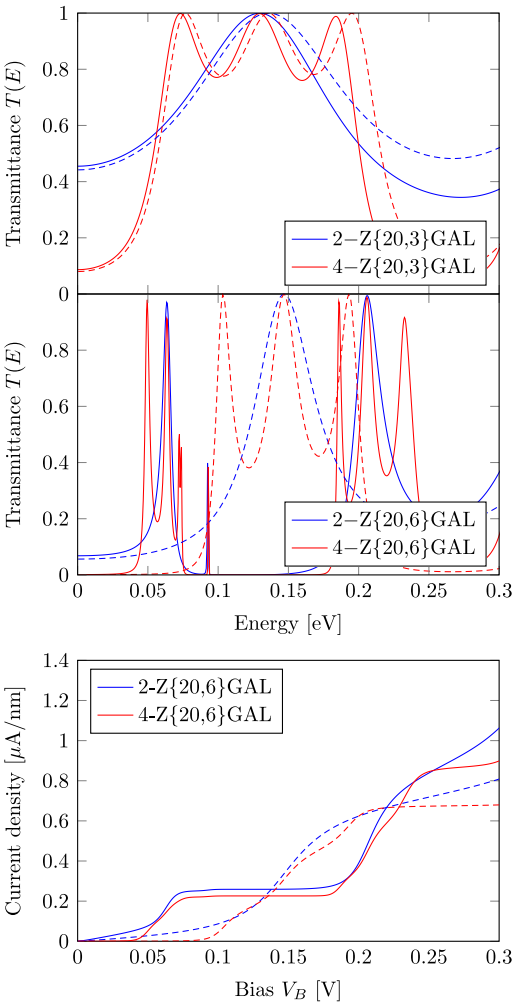

Figure 5. Transmittance (top) and current density (bottom) of GABs with zigzag antidots calculated using TB (solid) and the DE (dashed).

highly localized state in the TB spectrum near 0.09 eV, which is a result of the long zigzag edges. The deviations between TB and the DE have also been observed in the calculation of the band gap of fully periodic GALs [12]. The current density as a function of bias voltage can be calculated from equation (13) by dividing the current with the period of the unit cell. It follows from the equation that the current densities will be similar for similar transmittance functions. This is the case for GABs with armchair antidots. However, for structures like the 4-Z{20,6}GAL, where there is poor agreement of the transmittance function between TB and DE, the current densities will also be in poor agreement. This is illustrated in figure 5, where the current density has been calculated assuming a temperature of 30 K.

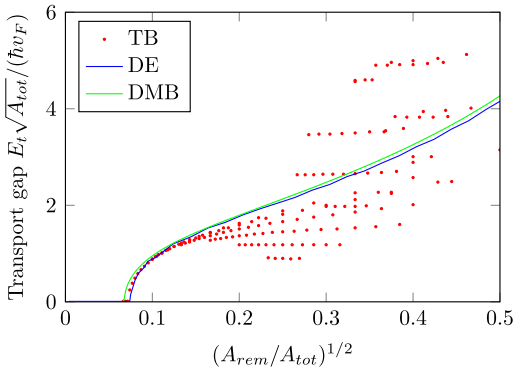

Figure 6. Transport gap of 4−Z{L, S}GAL barriers calculated using TB, the DE, and the DMB model.

It has previously been shown that the band gap shrinks substantially, compared to simple scaling laws, for structures with large zigzag antidots due to the presence of edge states [12]. The shrinking of the band gap is only predicted by the TB model, as the DE with a mass term does not distinguish between zigzag and armchair edges. In the calculation of the transport gap, we overcome some of the effects of very localized edge states in our TB calculations by convolving all TB transmittance spectra with a Gaussian. This smears out very narrow features of the transmittance spectra, while preserving those that are not. We compare the transport gap calculated with the DE with those calculated with TB and the DMB model in figure 6. The Dirac models are in fairly good agreement with TB for small antidots with size $(A_{\rm rem}/A_{\rm tot})^{1/2} < 0.15$. However, for larger antidots, there is generally a poor agreement. This is again due to the presence of localized states in the TB spectra. An interesting aspect of the TB transport gap, however, is that it is generally much higher than the TB band gap, which is given in [12]. TB predicts that the band gap almost closes for large zigzag antidots, whereas the TB transport gap does not. In fact, the TB transport gap is often higher than the one predicted by the Dirac models. This means that the transport gap of zigzag antidots can be higher than that of similarly sized armchair antidots, which contradicts the behavior of the band gap [12]. This is in good accordance with recent studies that showed that localized states in non-commensurate antidot lattices do not contribute to electronic transport [42]. Since the localized edge states typically lie beneath non-localized states, they will generally increase the transport gap. This also agrees with the results of Jippo *et al* [43] who calculated the transport gap for irregularly shaped antidots. They showed that the transport gap generally increases with the length of consecutive zigzag regions in the antidot. The transport gap of armchair antidots is highly predictable, as it follows the simple result from the DMB very accurately, whereas the transport gap of zigzag antidots is much less predictable. Therefore, even though the transport gap can be higher in some cases for zigzag antidots compared to armchair antidots, it may be an advantage to use armchair antidots in an experimental setup.

Brey and Fertig [44] have shown that by using appropriate boundary conditions in the DE, it is possible to obtain an accurate description of edge states in graphene nanoribbons with zigzag edges. They find that the A spinor element of the wave function must vanish on A-terminated edges, while the B spinor element must vanish on B-terminated edges. We can approximate the boundary conditions in the DE by introducing separate mass terms for the two sublattices and then letting the A/B mass term be non-zero only on A/B-terminated edges. Indeed, we find that this gives rise to localized states for fully periodic GALs using the method in [12]. However, the exact energies of the localized states are very sensitive to the magnitude of the mass term. It is therefore only possible to obtain a qualitative description of zigzag antidots with this approach. Unfortunately, implementing mass terms that are localized to the edges is complicated in the present area-based approach. We therefore restrict calculations to simple uniform mass terms.

3.3. Disorder

Up to now, the effect of disorder has been taken into account by convolving the TB spectra with a Gaussian. In reality, the effect of disorder is of course much more complex and needs to be studied in more detail. Ouyang *et al* [45] have shown that GALs with even neck widths, i.e. number of zigzag rows between neighboring antidots, are semiconducting, while those with odd neck widths are semimetallic. This means that randomization of antidot placement may lead to a local closing of the band gap and thus lead to local conduction channels in a GAB. Liu *et al* [46] have demonstrated that randomly oriented fullerene adsorption on pristine graphene gives rise to sizable band gaps on the order of 0.35 eV, due to the breaking of the sublattice symmetry. This indicates that a band gap, which has closed due to disorder, may recover in the presence of adsorbates. Our Dirac model is able to model any distribution of antidots, and we can thus introduce disorder by e.g. introducing randomization of antidot center location. We set up the displacement of the antidots to follow a normal distribution with a certain choice of standard deviation σ. All displacements are then mapped to the nearest graphene hexagon center in order to preserve the shape of the antidots in TB. A property of the normal distribution is that the mean displacement is given by $\sigma\sqrt{2/\pi}$. In figure 7, we show the effect of disorder for different values of σ for a 4-A{20,6}GAL barrier. As there are only 4 antidots in the unit cell, we average over transmittance spectra of several structures until the resulting spectrum does not change significantly. Figure 7 shows that the effect of disorder is more pronounced in TB than in our Dirac model. In fact, the DE spectra are almost unchanged in the presence of these amounts of disorder. In contrast, the TB transmittance maxima generally decrease with increasing disorder and new transmission peaks appear in the spectrum. For instance, a new transmission channel opens up at low energies with a peak at approximately 0.05 eV. This new channel may open due to the presence of odd neck widths between some of the antidots after random displacement, which, according to the results of Ouyang *et al*, could lead

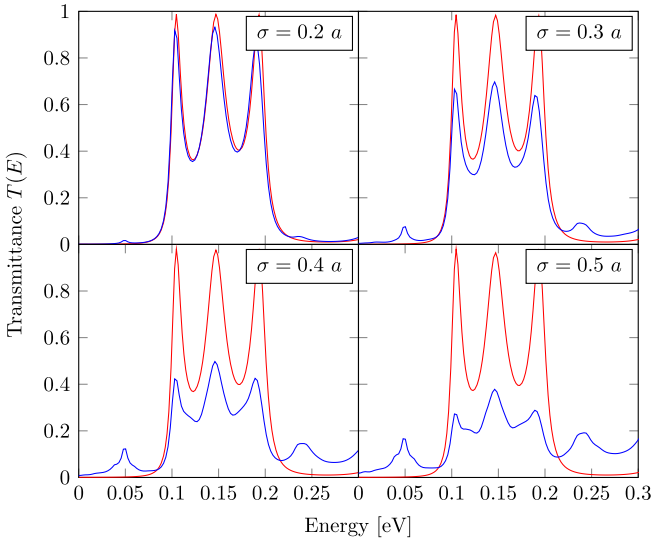

Figure 7. Average transmittance spectra of 4-A{20,6}GAL barriers for different degrees of disorder calculated with the DE (red) and TB (blue). Disorder was introduced by randomly displacing the center of the antidots according to a normal distribution.

to semimetallic regions in the barrier. The DE is a continuum model and can therefore not distinguish between the atomistic details of even and odd neck widths, and is therefore unable to predict the difference between them. It should be noted that a proper analysis of the effects of disorder requires one to construct a large supercell consisting of several disordered subcells. However, this quickly becomes very time consuming and we therefore use the original disordered GAB unit cell and then average over the results.

4. Conclusions

We use a Green's tensor area integral equation method to solve the Dirac equation with a spatially varying mass term. In this way, we are able to calculate the scattering of Dirac electrons on arbitrary graphene antidot structures. We use this method to calculate the transmittance of graphene antidot barriers with hexagonal antidots and compare them with results obtained using tight-binding. Our approach is much more general than previous attempts to use the Dirac equation to calculate scattering of Dirac electrons on antidots. The computational time of our Dirac model is scale invariant, which means that we are able to calculate properties of arbitrarily large structures. We show that our Dirac model is in excellent agreement with tight-binding for antidots with armchair edges. We also show that a simple Dirac mass barrier is able to predict the transport gap with high accuracy for antidots with armchair edges. Tight-binding predicts very localized edge states for large zigzag antidots, whereas the Dirac models do not. Therefore, the agreement between the Dirac models and tight-binding is generally poor when the barrier contains antidots with long zigzag edges. We show that the tight-binding transport gap for zigzag antidots is larger than for armchair antidots with equivalent size for some geometries, while it is lower for others. However, since the transport gap for armchair antidots is much more predictable, it may still be an advantage to use armchair antidots in an experimental setup. Furthermore, we show that a relatively narrow GAB, with only a few antidots in the unit cell, is sufficient to give rise to a transport gap. Finally, we have used our Dirac model to study disordered systems and find that it is not accurate for modeling systems with a large degree of disorder, but remains robust against relatively small amounts of disorder.

Acknowledgments

The authors gratefully acknowledge the financial support from the Center for Nanostructured Graphene (Project No. DNRF58) financed by the Danish National Research Foundation. We thank T. Søndergaard for helpful discussions on the Green's tensor area integral equation method and its numerical implementation.

References

[1] Novoselov K S, Geim a K, Morozov S V, Jiang D, Zhang Y, Dubonos S V, Grigorieva I V and Firsov A A 2004 *Science* **306** 666–9
[2] Du X, Skachko I, Barker A and Andrei E Y 2008 *Nat. Nanotechnol.* **3** 491–5
[3] Bolotin K I, Sikes K J, Jiang Z, Klima M, Fudenberg G, Hone J, Kim P and Stormer H L 2008 *Solid State Commun.* **146** 351–5
[4] Bolotin K I, Sikes K J, Hone J, Stormer H L and Kim P 2008 *Phys. Rev. Lett.* **101** 096802
[5] Han M Y, Özyilmaz B, Zhang Y and Kim P 2007 *Phys. Rev. Lett.* **98** 206805

[6] Zhang Y, Tang T T, Girit C, Hao Z, Martin M C, Zettl A, Crommie M F, Shen Y R and Wang F 2009 *Nature* **459** 820–3
[7] Xia F, Farmer D B, Lin Y m and Avouris P 2010 *Nano Lett.* **10** 715–8
[8] Balog R *et al* 2010 *Nat. Mater.* **9** 315–9
[9] Pedersen T G, Flindt C, Pedersen J G, Mortensen N A, Jauho A P and Pedersen K 2008 *Phys. Rev. Lett.* **100** 136804
[10] Fürst J A, Pedersen T G, Brandbyge M and Jauho A P 2009 *Phys. Rev.* B **80** 115117
[11] Fürst J A, Pedersen J G, Flindt C, Mortensen N A, Brandbyge M, Pedersen T G and Jauho A P 2009 *New J. Phys.* **11** 095020
[12] Brun S J, Thomsen M R and Pedersen T G 2014 *J. Phys: Condens. Matter* **26** 265301
[13] Petersen R and Pedersen T G 2009 *Phys. Rev.* B **80** 113404
[14] Vanević M, Stojanović V M and Kindermann M 2009 *Phys. Rev.* B **80** 045410
[15] Trolle M L, Møller U S and Pedersen T G 2013 *Phys. Rev.* B **88** 195418
[16] Eroms J and Weiss D 2009 *New J. Phys.* **11** 095021
[17] Giesbers A J M, Peters E C, Burghard M and Kern K 2012 *Phys. Rev.* B **86** 045445
[18] Xu Q, Wu M Y, Schneider G F, Houben L, Malladi S K, Dekker C, Yucelen E, Dunin-Borkowski R E and Zandbergen H W 2013 *ACS Nano* **7** 1566–72
[19] Bai J, Zhong X, Jiang S, Huang Y and Duan X 2010 *Nat. Nanotechnol.* **5** 190–4
[20] Kim M, Safron N S, Han E, Arnold M S and Gopalan P 2010 *Nano lett.* **10** 1125–31
[21] Kim M, Safron N S, Han E, Arnold M S and Gopalan P 2012 *ACS Nano* **6** 9846–54
[22] Zeng Z, Huang X, Yin Z, Li H, Chen Y, Li H, Zhang Q, Ma J, Boey F and Zhang H 2012 *Adv. Mater.* **24** 4138–42
[23] Wang M, Fu L, Gan L, Zhang C, Rümmeli M, Bachmatiuk A, Huang K, Fang Y and Liu Z 2013 *Sci. Rep.* **3** 1238
[24] Liang X, Jung Y S, Wu S, Ismach A, Olynick D L, Cabrini S and Bokor J 2010 *Nano Lett.* **10** 2454–60
[25] Jia X *et al* 2009 *Science* **323** 1701–5
[26] Girit Ç Ö *et al* 2009 *Science* **323** 1705–8
[27] Oberhuber F, Blien S, Heydrich S, Yaghobian F, Korn T, Schüller C, Strunk C, Weiss D and Eroms J 2013 *Appl. Phys. Lett.* **103** 143111
[28] Schwierz F 2010 *Nat. Nanotechnol.* **5** 487–96
[29] Pedersen T G and Pedersen J G 2012 *J. Appl. Phys.* **112** 113715
[30] Gunst T, Markussen T, Jauho A P and Brandbyge M 2011 *Phys. Rev.* B **84** 155449
[31] Pedersen J G, Gunst T, Markussen T and Pedersen T G 2012 *Phys. Rev.* B **86** 245410
[32] Berrada S, Nguyen V H, Querlioz D, Saint-Martin J, Alarcón A, Chassat C, Bournel A and Dollfus P 2013 *Appl. Phys. Lett.* **103** 183509
[33] Masir M R, Matulis A and Peeters F M 2011 *Phys. Rev.* B **84** 245413
[34] Heinisch R L, Bronold F X and Fehske H 2013 *Phys. Rev.* B **87** 155409
[35] Gomes J V and Peres N M R 2008 *J. Phys: Condens. Matter* **20** 325221
[36] Søndergaard T 2007 *Phys. Stat. Sol.* **244** 3448–62
[37] Novotny L and Hecht B 2006 *Principles of nano-optics* (Cambridge University Press)
[38] Abramovitz M and Stegun I A (eds) 1965 *Handbook of Mathematical Functions* (New York: Dover Publications)
[39] Yasumoto K and Yoshitomi K 1999 *IEEE Trans. Antennas Propag.* **47** 1050–5
[40] Datta S (ed) 1997 *Electronic Transport in Mesoscopic Systems* (Cambridge: Cambridge University Press)
[41] Zhang Y T, Li Q M, Li Y C, Zhang Y Y and Zhai F 2010 *J. Phys.: Condens. Matter* **22** 315304
[42] Lopata K, Thorpe R, Pistinner S, Duan X and Neuhauser D 2010 *Chem. Phys. Lett.* **498** 334–7
[43] Jippo H, Ohfuchi M and Kaneta C 2011 *Phys. Rev.* B **84** 075467
[44] Brey L and Fertig H A 2006 *Phys. Rev.* B **73** 235411
[45] Ouyang F, Peng S, Liu Z and Liu Z 2011 *ACS nano* **5** 4023–30
[46] Liu X, Wen Y, Chen Z, Lin H, Chen R, Cho K and Shan B 2013 *AIP Adv.* **3** 052126

Publication III

Stability and magnetization of free-standing and graphene-embedded iron membranes

Morten Rishøj Thomsen, Søren Jacob Brun and Thomas Garm Pedersen

The paper has been published in
Physical Review B **91**, 125439 (2015).

Stability and magnetization of free-standing and graphene-embedded iron membranes

M. R. Thomsen, S. J. Brun, and T. G. Pedersen
Department of Physics and Nanotechnology, Aalborg University, DK-9220 Aalborg Øst, Denmark
and Center for Nanostructured Graphene (CNG), DK-9220 Aalborg Øst, Denmark
(Received 19 November 2014; revised manuscript received 13 March 2015; published 30 March 2015)

Inspired by recent experimental realizations of monolayer Fe membranes in graphene perforations, we perform *ab initio* calculations of Fe monolayers and membranes embedded in graphene in order to assess their structural stability and magnetization. We demonstrate that monolayer Fe has a larger spin magnetization per atom than bulk Fe and that Fe membranes embedded in graphene exhibit spin magnetization comparable to monolayer Fe. We find that free-standing monolayer Fe is structurally more stable in a triangular lattice compared to both square and honeycomb lattices. This is contradictory to the experimental observation that the embedded Fe membranes form a square lattice. However, we find that embedded Fe membranes in graphene perforations can be more stable in the square lattice configuration compared to the triangular. In addition, we find that the square lattice has a lower edge formation energy, which means that the square Fe lattice may be favored during formation of the membrane.

DOI: 10.1103/PhysRevB.91.125439 PACS number(s): 75.75.−c, 61.48.Gh, 75.50.Bb, 75.70.Ak

I. INTRODUCTION

In recent years, there has been a tremendous interest in graphene and its derivatives, owing to their remarkable electronic properties, such as ultrahigh mobility of 1 000 000 cm^2/Vs at low temperature [1]. These properties make graphene interesting for electronic and spintronic applications. Carbon-based spintronic devices may have a distinct advantage over many other materials in that carbon has a very low spin-orbit coupling together with an absence of hyperfine interaction in the predominant ^{12}C isotope. This results in long spin lifetimes [2–4], as well as large spin relaxation lengths, which have been found to be on the order of several microns at room temperature [2–5] and make graphene ideal for ballistic spin transport [6].

Pristine graphene is nonmagnetic, but several suggestions on how to give graphene magnetic properties have been put forward. Density functional theory (DFT) calculations have shown that ferromagnetism can be introduced in graphene by, e.g., semihydrogenation [7], adding vacancies [8,9], or adding adatoms [9–14]. Semihydrogenating graphene sheets, where one sublattice is fully hydrogenated while the other is not, leads to a sublattice imbalance, which induces a magnetic moment of $1\mu_B$ per unit cell [7]. Monovacancies in graphene have also been demonstrated to have a magnetic moment between $1.04\mu_B$ [8] and $1.48\mu_B$ [9]. Lehtinen *et al.* [8] find that the spin-polarized state may be unstable, and find that it can be stabilized by adsorption of two hydrogen atoms in the vacancy, with a resulting magnetic moment of $1.2\mu_B$. The spin of a vacancy generally increases with the number of missing carbon atoms, except for the divacancy where the magnetic moment is vanishing [9]. Ferromagnetism can also be induced by transition metal adatoms on graphene or in graphene vacancies. Transition metal adatoms in graphene and single-walled carbon nanotubes were studied by Zanella *et al.* [10] and Fagan *et al.* [15], respectively. In particular, they find that the spin moment of Fe adatoms is largely unaffected by the presence of carbon. Zanella *et al.* find that the spin moment of Fe adsorbed on graphene is either 2 or $4\mu_B$ depending on the adsorption site, while Fagan *et al.* find that the spin moment of Fe adsorbed on a carbon nanotube is about $3.9\mu_B$ independent of adsorption site. DFT calculations show that a single Fe adatom on a graphene monovacancy is nonmagnetic [11–13]. However, by adding a Hubbard U term to the GGA functional, Santos *et al.* [12] showed that this state may, in fact, be magnetic with a spin moment of $1\mu_B$, and that the nonmagnetic properties predicted by the GGA calculation is a consequence of the limitations of the functional itself. Nevertheless, the spin moment of a single Fe adatom on a graphene monovacancy is strongly decreased compared to free Fe, due to the Fe-C interaction. A single Fe adatom in a graphene divacancy, however, has a spin moment of about $3.2\mu_B$ according to Krasheninnikov *et al.* [11], and $3.55\mu_B$ according to He *et al.* [13]. The reason for the increased spin is quite obvious; the larger vacancy increases the Fe-C distance and thus decreases the interaction between Fe and C. As the interaction between Fe and C seems to decrease the spin moment of Fe, we expect Fe-C systems to have decreased spins compared to a pure Fe system. Trapping larger Fe clusters in graphene perforations will lead to a larger spin moment, which combined with the electrical properties of graphene, might make this a suitable system for graphene-based spintronics.

Trapping of metal atoms, such as Fe and Mo, in graphene and carbon nanotube vacancies have been achieved experimentally in transmission electron microscopy (TEM) [14,16]. Vacancies are created under e-beam irradiation, after which mobile metal atoms on the surface move to the vacancy, where they are trapped. These trapped metals are stable for some time, but detrapping of some of the atoms has been observed over time [14,16], which is thought to occur due to weak bonding, e-beam irradiation, or high temperature during the experiments. Recent experimental results by Zhao *et al.* [17] show that monolayer Fe membranes can be grown in graphene perforations. These monolayer membranes both form and collapse under e-beam irradiation in TEM. The Fe is provided via leftover residue from the transfer process, where graphene is transferred from growth substrate to target substrate. Electron energy loss spectroscopy (EELS) and high-angle annular dark-field (HAADF) measurements suggest that the embedded membranes are composed of pure Fe. They find

that the embedded Fe membranes form a square lattice with a lattice constant of about 2.65 Å. Through density functional theory (DFT) calculations, Zhao *et al.* find that monolayer Fe is most stable in a square configuration with a lattice constant of 2.35 Å. They argue that the difference between observed and calculated lattice constant may be a result from straining due to lattice alignment and mismatch between the Fe membrane and graphene.

In this paper, we present a DFT analysis of the structural stability and magnetization of Fe systems in an attempt to obtain a basic understanding of these systems, as well as to explain the experimental results by Zhao *et al.* [17]. In particular, we compare the stability of Fe in square and triangular lattice configurations for both monolayer Fe, monolayer Fe carbide and Fe embedded in graphene perforations. We model embedded Fe membranes as a periodic system, effectively giving rise to graphene antidot lattices (GALs), where the antidots are filled with Fe. GALs, which are periodic perforations in an otherwise pristine graphene sheet, can be produced experimentally by, e.g., e-beam lithography on pristine graphene [18,19]. It is possible that the embedding of iron in graphene perforations can be scaled up to actual Fe-filled GALs. GALs have tunable band gaps that depend on geometric factors [20,21], which make them interesting for electronic and optoelectronic applications. It has been shown that a narrow slice of GAL with just a few rows connected to graphene sheets on either side is sufficient to block electron transport in the energy gap of the GAL [22,23]. By omitting antidots in some regions of such a GAL barrier, electrons can be guided through the unpatterned part, giving rise to an electronic waveguide [24], reminiscent of a photonic waveguide in a photonic crystal.

II. THEORETICAL METHODS

Spin-polarized DFT calculations were performed using the ABINIT package [25–28], which uses a plane-wave basis set to expand the wave function. We have used the Perdew-Burke-Ernzerhof GGA (PBE-GGA) exchange and correlation functional [29] in all calculations. We use a plane-wave cutoff energy of 435 eV combined with the projector-augmented wave (PAW) method [30]. It has previously been demonstrated that the PAW method is able to accurately describe magnetism in transition metal systems [30,31]. We use a Fermi smearing of 0.27 eV in order for a $16 \times 16 \times 1$ Monkhorst-Pack k-point grid to be adequate. The Fermi smearing has the effect of slightly lowering the magnetic moment as electrons will have a probability to occupy states above the Fermi level. An interlayer spacing of 10 Å was used in all calculations. Full relaxation of all atoms in the unit cells were made for all structures, in addition to relaxation of the unit cell size in the case of free-standing monolayer Fe and iron carbide. Atomic coordinates were optimized until the maximum force on atoms was smaller than 0.05 eV/Å. These parameters have previously been shown to be adequate for modeling transition metal adatoms on graphene vacancies [8,11]. The same parameters are used when calculating the edge formation energy, except the k-point sampling is reduced to $16 \times 1 \times 1$, due to a lateral distance between ribbons of 10 Å.

III. FREE-STANDING MONOLAYER SYSTEMS

A. Monolayer iron

In order to obtain an understanding of iron membranes embedded in graphene perforations, we first determine the stability of free-standing monolayer iron in different lattice configurations. Then, we calculate the edge formation energy of monolayer iron, in order to obtain an understanding of the formation kinetics of iron membranes. Lastly, we determine the stability of iron membranes embedded in graphene antidots for certain hole sizes.

The binding energy and magnetization of free-standing monolayer iron in square, triangular, and honeycomb lattice configurations are shown in Fig. 1. The antiferromagnetic square and honeycomb lattices are made such that each atom only has nearest neighbors with opposite spin. This is not possible in the triangular lattice, so we chose an antiferromagnetic lattice that essentially consists of spin-polarized lines, where each atom has opposite spin to four of its six nearest neighbors. We do not expect this configuration to be physically sound, but we include it in order to compare with the other lattice configurations. We use the smallest possible unit cells, which means that the ferromagnetic unit cells of the square and triangular lattice contain one atom and the honeycomb lattice contains two. In the antiferromagnetic case, all three unit cells contain two atoms. The figure shows that ferromagnetic ordering is generally favored over antiferromagnetic ordering, consistent with earlier results which show that monolayer Fe

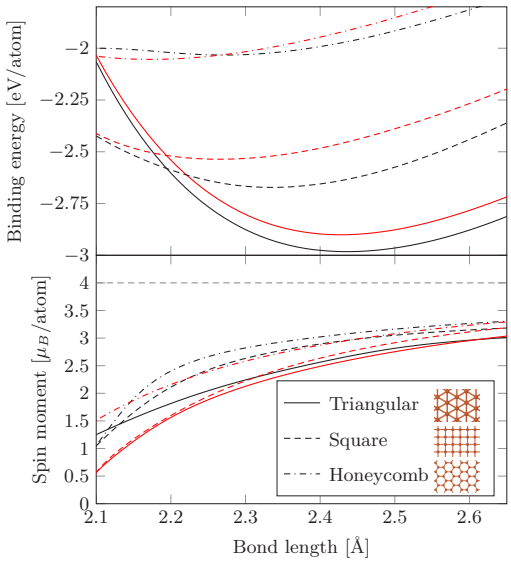

FIG. 1. (Color online) Binding energy (upper panel) and spin moment (lower panel) of monolayer Fe as a function of bond length. The black and red lines are for ferromagnetic and antiferromagnetic ordering, respectively. The magnitude of the spin is shown in case of antiferromagnetic ordering, as it has zero net spin. The dashed gray line indicates the spin of free Fe.

in the square lattice favors ferromagnetic ordering [32]. The figure also shows that the honeycomb lattice is unfavored compared to the square and triangular lattices. We therefore exclude antiferromagnetic ordering as well as the honeycomb lattice in the remaining calculations. In addition, the figure shows that the most stable configuration is the ferromagnetic triangular lattice, as it has the lowest binding energy at equilibrium. However, it is seen that, under compressive strain, the ferromagnetic square lattice eventually becomes favored. The spin moments per atom at equilibrium are $2.73\mu_B$ and $2.68\mu_B$ for the square and triangular lattice, respectively, which is significantly larger than the bulk spin moment of $2.22\mu_B$ [33]. Our results for the spin of the ferromagnetic triangular lattice are in good agreement with previous results [34,35].

As expected, we see that the spin moment increases with increasing distance between the Fe atoms, as the spin tends towards $4\mu_B$ for free Fe. We notice that the bond length at equilibrium of the square lattice is 2.33 Å, which is significantly lower than the experimental results of 2.65 Å by Zhao *et al.* [17], suggesting that the Fe membranes are strained by the surrounding graphene. In addition, it is seen that the energy cost of straining the square lattice to 2.65 Å is only about 0.2 eV per atom. Our predictions of the lattice constant and energy cost of straining for the square monolayer Fe lattice are very close to the theoretical results by Zhao *et al.* The major difference between the results is that we find the triangular lattice to be more stable, whereas Zhao *et al.* find that the square lattice is more stable, in agreement with their experimental observations that Fe embedded in graphene perforations forms a square lattice. The differences in the calculations are that we use a plane wave basis set and a $16 \times 16 \times 1$ k-point sampling, whereas Zhao *et al.* use a localized basis and a $3 \times 3 \times 1$ k-point sampling. The elementary unit cells for monolayer Fe are very small, and we find that a $3 \times 3 \times 1$ k-point sampling is insufficient for obtaining converged spin magnetization and total energy. We therefore believe that the discrepancy arises due to the different k-point sampling.

B. Edge energy of monolayer iron

We have demonstrated that the triangular lattice is energetically favored over the square lattice, so in order to explain why the square lattice is formed experimentally, we now analyze the edge formation energy by comparing the energy of an Fe nanoribbon and monolayer Fe. The edge formation energy per length is given by $E_{\text{edge}} = (E_{\text{ribbon}} - NE_{\text{monolayer}})/2l$, where l is the length of the unit cell in the direction of the ribbon edge, E_{ribbon} is the total energy of the nanoribbon unit cell, N is the number of atoms in the unit cell, and $E_{\text{monolayer}}$ is the energy per atom of the monolayer system. The factor of $1/2$ is due to the fact that a nanoribbon has two edges. For both the square and the triangular lattice, we examine two different rotations of the edges, as shown in Fig. 2.

In Fig. 3(a) we observe that the triangular lattice has a larger edge formation energy than the square lattice for both rotations of both lattices. This means that, during formation of the membrane, the square lattice may be favored due to the lower edge formation energy. The membrane may then be kinetically hindered from subsequently rearranging into the triangular lattice. It is seen in Fig. 3(b) that the bond length contracts on the edges of the ribbon, while the remaining structure is almost unchanged. This indicates that the large experimentally observed lattice constant is not due to formation kinetics.

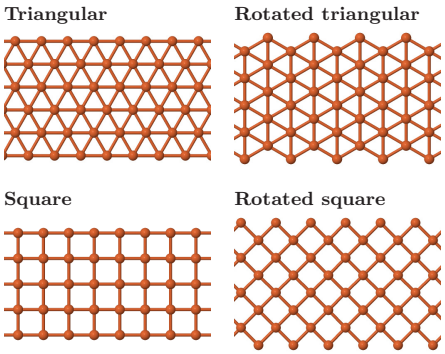

FIG. 2. (Color online) Geometries used for evaluation of edge energies.

C. Iron carbide

Another possibility is that the experimentally observed structure is, in fact, an iron carbide. Zhao *et al.* state that relatively small amounts of carbon may lie beyond the

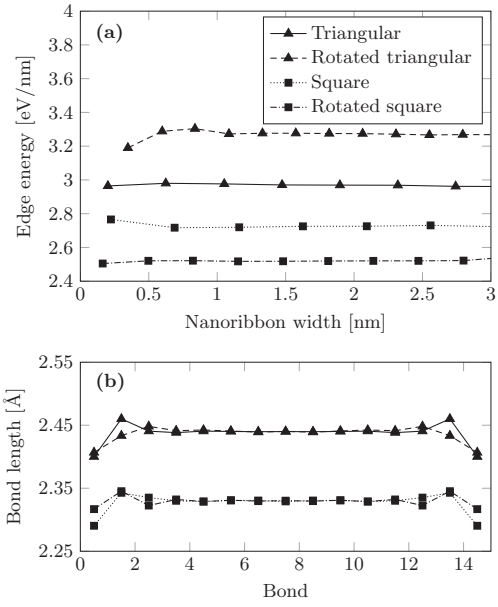

FIG. 3. (a) Edge formation energy for square and triangular Fe nanoribbons as a function of nanoribbon width. (b) Bond lengths through a 16-atom-wide Fe nanoribbon with different orientations and edge rotations.

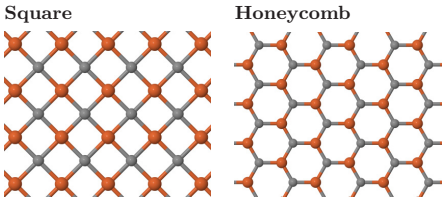

FIG. 4. (Color online) Iron carbides with square and honeycomb arrangements. The gray balls are C and the orange balls are Fe.

detection limits of their EELS setup and therefore cannot exclude the possibility that the membrane is made of iron carbide. It is also very difficult to observe C atoms near Fe in TEM due to the large difference in contrast. The iron carbides shown in Fig. 4 have binding energies per unit cell of -9.91 eV and -9.49 eV for the square and honeycomb lattice, respectively. The square lattice is thus the most stable configuration. The sum of the binding energy of separate monolayer Fe and graphene systems is -10.37 eV. The energy difference between the separate systems and the iron carbide is just 0.46 eV, which suggests that the iron carbide in square arrangement could be metastable. In particular, it is interesting to note that the lattice constant, i.e., the Fe-Fe distance, of the square iron carbide is 2.66 Å, which is extremely close to the experimentally observed value. However, since we find the structure to be, at best, metastable and no carbon signal was observed in EELS experiments, we are still skeptical that the observed structure is, in fact, iron carbide. More accurate measurements are needed in order to exclude the possibility of the membranes consisting of iron carbide.

IV. EMBEDDED IRON

We will now study the structural stability and magnetization of Fe membranes embedded in graphene perforations. In order to model this with DFT, we impose periodic boundary conditions, which means we effectively have a graphene antidot lattice (GAL), where the antidots are filled with Fe. We use the conventional $\{L,S\}$ notation to denote GALs with unit cell side length L and antidot side length S, both in units of the graphene lattice constant, consistent with earlier work [36]. By filling a given antidot with the same amount of Fe atoms in the square and triangular configurations, we can make a direct comparison of the stability of the two systems by comparing their binding energies. In particular, we compare 12 and 21 Fe atoms embedded in a {4,2} and a {5,3} antidot lattice with hexagonal hole geometry, respectively. These antidot lattices are chosen because both square and triangular lattice configurations with an equal amount of Fe atoms can be found that conform fairly well with the antidots. Figure 5 shows the structures after relaxation of all atoms in the unit cell.

The figure shows that the surrounding graphene is almost unaffected by the presence of Fe, due to the large in-plane strength of graphene. It is also seen that the Fe bulges out-of-plane for the small antidots, especially for Fe in square arrangement. This indicates that the square lattice does not conform as well to the graphene lattice as the triangular lattice

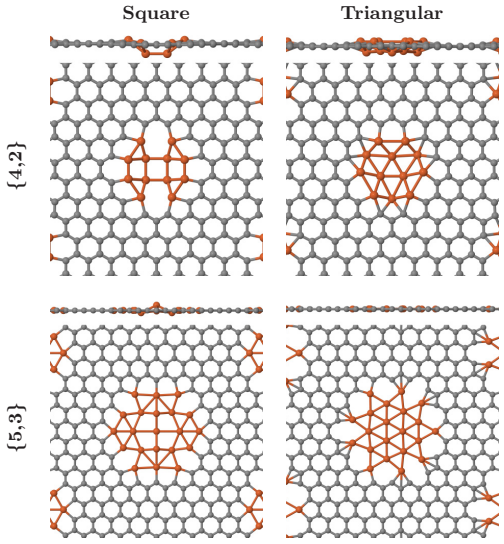

FIG. 5. (Color online) Top and side view of structurally relaxed graphene antidots with embedded Fe.

does for the small antidot. In the larger antidot, the Fe is seen to be mostly co-planer with the graphene, which indicates that both lattice configurations conform better to the graphene lattice. The Fe still bulges slightly out-of-plane in the square lattice configuration, which indicates that the square lattice still conforms worse to the graphene lattice than the triangular lattice. By comparing the binding energies of the two systems, we can determine which of the Fe configurations is more stable.

The unit cells we consider are probably too small for the spins to be decoupled between neighboring cells. This means that the magnitude of the magnetic moment may differ for isolated Fe membranes in graphene. However, due to the high strength of the supporting graphene lattice, we expect that structural properties will be in quantitative agreement with isolated Fe membranes.

We find that the triangular lattice is favored in the {4,2} antidot lattice with a binding energy difference of 2.31 eV, while the square lattice is favored in the {5,3} antidot lattice with a binding energy difference of 1.37 eV. The fact that the square lattice is favored in the large antidot, despite conforming worse to the graphene lattice, indicates that the square lattice has a larger binding energy to graphene than the triangular lattice. We therefore presume that the square lattice will have a greater advantage in larger antidots, where it conforms better to the graphene lattice. However, when the Fe membrane grows too large, the "bulk" behavior should overcome edge or interface effects, which should lead to formation of the triangular Fe lattice. Moreover, there is still the possibility that a 3D nanocrystal could form instead of the triangular monolayer membrane as the 3D structure, in principle, has lower energy than the 2D counterpart for sufficiently large structures. We thus speculate that there is an antidot size regime, where the square Fe lattice is favored, but

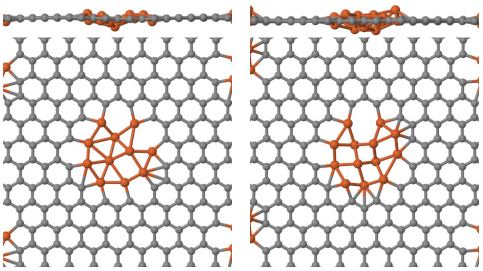

FIG. 6. (Color online) Top and side view of structurally relaxed {4,2} graphene antidot lattices with 11 (left) and 13 (right) Fe atoms.

when the antidots become too large, either the triangular monolayer Fe lattice or a 3D nanocrystal will be formed instead. However, we cannot investigate the extent of this regime further, due to the computational complexity of the DFT calculations.

In the analysis of the {4,2} unit cell, the choice of 12 Fe atoms was made to ensure a symmetric structure in both triangular and square arrangements. In order to substantiate our conclusions regarding the relative stability of these arrangements, we now investigate the {4,2} unit cell with a varying number of Fe atoms. In this case, we place the Fe atoms asymmetrically in the unit cell to obtain convergence to the global structural minimum. For the structure with 12 Fe atoms, the fully relaxed structure is the triangular one shown in the top right in Fig. 5. We find that a structure with 11 Fe atoms is more stable than the structures with either 12, 13, or 14 Fe atoms. The difference in binding energy per atom between the structure with 11 and 12 Fe atoms is only 30 meV, however, which is much smaller than the difference in binding energy obtained by changing the lattice configuration between square and triangular. The relaxed structures in the cases of 11 and 13 Fe atoms are shown in Fig. 6. The figure shows that the structure with 11 Fe atoms approximately forms a triangular

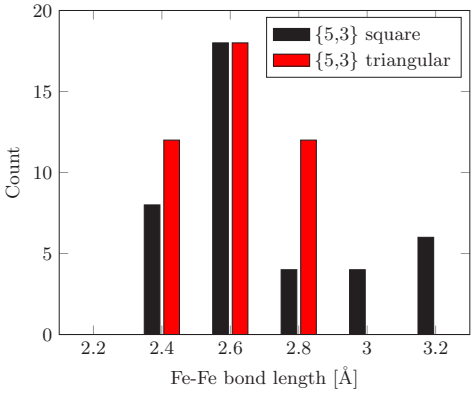

FIG. 7. (Color online) Fe-Fe bond lengths of the two {5,3} structures shown in Fig. 5.

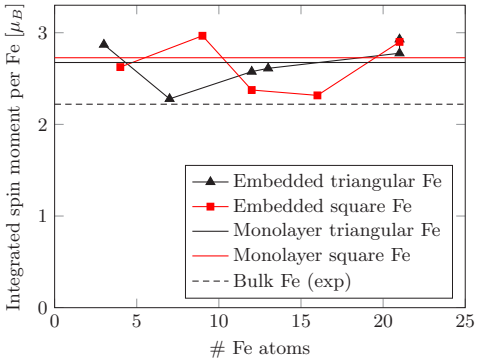

FIG. 8. (Color online) Integrated spin moment per atom for Fe membranes embedded in graphene antidots.

lattice, which is however a bit distorted because there is no longer any symmetric way to arrange the atoms. Furthermore, we see that the structure with 13 Fe atoms forms a square lattice, but it is no longer planar, simply because there is not enough room in the antidot to support a planar structure with this many Fe atoms. The conclusion that the triangular lattice

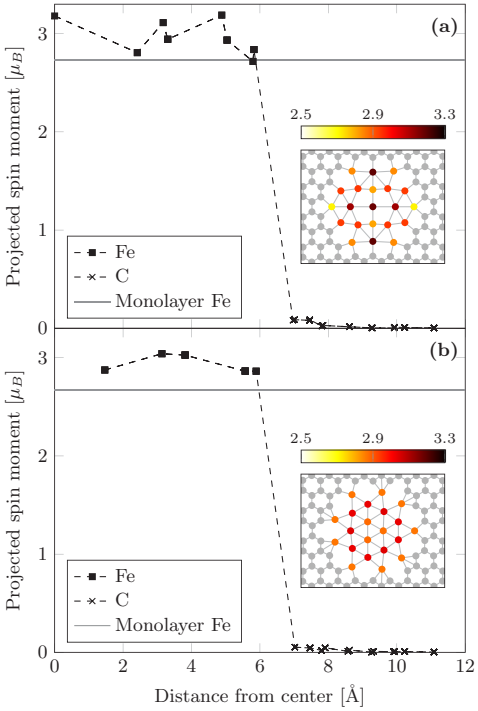

FIG. 9. (Color online) Projected spin moment for a {5,3} graphene antidot lattice with 21 Fe atoms in a hexagonal antidot in (a) square arrangement and (b) triangular arrangement.

is stable in the {4,2} unit cell is thus unchanged when varying the number of Fe atoms by a few units.

We saw previously that there was a rather large discrepancy between the bond lengths of the bulk monolayer Fe and the one measured in the experiments. To further investigate this discrepancy we have counted all the Fe-Fe bond lengths in the two {5,3} antidot structures in Fig. 7. The figure shows that the Fe-Fe bond length inside the graphene antidots is generally quite close to the one measured experimentally, with a mean value of 2.7 Å and 2.6 Å in the square and triangular cases, respectively. The square lattice is thus strained by about 16% on average compared to the bulk monolayer value. By comparison, the mean C-C bond length is almost unaffected by the interface with a mean value of 1.43 Å in both cases.

Figure 8 shows that the spin moment per Fe atom embedded in graphene antidots is around the value of monolayer Fe even for very few embedded Fe atoms. In contrast to Fe in a graphene monovacancy, where the spin moment is vanishing, the spin moment is only weakly affected by the presence of carbon on the edge. In fact, the spin moment may in some cases even exceed the monolayer value, due to the increased bond lengths. This is consistent with the result for Fe in a graphene divacancy, where the spin moment is also only weakly affected by the presence of carbon. This effect can be seen directly in Fig. 9, which shows the projected spin moment as a function of distance from the center of the antidot for a {5,3} graphene antidot lattice with 21 Fe atoms. The projected spin moment is calculated by integrating the difference in spin-up and spin-down electron densities inside the Voronoi volume associated with each atom. The figure shows that there is, in fact, an enhanced spin moment on nearly all Fe atoms in this case.

V. CONCLUSIONS

We have studied the stability of monolayer Fe and graphene-embedded Fe through *ab initio* calculations. We find that the most stable configuration of monolayer Fe is the ferromagnetic triangular lattice with a lattice constant of 2.44 Å. This is in contrast to experimental results of graphene-embedded Fe, which shows that these structures have a square lattice configuration with a bond length of 2.65 Å. However, we find that the square lattice configuration has a lower edge formation energy. This means that, during formation, it might be favorable to form the square lattice and the structure could then be kinetically hindered from subsequently rearranging to the triangular lattice. Furthermore, we have compared the stability of the square and triangular Fe lattices in two different graphene antidot lattices. In the larger one of these, the square lattice is, in fact, more stable than the triangular lattice, with a mean Fe-Fe bond length of 2.7 Å. This result is in very close agreement with the experimental results. Our results show that only a few Fe atoms in the graphene antidots are sufficient to give rise to magnetic moments, which are comparable to the magnetic moment of monolayer Fe.

ACKNOWLEDGMENTS

The authors gratefully acknowledge the financial support from the Center for Nanostructured Graphene (Project No. DNRF58) financed by the Danish National Research Foundation and from the QUSCOPE project financed by the Villum Foundation.

[1] L. Wang, I. Meric, P. Y. Huang, Q. Gao, Y. Gao, H. Tran, T. Taniguchi, K. Watanabe, L. M. Campos, D. A. Muller, J. Guo, P. Kim, J. Hone, K. L. Shepard, and C. R. Dean, Science **342**, 614 (2013).

[2] W. Han, R. K. Kawakami, M. Gmitra, and J. Fabian, Nat. Nanotechnol. **9**, 794 (2014).

[3] M. H. D. Guimarães, P. J. Zomer, J. Ingla-Aynés, J. C. Brant, N. Tombros, and B. J. van Wees, Phys. Rev. Lett. **113**, 086602 (2014).

[4] M. Drögeler, F. Volmer, M. Wolter, B. Terrés, K. Watanabe, T. Taniguchi, G. Güntherodt, C. Stampfer, and B. Beschoten, Nano Lett. **14**, 6050 (2014).

[5] N. Tombros, C. Jozsa, M. Popinciuc, H. T. Jonkman, and B. J. Van Wees, Nature (London) **448**, 571 (2007).

[6] M. Weser, E. N. Voloshina, K. Horn, and Y. S. Dedkov, Phys. Chem. Chem. Phys. **13**, 7534 (2011).

[7] J. Zhou, Q. Wang, Q. Sun, X. Chen, Y. Kawazoe, and P. Jena, Nano Lett. **9**, 3867 (2009).

[8] P. O. Lehtinen, A. S. Foster, Y. Ma, A. V. Krasheninnikov, and R. M. Nieminen, Phys. Rev. Lett. **93**, 187202 (2004).

[9] S. Haldar, B. S. Pujari, S. Bhandary, F. Cossu, O. Eriksson, D. G. Kanhere, and B. Sanyal, Phys. Rev. B **89**, 205411 (2014).

[10] I. Zanella, S. B. Fagan, R. Mota, and A. Fazzio, J. Phys. Chem. C **112**, 9163 (2008).

[11] A. V. Krasheninnikov, P. O. Lehtinen, A. S. Foster, P. Pyykkö, and R. M. Nieminen, Phys. Rev. Lett. **102**, 126807 (2009).

[12] E. J. G. Santos, A. Ayuela, and D. Sánchez-Portal, New J. Phys. **12**, 053012 (2010).

[13] Z. He, K. He, A. W. Robertson, A. I. Kirkland, D. Kim, J. Ihm, E. Yoon, G.-D. Lee, and J. H. Warner, Nano Lett. **14**, 3766 (2014).

[14] J. A. Rodrígues-Manzo, O. Cretu, and F. Banhart, ACS Nano **4**, 3422 (2010).

[15] S. B. Fagan, R. Mota, A. J. R. da Silva, and A. Fazzio, Phys. Rev. B **67**, 205414 (2003).

[16] A. W. Robertson, B. Montanari, K. He, J. Kim, C. S. Allen, Y. A. Wu, J. Olivier, J. Neethling, N. Harrison, A. I. Kirkland, and J. H. Warner, Nano Lett. **13**, 1468 (2013).

[17] J. Zhao, Q. Deng, A. Bachmatiuk, G. Sandeep, A. Popov, J. Eckert, and M. H. Rümmeli, Science **343**, 1228 (2014).

[18] J. Eroms and D. Weiss, New J. Phys. **11**, 095021 (2009).

[19] A. J. M. Giesbers, E. C. Peters, M. Burghard, and K. Kern, Phys. Rev. B **86**, 045445 (2012).

[20] T. G. Pedersen, C. Flindt, J. G. Pedersen, N. A. Mortensen, A.-P. Jauho, and K. Pedersen, Phys. Rev. Lett. **100**, 136804 (2008).

[21] S. J. Brun, M. R. Thomsen, and T. G. Pedersen, J. Phys.: Condens. Matter **26**, 265301 (2014).

[22] T. G. Pedersen and J. G. Pedersen, J. Appl. Phys. **112**, 113715 (2012).
[23] M. R. Thomsen, S. J. Brun, and T. G. Pedersen, J. Phys.: Condens. Matter **26**, 335301 (2014).
[24] J. G. Pedersen, T. Gunst, T. Markussen, and T. G. Pedersen, Phys. Rev. B **86**, 245410 (2012).
[25] X. Gonze, J.-M. Beuken, R. Caracas, F. Detraux, M. Fuchs, G.-M. Rignanese, L. Sindic, M. Verstraete, G. Zerah, F. Jollet, M. Torrent, A. Roy, M. Mikami, Ph. Ghosez, J.-Y. Raty, and D. C. Allan, Comp. Mater. Sci. **25**, 478 (2002).
[26] X. Gonze, B. Amadon, P.-M. Anglade, J.-M. Beuken, F. Bottin, P. Boulanger, F. Bruneval, D. Caliste, R. Caracas, M. Côté, T. Deutsch, L. Genovese, Ph. Ghosez, M. Giantomassi, S. Goedecker, D. R. Hamann, P. Hermet, F. Jollet, G. Jomard, S. Leroux, M. Mancini, S. Mazevet, M. J. T. Oliveira, G. Onida, Y. Pouillon, T. Rangel, G.-M. Rignanese, D. Sangalli, R. Shaltaf, M. Torrent, M. J. Verstraete, G. Zerah, and J. W. Zwanziger, Comput. Phys. Commun. **180**, 2582 (2009).
[27] F. Bottin, S. Leroux, A. Knyazev, and G. Zérah, Comp. Mater. Sci. **42**, 329 (2008).
[28] M. Torrent, F. Jollet, F. Bottin, G. Zérah, and X. Gonze, Comp. Mater. Sci. **42**, 337 (2008).
[29] J. P. Perdew, K. Burke, and M. Ernzerhof, Phys. Rev. Lett. **77**, 3865 (1996).
[30] G. Kresse and D. Joubert, Phys. Rev. B **59**, 1758 (1999).
[31] G. Kresse, W. Bergermayer, and R. Podloucky, Phys. Rev. B **66**, 146401 (2002).
[32] S. Blügel, B. Drittler, R. Zeller, and P. Dederichs, Appl. Phys. A **49**, 547 (1989).
[33] *CRC Handbook of Chemistry and Physics*, 95th ed., edited by W. M. Haynes (CRC Press, Boca Raton, Florida, USA, 2014).
[34] J. C. Boettger, Phys. Rev. B **47**, 1138 (1993).
[35] S. Achilli, S. Caravati, and M. I. Trioni, J. Phys.: Condens. Matter **19**, 305021 (2007).
[36] M. L. Trolle, U. S. Møller, and T. G. Pedersen, Phys. Rev. B **88**, 195418 (2013).

Publication IV

Spin relaxation in hydrogenated graphene

Morten Rishøj Thomsen, Mikko M. Ervasti, Ari Harju and
Thomas Garm Pedersen

The paper has been published in
Physical Review B **92**, 195408 (2015).

Spin relaxation in hydrogenated graphene

M. R. Thomsen,[1,2] M. M. Ervasti,[3] A. Harju,[3] and T. G. Pedersen[1,2]
[1]*Department of Physics and Nanotechnology, Aalborg University, DK-9220 Aalborg Øst, Denmark*
[2]*Center for Nanostructured Graphene (CNG), DK-9220 Aalborg Øst, Denmark*
[3]*COMP Centre of Excellence, Department of Applied Physics, Aalto University, Helsinki, Finland*
(Received 17 July 2015; revised manuscript received 3 September 2015; published 9 November 2015)

We calculate the spin transport of hydrogenated graphene using the Landauer-Büttiker formalism with a spin-dependent tight-binding Hamiltonian. Hydrogen adatoms are a common defect and they carry a finite magnetic moment, which makes it important to understand their influence on spin transport for graphene-based spin devices. Our tight-binding model accurately reproduces the density-functional theory band structure and atom-projected density of states. The advantages of using the Landauer-Büttiker formalism are that it simultaneously gives information on sheet resistance and localization length as well as spin relaxation length. Furthermore, the transport can be computed very efficiently using this method by employing the recursive Green's function technique. Here, we study hydrogen adatoms on graphene with randomly aligned magnetic moments, where interference effects are explicitly included. We show that a 5 ppm hydrogen defect density is sufficient to reduce the spin relaxation length to 2 μm and that the inverse spin relaxation length and sheet resistance scale nearly linearly with the impurity concentration. Moreover, the spin relaxation mechanism in hydrogenated graphene is Markovian only near the charge neutrality point or in the highly dilute impurity limit.

DOI: 10.1103/PhysRevB.92.195408 PACS number(s): 72.25.−b, 72.10.Fk, 72.80.Vp

I. INTRODUCTION

Spin transport in graphene has attracted a lot of attention in recent years due to very long spin relaxation times and spin relaxation lengths predicted for this material [1,2]. The spin relaxation length in graphene has been predicted theoretically to be at least 20 μm [1] for experimentally realistic device parameters, whereas experimental values are about an order of magnitude lower, typically around 1–4 μm [3–8], but has been observed as large as around 200 μm in short samples at low temperature [9] and 12 μm in encapsulated graphene at room temperature [10]. It has been ruled out experimentally that this discrepancy is due to hyperfine interactions with the naturally occurring ^{13}C isotope in graphene [7]. Experimental measurements of graphene in the presence of a strong magnetic field show that the observed low spin relaxation length is, at least in part, due to magnetic impurities in graphene [11]. Magnetic impurities are very common in graphene and may, for instance, be hydrogen adatoms [12], vacancies [12,13], or embedded metal atoms [14,15] in graphene pores. An attempt to explain the effects of magnetic impurities in graphene has been given by Kochan *et al.* [16]. They find that 0.36 ppm coverage of hydrogen adatoms is sufficient to obtain spin relaxation times that are in agreement with experiments. Their model is based on the Green's function of a single hydrogen adatom in an infinite graphene sheet and multiplying the results with the impurity concentration. In effect, their model does not include interference effects between scatterers and is thus only valid in the highly dilute limit. Spin transport in hydrogenated graphene was also considered by Soriano *et al.* [17,18]. Their method is based on a mean-field Hubbard Hamiltonian and the real space Kubo-transport formalism. They find that a coverage of 15 ppm hydrogen adatoms gives the correct order of magnitude of the spin relaxation time [18], which is more than an order of magnitude larger than the prediction by Kochan *et al.* Additionally, the energy dependence of the two theoretical predictions for the spin relaxation time do not agree with the experimental findings. A recent *ab initio* study of the spin scattering of hydrogen adatoms on narrow armchair graphene nanoribbons by Wilhelm *et al.* [19] has shown that spin scattering off a single hydrogen adatom with defect spin oriented perpendicular to the electron spin is sufficient to obtain spin-flip conductance on the same order of magnitude as the spin-conserved conductance. They also showed spin-orbit interactions to be negligible compared to exchange interactions in the context of spin scattering on hydrogen adatoms.

The spin relaxation length is determined by the decay rate of spin polarization. Zurek *et al.* [20] have found through a phenomenological spin interaction Hamiltonian that the spin relaxation decay rate depends on the distribution of coupling strengths between a spin system and an environment with many independent spins. In particular, they find that a Gaussian distribution of couplings leads to Gaussian decay of the spin polarization with respect to time, whereas a Lorentzian distribution leads to exponential decay. It is straightforward to demonstrate that the spin relaxation of scatterers on a classical Markovian chain is also exponential. Therefore, the exponential decay of spin polarization is typically referred to as Markovian behavior [21].

In this paper, we calculate the spin-dependent electron transport on graphene with hydrogen adatoms using the Landauer-Büttiker formalism, which is a widely used method for calculating quantum transport in nanoscale devices [19,22–27]. We use hydrogen adatoms as they are very common magnetic defects on graphene. Each defect has a finite magnetic moment of $1\mu_B$. Additionally, due to local sp^3 hybridization, heavily hydrogenated graphene has an energy gap [28]. In particular, we will demonstrate that the Landauer-Büttiker formalism can be used to extract the spin relaxation length of a system. We will demonstrate that the spin relaxation is not always Markovian and that inverse spin relaxation length and sheet resistance scale nearly linearly with impurity concentration.

II. THEORETICAL METHODS

We start by simulating a hydrogen adatom on graphene in a supercell geometry using density-functional theory (DFT) as implemented in the FHI-AIMS package [29]. It is an all-electron code with numerical atom-centered basis functions. We use the default *tight* basis set for each atom type in a spin-polarized calculation. The electron-electron interactions are treated at the level of the Perdew-Burke-Ernzerhof (PBE) exchange-correlation functional [30]. The hydrogen adatom on graphene is relaxed in a supercell with $2 \times 8 \times 8 = 128$ carbon atoms, until the forces between the atoms are smaller than 10^{-3} eV/Å. We expect the supercell to be large enough for finite size effects to be negligible to describe hydrogen adatoms in the dilute limit. Moreover, the DFT self-consistency cycle is considered converged if, among other things, the total energy changes by less than 10^{-6} eV. We use an $8 \times 8 \times 1$ k-point Monkhorst-Pack grid during relaxation. The final band structure and density of states (DOS) calculations use Γ-centered grids of $15 \times 15 \times 1$ k points, whereas the atom-projected partial DOS (PDOS) calculation uses a grid of $12 \times 12 \times 1$ k points.

The DFT band structure, DOS, and PDOS of a system with a hydrogen adatom are shown in Fig. 1. There are spin-polarized impurity bands on both sides of the Fermi energy that also appear as peaks in the total DOS. The occupied impurity band of the majority spin component results in a spin moment of $1.0\mu_B$. The states corresponding to the impurity band, and the resulting spin density thereof, are localized at the hydrogen atom (H) and at the sublattice neighboring the carbon atom (C_0) underneath the hydrogen atom. Other models, such as Ref. [17], remove the H and C_0 atom sites, such that the vacancy in the lattice results in a similar spin density profile.

We fit tight-binding (TB) models to the DFT band structures and PDOS in order to simulate systems with a large number of hydrogen adatoms in the dilute limit. We start with a tight-binding model of graphene, written as

$$\hat{H}_0 = \sum_{i,j} t_{ij} |i\rangle\langle j|, \tag{1}$$

where $|i\rangle$ is a state localized at the lattice site i, and t_{ij} are hopping parameters between the lattice sites. The carbon on-site energy is taken as the energy zero point. We take hoppings up to third-nearest neighbors, and we denote the first-, second- and third-nearest-neighbor hopping elements as t_1, t_2, and t_3, respectively. By fitting to the pristine graphene DFT band structure, we find the C-C hopping parameters $t_1 = -2.855$ eV, $t_2 = -0.185$ eV, and $t_3 = -0.190$ eV. The t_1 and t_2 parameters are fitted freely, and t_3 is included by assuming that $t_3 = t_1(0.18/2.7)$, where the factor is motivated by earlier models [31].

It turns out that the systems with a hydrogen adatom can be accurately described with remarkably simple models, at least in the dilute limit. Namely, we introduce a new site corresponding to the hydrogen adatom (H), and we couple it to the graphene backbone by allowing only a spin-independent hopping t' to the carbon site beneath it (C_0). Moreover, the hydrogen on-site potential is taken as spin dependent with values of $\varepsilon_\uparrow$ and $\varepsilon_\downarrow$ for the majority and minority spin channels, respectively. The model Hamiltonian in the case of a single hydrogen adatom is written as

$$\begin{aligned}\hat{H} = \hat{H}_0 &+ t'(|\mathrm{C}_0\rangle\langle\mathrm{H}| + |\mathrm{H}\rangle\langle\mathrm{C}_0|) \\ &+ |\mathrm{H}\rangle\langle\mathrm{H}| \otimes (\varepsilon_\uparrow |\uparrow_{\mathbf{a}}\rangle\langle\uparrow_{\mathbf{a}}| + \varepsilon_\downarrow |\downarrow_{\mathbf{a}}\rangle\langle\downarrow_{\mathbf{a}}|),\end{aligned} \tag{2}$$

where the spin-independent parts are shortened as $\hat{H}_0 \otimes \mathbb{1} = \hat{H}_0$, and $|\uparrow_{\mathbf{a}}\rangle$ and $|\downarrow_{\mathbf{a}}\rangle$ are the orthogonal spin basis vectors along the spin-quantization axis $\mathbf{a} = (\sin\theta\cos\phi, \sin\theta\sin\phi, \cos\theta)$, such that $|\uparrow_{\mathbf{a}}\rangle = \cos(\theta/2)|\uparrow\rangle + e^{i\phi}\sin(\theta/2)|\downarrow\rangle$ and $|\downarrow_{\mathbf{a}}\rangle = e^{-i\phi}\sin(\theta/2)|\uparrow\rangle - \cos(\theta/2)|\downarrow\rangle$, where we have used the shorthand notation $|\uparrow\rangle = |\uparrow_{\hat{\mathbf{z}}}\rangle$ and $|\downarrow\rangle = |\downarrow_{\hat{\mathbf{z}}}\rangle$. The spin-quantization axis for the charge carriers is chosen to be $\hat{\mathbf{z}}$ in all calculations.

We fit the tight-binding model to the DFT band structure and PDOS. Specifically, we compare the six lowest unoccupied and six highest occupied bands, and fit the two-dimensional band energies in the first Brillouin zone. The DFT PDOS is fitted to the TB local DOS (LDOS) in the defect neighborhood up to the fourth-nearest carbon atoms surrounding the hydrogen adatom. We find that the C-H hopping is $t' = 9.475$ eV, and the hydrogen on-site potentials have values $\varepsilon_\uparrow = 1.853$ eV for the majority spin component and $\varepsilon_\downarrow = 4.689$ eV for the minority spin component. The fitted TB band structure, total DOS, and LDOS are shown in Fig. 1, where they are compared to the DFT calculations. The figure shows excellent agreement between the TB model and the DFT results. One should note that the model parameters depend slightly on the number of energy bands and PDOS atoms, and the corresponding weights for these in the cost function, but this will only have a marginal effect on the obtained results.

We consider the quantization axis of the defect spin moments as classical vectors that can be rotated individually, and eventually ensemble average results over different rotation angles and defect position realizations. To do this, we write the spin-dependent part of the model Hamiltonian, Eq. (2), as

$$\varepsilon_\uparrow |\uparrow_{\mathbf{a}}\rangle\langle\uparrow_{\mathbf{a}}| + \varepsilon_\downarrow |\downarrow_{\mathbf{a}}\rangle\langle\downarrow_{\mathbf{a}}| = \frac{\varepsilon_\uparrow + \varepsilon_\downarrow}{2}\mathbb{1} + \frac{\varepsilon_\uparrow - \varepsilon_\downarrow}{2}\hat{\sigma}_{\mathbf{a}}, \tag{3}$$

where $\mathbb{1} = |\uparrow_{\mathbf{a}}\rangle\langle\uparrow_{\mathbf{a}}| + |\downarrow_{\mathbf{a}}\rangle\langle\downarrow_{\mathbf{a}}|$ is the identity matrix and $\hat{\sigma}_{\mathbf{a}} = |\uparrow_{\mathbf{a}}\rangle\langle\uparrow_{\mathbf{a}}| - |\downarrow_{\mathbf{a}}\rangle\langle\downarrow_{\mathbf{a}}|$ is the Pauli z matrix in the given basis. For each defect, we define the rotation angles θ and ϕ on the Bloch sphere. As the only spin-dependent parameter is the hydrogen on-site potential, spin flipping only occurs at these sites when the charge carrier spin is not aligned with the defect spin. In the $\{|\uparrow\rangle, |\downarrow\rangle\}$ basis, $\hat{\sigma}_{\mathbf{a}}$ is given by

$$\begin{aligned}\hat{\sigma}_{\mathbf{a}} = &\cos\theta|\uparrow\rangle\langle\uparrow| - \cos\theta|\downarrow\rangle\langle\downarrow| \\ &+ e^{-i\phi}\sin\theta|\uparrow\rangle\langle\downarrow| + e^{i\phi}\sin\theta|\downarrow\rangle\langle\uparrow|.\end{aligned} \tag{4}$$

The rotation of the defect spins is similar to the method used in Ref. [19], except that we rotate each defect spin individually. The reasons why we do this are the following: In the dilute limit, the interactions between the defects can be assumed small. Then a finite temperature or other environmental factors, e.g., local Zeeman terms originating from the graphene curvature or substrate, can break the magnetic ordering in a system with many hydrogen adatoms. In such a case, we cannot choose the same spin basis simultaneously for all the defect spin moments. Instead, the defect spin moments can be at least partly uncorrelated, pointing to somewhat random directions. On the other hand, in the limit of many

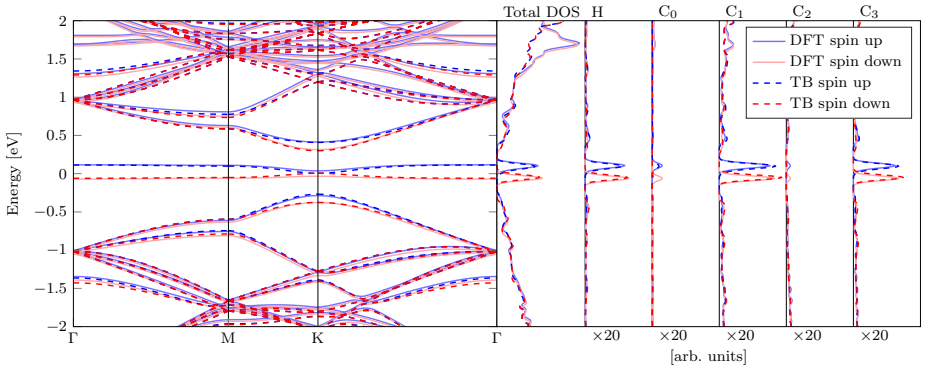

FIG. 1. (Color online) Spin-polarized band structure, total DOS, and PDOS of an 8×8 supercell with a hydrogen adatom for both the majority and minority spin components. The DFT PDOS is compared to the TB LDOS at the hydrogen atom (H), the carbon atom underneath the hydrogen atom (C_0), and its first-, second-, and third-nearest neighbors C_1, C_2, and C_3, respectively.

nearby defects, frustration can result in a nontrivial defect spin moment configuration that can be difficult to estimate without explicitly including the defect spin-spin interactions.

The transmittance between any two leads p and q of a multiterminal system can be calculated using the Landauer-Büttiker formula [24] $T_{pq} = \mathrm{Tr}\{\Gamma_p G \Gamma_q G^\dagger\}$, where $G = [(E + i\varepsilon)I - H - \sum_n \Sigma_n]^{-1}$ is the retarded Green's function. Σ_n and Γ_n are the self-energy and linewidth functions, respectively, of lead n. The leads are modeled here as pristine graphene ribbons with the same unit cell width as the device region and the electronic transport is in the zigzag direction (see Fig. 2). A small imaginary part $\varepsilon = 10^{-5}$ eV is added to the energy for numerical stability. If the spins are decoupled in the leads, it is easy to demonstrate that the spin-channel resolved transmittance between the leads of a spin-dependent two-terminal system becomes [19,32]

$$T_{\sigma,\sigma'} = \mathrm{Tr}\left\{\Gamma_\sigma^{(L)} G \Gamma_{\sigma'}^{(R)} G^\dagger\right\}, \tag{5}$$

where $\Gamma_\sigma^{(L)}$ ($\Gamma_{\sigma'}^{(R)}$) is the linewidth function of the left (right) lead with spin σ (σ'). The transmittance on this form can be computed efficiently using the recursive Green's functions (RGF) technique (as outlined in Refs. [25,33]). All calculations are performed on unit cells with a relatively large width of 12.8 nm in order to minimize finite size effects. Furthermore, the calculations are performed using periodic boundary conditions transverse to the transport direction and the results are averaged over 29 k points. Exactly at the charge neutrality point (CNP), the only propagating mode in the leads is at $k = 0$ and it is therefore important to ensure that this is included.

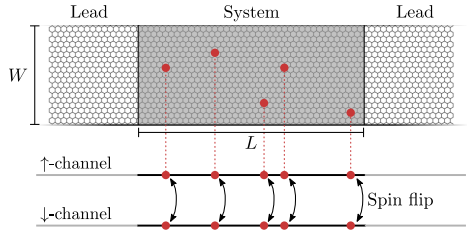

FIG. 2. (Color online) Unit cell of width W and length L as used in the simulations. The unit cell is repeated periodically transverse to the leads. The spin-dependent transport is equivalent to having two separate channels that couple only at magnetic impurity sites.

The spin-conserved transport is defined as $T_{sc} = T_{\uparrow\uparrow} + T_{\downarrow\downarrow}$ and the spin-flipped transport is defined as $T_{sf} = T_{\uparrow\downarrow} + T_{\downarrow\uparrow}$. We expect the total transport $T = T_{sc} + T_{sf}$ to be either Ohmic or localized. For Ohmic transport the resistance per unit cell is $R(L) = R_c + R_s L/W$, where R_c is the contact resistance, R_s is the sheet resistance, L is the device length, and W is the width of the unit cell. In the localization regime, the resistance is $R(L) = R_c \exp(L/\xi)$, where ξ is the localization length. By fitting the total transport to a compound expression

$$R(L) = \frac{h}{2e^2 T} = R_c \exp(L/\xi) + R_s L/W, \tag{6}$$

we obtain both localization length and Ohmic resistance. In the limits $\xi \to \infty$ and $R_s \to 0$, this expression reduces to the Ohmic and localization regimes, respectively.

We can use the spin polarization P to obtain the spin relaxation length λ_S. According to Zurek *et al.* [20], the spin relaxation mechanism can be either exponential or Gaussian, depending on the distribution of spin couplings to an environment. In order to include both cases as well as any intermediate relaxation mechanism, we fit the output spin polarization of a device with length L according to the following expression,

$$P(L) = \frac{T_{sc}(L) - T_{sf}(L)}{T_{sc}(L) + T_{sf}(L)} = e^{-(L/\lambda_S)^n}. \tag{7}$$

It follows that the spin relaxation behavior is exponential when $n = 1$ and Gaussian when $n = 2$.

III. RESULTS

The output spin polarization of a system containing a single H adatom is shown in Fig. 3. When there is only a single defect, the transport properties do not depend on

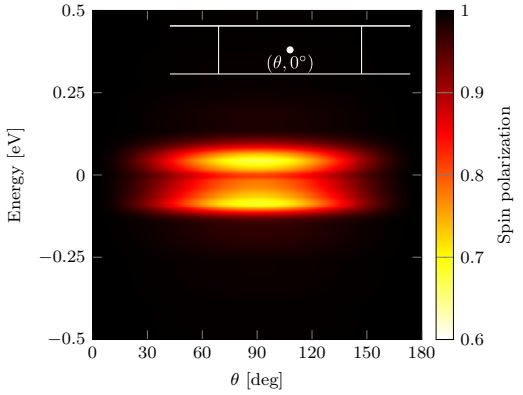

FIG. 3. (Color online) Spin polarization as a function of energy and angle of a graphene system with a single H adatom. The inset shows an illustration of the device.

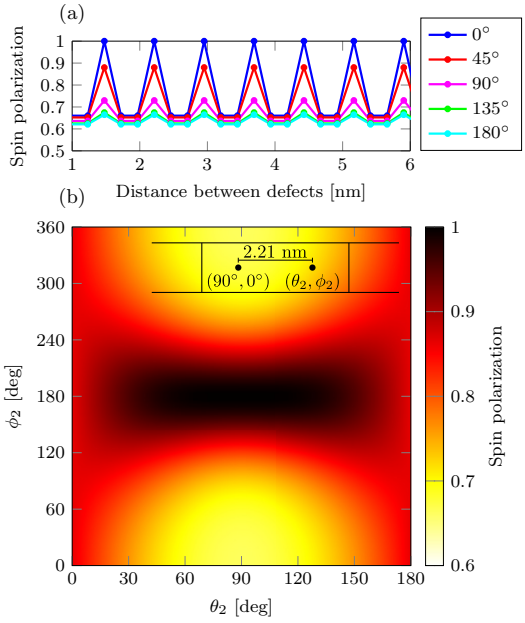

FIG. 4. (Color online) Spin polarization of a system with two H adatoms at an energy of $E = 0.0$ eV. The H adatoms are placed on a line parallel to the transport direction and the defect spin angles are $(\theta_1,\phi_1) = (90^\circ,0^\circ)$ and (θ_2,ϕ_2), respectfully. (a) The distance between the defect is varied and θ_2 has been fixed to 90°. (b) The defects are placed 2.21 nm apart.

the azimuthal defect spin angle ϕ. Therefore, only the polar angle θ and the energy E are varied. The figure shows that the spin scatters very strongly near the CNP, $E \simeq 0$, resulting in a significantly decreased spin polarization. This is a consequence of scattering on H adatoms, which have defect bands that span approximately ± 0.1 eV around the CNP (cf. Fig. 1). This means that a single H adatom with defect spin perpendicular to the charge carrier spin is able to destroy almost half of the spin polarization for energies near the CNP. This is in good agreement with Wilhelm *et al.* [19], who found that an $N = 11$ armchair graphene nanoribbon with a single H adatom can have spin-flip transmittance that can surpass the spin-conserved part.

In order to obtain information on the interference effects on spin flipping, we calculate the output spin polarization of a system with two H adatoms separated by a distance of 2.21 nm parallel to the transport direction [see Fig. 4(b)]. The output spin polarization is evaluated at the CNP and the orientations of the defect spins have been chosen to be $(\theta_1,\phi_1) = (90^\circ,0^\circ)$ and (θ_2,ϕ_2), respectively. The figure shows that the output spin polarization is minimal when the defect spins are perpendicular to the charge carrier spin and point in the same direction, whereas it is maximal, when the spins are perpendicular to the charge carrier spin and point in opposite directions. In Fig. 3, we saw that a single defect with spin perpendicular to the charge carrier spin could flip almost half of the electron spin to the opposite channel. Now we see that by having two defects with oppositely oriented spins, the second can almost completely negate the first spin flip. When the two defect spins point in opposite directions, the phase change associated with spin flipping will have equal size and opposite sign. This means that the electron spin will be in phase with the charge carrier spin after the second spin flip, leading to constructive interference. This is not necessarily the case when the defect spins point in the same direction. The interference between defects is thus very important and should not be ignored. Furthermore, the spin-scattering strength depends strongly on the relative position of the two defects, which is illustrated in Fig. 4(a), where the spin polarization is calculated as a function of distance between them. The figure shows that at the CNP, the output spin polarization is periodic with the distance between them with a period of three graphene lattice constants. Presumably, the periodicity arises due to the same quantization phenomenon that causes every third armchair graphene nanoribbon to be metallic, and the remaining nanoribbons to be semiconducting.

We now turn to calculating the effects of multiple magnetic hydrogen adatoms on graphene. We place hydrogen adatoms at random positions uniformly distributed across the device according to a predefined impurity concentration η. We wish to keep the device nonmagnetic in order to isolate spin relaxation from other magnetic effects. Therefore, we choose the directions of the defect spins at random, uniformly distributed on a Bloch sphere. The transport is calculated for very long devices of 147.5 nm, which contain a total of 72 000 carbon atoms in the unit cell. Using the RGF method, we can extract the transport after each slice of the device, allowing us to obtain the transport results for all device lengths until the chosen maximum length. In order to minimize the effects of the finite width of the unit cell, we average over an ensemble of 150 device realizations. The spin polarization as a function of device length and energy for different impurity concentrations is shown in Fig. 5 as well as an example of transmittance and spin polarization as a function of device

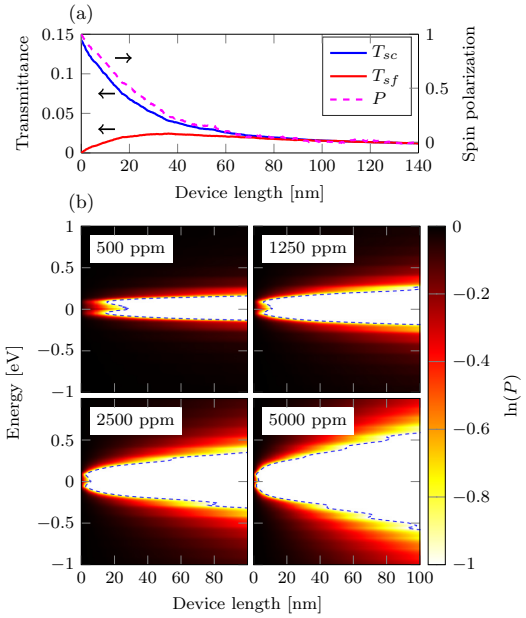

FIG. 5. (Color online) (a) Ensemble-averaged transmittance and spin polarization as a function of device length for a system with impurity concentration $\eta = 500$ ppm calculated at the CNP. (b) Ensemble-averaged spin polarization as a function of energy and device length for different impurity concentrations. The dashed lines show the spin relaxation length.

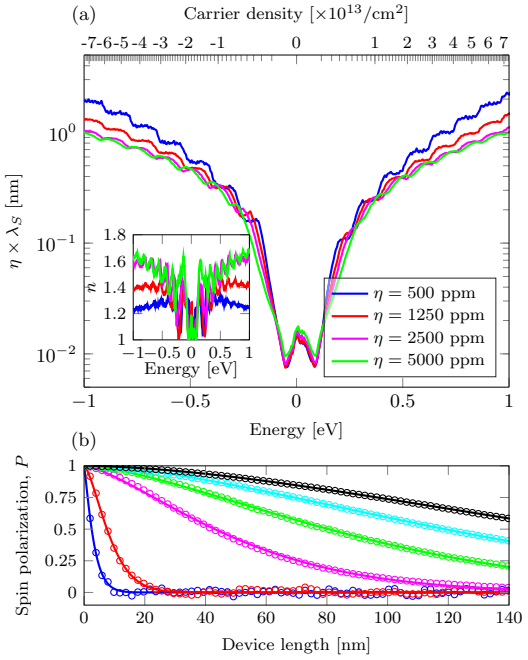

FIG. 6. (Color online) (a) Normalized spin relaxation length $\eta \times \lambda_S$ and exponent n (inset) obtained by fitting against Eq. (7). The spin relaxation lengths are normalized with the defect concentration in order to illustrate that their inverse scale nearly linearly with respect to it. (b) Examples of fitting the spin relaxation against Eq. (7) of a system with 5000 ppm H adatoms for different energies. The energies are between 0.0 eV (fastest decay) and 1.0 eV (slowest decay) in steps of 0.2 eV. The circles are the ensemble averaged spin polarizations and the lines are the corresponding fitted functions. For visualization purposes, only every fourth data point is shown.

length for a single energy and impurity concentration. We show the logarithm of the spin polarization in the range between -1 and 0 in order to highlight the spin relaxation length, which is defined as the device length at which $\ln[P(L)] = -1$. The figure shows that the spin polarization decays very fast for energies close to the H adatom defect bands (cf. Fig. 1). As expected, the spin polarization decays faster with increasing impurity concentration. Note that the spin polarization also decays for energies away from the H defect bands, due to the relatively small, but finite, spin splitting in the remaining band structure. The small energy-dependent oscillations in Figs. 5 and 6 are due to finite size effects originating from the finite width of the unit cell.

Equation (7) with two fitted parameters captures the simulated spin polarization as a function of device length very accurately. The fitted parameters are the spin relaxation length λ_S as well as the exponent n, which provides information on the spin relaxation mechanism [see Fig. 6(a)]. A few examples of the fitting procedure are included in Fig. 6(b) in order to illustrate the excellent quality of the fits. The carrier concentration in the figure is computed at Fermi energies corresponding to the energy axis. Positive and negative carrier densities refer to electron and hole doping, respectively. The spin relaxation length is very short for energies near the H defect bands. For the same energies, the spin relaxation mechanism is predominantly exponential with an exponent of $n \simeq 1$. For energies further away from the CNP, the spin relaxation length increases. We note that λ_S has two minima near the CNP, which are correlated with the large spin splitting of the H adatom defect bands. Exactly at the CNP, the spin splitting of the defect bands is vanishing, resulting in a local maxima. The figure shows that there is an almost linear scaling of the inverse spin relaxation length λ_S^{-1} with respect to impurity concentration η, especially near the CNP. Away from the CNP we observe that n decreases with decreasing impurity concentration. This suggests that the spin relaxation mechanism tends toward exponential (Markovian) behavior in the highly dilute impurity limit. Importantly, we see that the decay of the spin polarization as a function of device length need not be exponential nor Gaussian, which means that a more complete theory on spin relaxation should not presume anything about the spin relaxation behavior, except in the limit of very dilute systems, where the approximation of exponential decay seems to be valid. For energies near the CNP, the normalized localization length is $\eta \times \lambda_S \approx 0.01$ nm. In order to obtain experimentally observed spin relaxation length of about $\lambda_S \simeq 2\ \mu$m [3], the impurity concentration should be

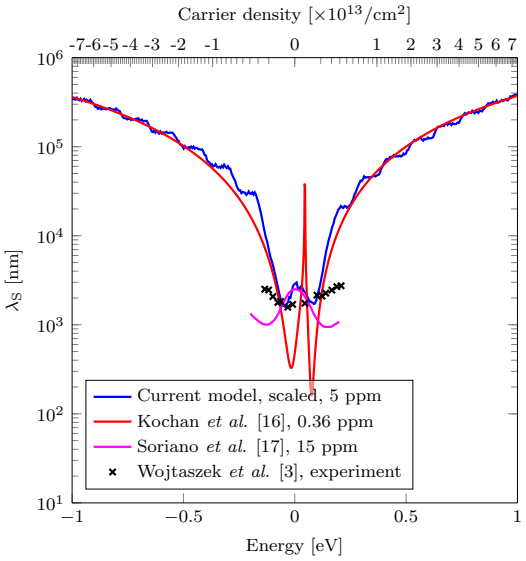

FIG. 7. (Color online) Comparison of spin relaxation lengths obtained by different authors.

$\eta \approx 5$ ppm, which is more than an order of magnitude larger than the prediction by Kochan *et al.* [16] of 0.36 ppm. We expect our model to be more accurate as it is based on a full transport calculation and therefore takes interference effects into account. Our prediction of the impurity concentration is, however, in closer agreement with Soriano *et al.* [18], who found that an impurity concentration of 15 ppm gives spin relaxation times in agreement with an experiment based on time propagation of the spin polarization operator using a self-consistent Hubbard model.

A comparison of spin relaxation lengths obtained by the current model and those obtained by other theoretical methods and experiments is presented in Fig. 7. We have scaled our 500 ppm result to 5 ppm by multiplying it by a factor of 100. The two other theoretical methods [16,17] give the spin relaxation time τ_S, which is related to the spin relaxation length by $\lambda_S = v_S\tau_S$ in the ballistic regime and by $\lambda_S = \sqrt{D_S\tau_S}$ in the diffusive regime, where v_S is spin carrier velocity and and D_S is the spin diffusion constant. In the low-defect-density case, we expect to be in the ballistic regime. Therefore, we compare results that are all obtained in the low-defect-density case. We obtain a velocity $v_S = 1.65 \times 10^4$ m/s by a least squares fitting between our result and the analytic result obtained by Kochan *et al.* [16]. We observe that the result by Kochan *et al.* is in fairly good agreement with ours regarding the location of the two minima near the CNP and in quantitative agreement further away from the CNP. However, their result predicts variations over several orders of magnitude near the CNP, whereas our result predicts a variation of only about a factor of 2. In fact, their result is singular exactly at the CNP, because it is neither broadened by the self-energy due to leads or by finite geometry effects.

Furthermore, we compare with the experimental results of hydrogenated graphene obtained by Wojtaszek *et al.* [3]. Note that the experimental results were obtained without detailed knowledge of the defect concentration. However, the authors estimated the concentration to be around 200 ppm. Lastly, we compare our results to the theoretical result by Soriano *et al.* [17]. The figure shows that their result is neither in qualitative agreement with our model nor the analytic result by Kochan *et al.* or experiment. We speculate that the deviation arises from the fact that Soriano *et al.* uses vacancies in graphene to model hydrogen adatoms, whereas both our model and the model used by Kochan *et al.* employ a parametrization of hydrogen on graphene. Theoretical predictions [16,18,34], including our own, show that the spin relaxation time (or spin relaxation length) decreases with increasing impurity concentration. However, experimental work on hydrogenated graphene shows that the spin relaxation time (or spin relaxation length) actually increases with increasing impurity concentration [3]. The origin of this discrepancy remains elusive, but could stem from interactions between graphene and the substrate, as this has not been included in any of the theoretical models. Another possibility is that the hydrogen plasma used in the experiments was additionally cleaning the graphene surface, thus increasing the spin relaxation time. Finally, a recent paper by Idzuchi *et al.* [35] discusses the possibility that details of the Hanle measurements were not taken into account in the data analysis.

By fitting the total transmittance against Eq. (6) we obtain the Ohmic sheet resistance as well as the localization length

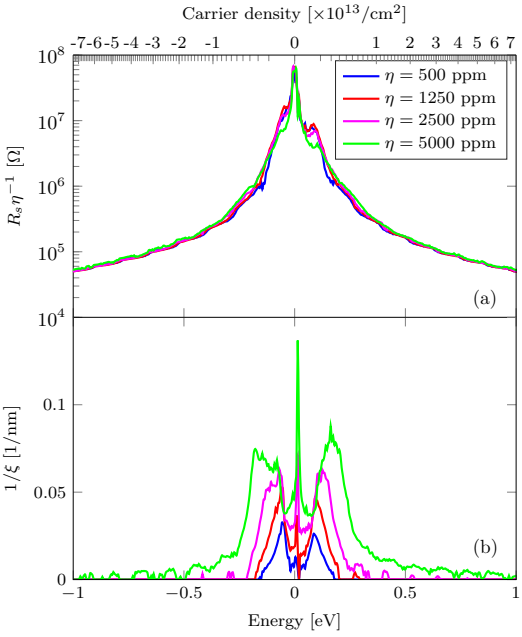

FIG. 8. (Color online) (a) Normalized Ohmic sheet resistance R_s/η and (b) inverse localization length $1/\xi$ obtained by fitting against Eq. (6).

(see Fig. 8). We observe localization near the H defect bands (cf. Fig. 1) and vanishing localization elsewhere. Additionally, the figure shows that the sheet resistance scales linearly with respect to impurity concentration. However, the scaling of the localization length is far from linear, which shows that the induced localization per atom decreases with increasing impurity concentration. Furthermore, as the impurity concentration is decreased, the energy window at which there is localization, narrows.

IV. CONCLUSIONS

In this work, we study spin-dependent transport of hydrogenated graphene. We use a simple model with only a spin-dependent on-site potential at the defect site to describe hydrogen adatoms on graphene. As the model is simple, some of the results are expected to extend qualitatively to other systems as well. We have demonstrated that the Landauer-Büttiker formalism can be used to calculate spin-dependent transport of systems with magnetic impurities with individually oriented magnetic moments. In this work, we study hydrogen adatoms on graphene. By calculating the spin-dependent transport as a function of device length, we can extract properties such as spin relaxation length, localization length, and sheet resistance. We have shown that there is strong localization for energies around the hydrogen-induced defect bands, which also lead to a very high sheet resistance. Away from the defect bands there is vanishing localization. Furthermore, we have demonstrated that the spin relaxation length is very short for energies around the hydrogen-induced defect bands and that the spin relaxation mechanism is exponential (Markovian) near the CNP and nonexponential (non-Markovian) otherwise. Additionally, we have shown that the inverse spin relaxation length and sheet resistance scale nearly linearly with impurity concentration, whereas the localization length does not.

ACKNOWLEDGMENTS

M.R.T. and T.G.P. gratefully acknowledge the financial support from the Center for Nanostructured Graphene (Project No. DNRF58) financed by the Danish National Research Foundation and from the QUSCOPE project financed by the Villum Foundation. The work by A.H. and M.M.E. has been supported by the Academy of Finland through its Centres of Excellence Program (Project No. 251748). We acknowledge the computational resources provided by Aalto Science-IT project and Finland's IT Center for Science (CSC). M.M.E. acknowledges financial support from the Finnish Cultural Foundation.

[1] D. Huertas-Hernando, F. Guinea, and A. Brataas, Phys. Rev. Lett. **103**, 146801 (2009).
[2] W. Han, R. K. Kawakami, M. Gmitra, and J. Fabian, Nat. Nanotechnol. **9**, 794 (2014).
[3] M. Wojtaszek, I. J. Vera-Marun, T. Maassen, and B. J. van Wees, Phys. Rev. B **87**, 081402 (2013).
[4] N. Tombros, S. Tanabe, A. Veligura, C. Jozsa, M. Popinciuc, H. T. Jonkman, and B. J. van Wees, Phys. Rev. Lett. **101**, 046601 (2008).
[5] N. Tombros, C. Jozsa, M. Popinciuc, H. T. Jonkman, and B. J. van Wees, Nature (London) **448**, 571 (2007).
[6] W. Han and R. K. Kawakami, Phys. Rev. Lett. **107**, 047207 (2011).
[7] M. Wojtaszek, I. J. Vera-Marun, E. Whiteway, M. Hilke, and B. J. van Wees, Phys. Rev. B **89**, 035417 (2014).
[8] P. J. Zomer, M. H. D. Guimaraes, N. Tombros, and B. J. van Wees, Phys. Rev. B **86**, 161416 (2012).
[9] B. Dlubak, M.-B. Martin, C. Deranlot, B. Servet, S. Xavier, R. Mattana, M. Sprinkle, C. Berger, W. A. De Heer, F. Petroff, A. Anane, P. Seneor, and A. Fert, Nat. Phys. **8**, 557 (2012).
[10] M. H. D. Guimarães, P. J. Zomer, J. Ingla-Aynés, J. C. Brant, N. Tombros, and B. J. van Wees, Phys. Rev. Lett. **113**, 086602 (2014).
[11] S. Lara-Avila, S. Kubatkin, O. Kashuba, J. A. Folk, S. Lüscher, R. Yakimova, T. J. B. M. Janssen, A. Tzalenchuk, and V. Fal'ko, Phys. Rev. Lett. **115**, 106602 (2015).
[12] O. V. Yazyev and L. Helm, Phys. Rev. B **75**, 125408 (2007).
[13] Y. Ma, P. O. Lehtinen, A. S. Foster, and R. M. Nieminen, New J. Phys. **6**, 68 (2004).
[14] A. V. Krasheninnikov, P. O. Lehtinen, A. S. Foster, P. Pyykkö, and R. M. Nieminen, Phys. Rev. Lett. **102**, 126807 (2009).
[15] M. R. Thomsen, S. J. Brun, and T. G. Pedersen, Phys. Rev. B **91**, 125439 (2015).
[16] D. Kochan, M. Gmitra, and J. Fabian, Phys. Rev. Lett. **112**, 116602 (2014).
[17] D. Soriano, N. Leconte, P. Ordejón, J.-C. Charlier, J.-J. Palacios, and S. Roche, Phys. Rev. Lett. **107**, 016602 (2011).
[18] D. Soriano, D. Van Tuan, S. M. Dubois, M. Gmitra, A. W. Cummings, D. Kochan, F. Ortmann, J.-C. Charlier, J. Fabian, and S. Roche, 2D Mater. **2**, 022002 (2015).
[19] J. Wilhelm, M. Walz, and F. Evers, Phys. Rev. B **92**, 014405 (2015).
[20] W. H. Zurek, F. M. Cucchietti, and J. P. Paz, Acta Phys. Pol., B **38**, 1685 (2007).
[21] W. A. Coish, J. Fischer, and D. Loss, Phys. Rev. B **77**, 125329 (2008).
[22] S. R. Power and A.-P. Jauho, Phys. Rev. B **90**, 115408 (2014).
[23] M. R. Thomsen, S. J. Brun, and T. G. Pedersen, J. Phys.: Condens. Matter **26**, 335301 (2014).
[24] S. Datta, *Electronic Transport in Mesoscopic Systems* (Cambridge University Press, Cambridge, UK, 1995).
[25] T. Markussen, R. Rurali, M. Brandbyge, and A.-P. Jauho, Phys. Rev. B **74**, 245313 (2006).
[26] T. G. Pedersen and J. G. Pedersen, J. Appl. Phys. **112**, 113715 (2012).
[27] J. G. Pedersen, T. Gunst, T. Markussen, and T. G. Pedersen, Phys. Rev. B **86**, 245410 (2012).
[28] R. Balog, B. Jørgensen, L. Nilsson, M. Andersen, E. Rienks, M. Bianchi, M. Fanetti, E. Lægsgaard, A. Baraldi, S. Lizzit, Z. Sljivancanin, F. Besenbacher, B. Hammer, T. G. Pedersen, P. Hofman, and L. Hornekær, Nat. Mater. **9**, 315 (2010).

[29] V. Blum, R. Gehrke, F. Hanke, P. Havu, V. Havu, X. Ren, K. Reuter, and M. Scheffler, Comput. Phys. Commun. **180**, 2175 (2009).
[30] J. P. Perdew, K. Burke, and M. Ernzerhof, Phys. Rev. Lett. **77**, 3865 (1996).
[31] Y. Hancock, A. Uppstu, K. Saloriutta, A. Harju, and M. J. Puska, Phys. Rev. B **81**, 245402 (2010).
[32] T. P. Pareek and P. Bruno, Phys. Rev. B **65**, 241305 (2002).
[33] A. MacKinnon, Z. Phys. B **59**, 385 (1985).
[34] D. Van Tuan, F. Ortmann, D. Soriano, S. O. Valenzuela, and S. Roche, Nat. Phys. **10**, 857 (2014).
[35] H. Idzuchi, A. Fert, and Y. Otani, Phys. Rev. B **91**, 241407 (2015).

Publication V

Magnetic edge states and magnetotransport in graphene antidot barriers

Morten Rishøj Thomsen, Stephen Robert Power, Antti-Pekka Jauho and Thomas Garm Pedersen

The paper has been published in
Physical Review B **92**, 045438 (2016).

Magnetic edge states and magnetotransport in graphene antidot barriers

M. R. Thomsen,[1,2] S. R. Power,[2,3] A.-P. Jauho,[3] and T. G. Pedersen[1,2]

[1]*Department of Physics and Nanotechnology, Aalborg University, DK-9220 Aalborg Øst, Denmark*

[2]*Center for Nanostructured Graphene (CNG), DK-9220 Aalborg Øst, Denmark*

[3]*Center for Nanostructured Graphene (CNG), DTU Nanotech, Department of Micro- and Nanotechnology, Technical University of Denmark, DK-2800 Kongens Lyngby, Denmark*

(Received 13 May 2016; published 28 July 2016)

Magnetic fields are often used for characterizing transport in nanoscale materials. Recent magnetotransport experiments have demonstrated that ballistic transport is possible in graphene antidot lattices (GALs). These experiments have inspired the present theoretical study of GALs in a perpendicular magnetic field. We calculate magnetotransport through graphene antidot barriers (GABs), which are finite rows of antidots arranged periodically in a pristine graphene sheet, using a tight-binding model and the Landauer-Büttiker formula. We show that GABs behave as ideal Dirac mass barriers for antidots smaller than the magnetic length and demonstrate the presence of magnetic edge states, which are localized states on the periphery of the antidots due to successive reflections on the antidot edge in the presence of a magnetic field. We show that these states are robust against variations in lattice configuration and antidot edge chirality. Moreover, we calculate the transmittance of disordered GABs and find that magnetic edge states survive a moderate degree of disorder. Due to the long phase-coherence length in graphene and the robustness of these states, we expect magnetic edge states to be observable in experiments as well.

DOI: 10.1103/PhysRevB.94.045438

I. INTRODUCTION

Graphene antidot lattices (GALs), which are periodic perforations in a graphene sheet, may open a band gap in the otherwise semimetallic material [1–7]. An advantage of GALs is that the size of the band gap can be tuned by geometrical factors. Recent magnetotransport experiments have demonstrated that ballistic transport is possible in GALs [8,9], which gives rise to interesting phenomena such as magnetoresistance oscillations due to cyclotron orbits that are commensurate with the antidot lattice. Ballistic transport in pristine graphene has been demonstrated several times and even at room temperature [10–15], but ballistic transport in GALs has previously been hindered by defects introduced by top-down fabrication of the antidots. The recent demonstrations [8,9] of ballistic transport in GALs were achieved by minimizing interaction with the substrate by using hexagonal boron nitride (hBN) substrates and by reducing edge roughness by encapsulating the graphene flake in hBN before etching the antidot lattice [8].

Previous theoretical studies on nanostructured graphene in magnetic fields have primarily focused on the density of states and optical properties [16–19]. The density of states of a structure under a magnetic field reveals a self-similar structure known as Hofstadter's butterfly [20]. In particular, Hofstadter butterflies of GALs have revealed band-gap quenching induced by perpendicular magnetic fields [16]. Transport calculations have yet to reveal if band-gap quenching also gives rise to quenching of the transport gap. Using the Dirac approximation, perforations in a graphene sheet are modeled as local mass terms rather than potentials [7]. Within this description, it has been demonstrated that a single graphene antidot supports localized edge states in the presence of magnetic fields [19]. Conceptually, one may think of these as edge states due to repeated reflections of electrons on the antidot edge provided the radius of the cyclotron motions is small compared to the antidot radius. We will refer to these as "magnetic edge states," not to be confused with spin-polarized edge states, such as those observed on extended zigzag edges [21]. Hence, by such states, we simply mean states that are localized near an antidot due to the magnetic field.

Magnetic edge states occur when the electron wave interferes constructively with itself in a pinned orbit around the antidot, which gives rise to Aharonov-Bohm-type oscillations. In conventional semiconductors, such as GaAs, Aharonov-Bohm oscillations due to antidots in two-dimensional electron gases have been studied theoretically [22–24] and observed experimentally [25–27]. Additionally, a theoretical study predicts the presence of Aharonov-Bohm-type oscillations in graphene nanorings [28]. We likewise predict magnetic edge states to be present in GALs and due to the long phase-coherence length in graphene, we expect these to be observable in experiments as well. Cyclotron orbits were recently imaged in pristine graphene using cooled scanning probe microscopy [29,30]. It would be remarkable if this technique could be used for direct observation of magnetic edge states in graphene antidots.

In the present work, we study the transport properties of graphene antidot barriers (GABs), i.e., finite rows of antidots in an otherwise pristine graphene sheet, in the presence of perpendicular magnetic fields. In our transport calculations, we use the Landauer-Büttiker formalism with a tight-binding model, which is widely used for calculating the quantum transport in nanoscale devices [31–39]. The magnetic field is included in the Hamiltonian by a Peierls substitution. The calculations utilize the recursive Green's function (RGF) method, which greatly reduces the calculation time, while retaining accuracy. Furthermore, we compare the tight-binding results to both an ideal Dirac mass barrier and a gapped graphene model. We find that Dirac mass barriers provide a good description of the transport gap for GABs with small antidots provided the magnetic field is not too strong. Furthermore, we find evidence of magnetic edge states on the antidots and demonstrate simple

scaling of these, allowing predictions for larger systems. Finally, we calculate the transmittance of disordered GABs and compare this to the corresponding transmittance in ordered GABs.

II. THEORY AND METHODS

A. Tight-binding model

In this section, we will use the RGF method with a tight-binding model in order to calculate transmittance of electrons through GABs in a magnetic field. The barrier regions are periodic perpendicular (y direction) to the transport direction (x direction). We also calculate the density of states (DOS) of fully periodic GALs and compare these to the transmittance of GABs.

In the nearest-neighbor orthogonal tight-binding model, the Hamiltonian can be written as

$$\hat{H} = \sum_{i<j} t_{ij}\hat{c}_i^\dagger \hat{c}_j + \text{H.c.}, \tag{1}$$

where the hopping parameter t_{ij} is taken as $-\gamma$ for nearest neighbors and vanishing otherwise. The magnetic field is included by performing the Peierls substitution $t_{ij} \to t_{ij}e^{i\phi_{ij}}$, where $\phi_{ij} = (e/\hbar)\int_{\mathbf{r}_i}^{\mathbf{r}_j} \mathbf{A}\cdot d\mathbf{l}$ is the Peierls phase, $\mathbf{A}$ is the vector potential, and $\mathbf{r}_i$ is the position of atom i. The magnetic field in the leads is taken to zero, which means the vector potential in the Landau gauge is given by

$$\mathbf{A}(\mathbf{r}) = \hat{\mathbf{y}}B\bar{x}, \quad \bar{x} = \begin{cases} 0, & x < 0 \\ x, & 0 \leqslant x \leqslant d \\ d, & x > d, \end{cases} \tag{2}$$

where d is the width of the barrier; see Fig. 1. Note that the vector potential cannot be set to zero in the $x > d$ region, as this would imply an infinite magnetic field at the $x = d$ interface. In this gauge, the Peierls phase becomes

$$\phi_{ij} = \frac{eB}{2\hbar}(y_j - y_i)(\bar{x}_i + \bar{x}_j). \tag{3}$$

We present calculations for triangular, rotated triangular, rectangular, and honeycomb GALs in the notation of Ref. [2]. We will use hexagonal antidots with armchair edges and denote the antidot lattices by $\{L,S\}$, where L and S are the side lengths, in units of the graphene lattice constant $a = 0.246$ Å, of the GAL unit cell and the antidot, respectively; see Fig. 1. For rectangular lattices, we use L_x and L_y to denote the side lengths in the x and y directions, respectively. In our calculations, we chose $L_y \approx L_x = L$ in order for the unit cell to be approximately square. Unless stated otherwise, calculations are made on triangular GABs and assume periodic boundary conditions along the y direction. Calculations on GALs also assume periodic boundary conditions along the x direction and the results are k averaged in the periodic directions. The number of k points in each direction is taken as the odd integer closest to $400/L$.

We also perform calculations on a gapped graphene model where, instead of introducing antidots, a band gap is opened by using a staggered sublattice potential of Δ on one sublattice and $-\Delta$ on the other, opening a band gap of $E_g = 2\Delta$ [40]. The advantage of this method compared to using the actual antidot geometry is that it is computationally much faster due to the reduced width of the unit cell in the y direction.

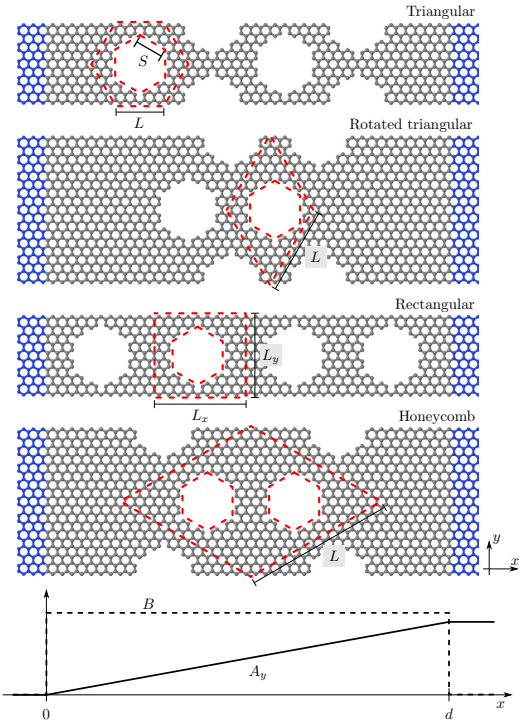

FIG. 1. GAB unit cells used in transport calculations and corresponding vector potential and magnetic field. The unit cells shown here all have four rows of antidots in the transport direction, the same antidot size, and similar neck widths. The gray and blue atoms represent the system and semi-infinite leads, respectively. The dashed red lines outline the corresponding GAL unit cells.

We use the RGF method to extract properties such as transmittance and DOS. This method has the same accuracy as direct diagonalization, but is considerably faster. The method is outlined in Refs. [41,42] and relies on calculating certain block elements of the retarded Green's function $G = [(E + i\varepsilon)I - H - \Sigma_L - \Sigma_R]^{-1}$ by slicing the system into smaller cells, which only couple to themselves and their nearest neighbors. H is the Hamiltonian matrix and Σ_L and Σ_R are the self-energies of the semi-infinite pristine graphene left and right leads, respectively. Also, $i\varepsilon$ is a small imaginary factor added to the energy. While ε should, in principle, be infinitesimal, we apply a finite but small value for numerical stability and, in practice, take $\varepsilon = \gamma 10^{-4}$ in all calculations. The lead self-energies are omitted when calculating the DOS of the GALs, as these are additionally periodic along the x direction. Moreover, in the absence of leads, the vector potential in the Landau gauge simply reduces to $\mathbf{A} = \hat{\mathbf{y}}Bx$. The GAL unit cells are indicated by the dashed red lines in Fig. 1. The RGF algorithms require the Hamiltonian to be block tridiagonal. In the case of GABs, the Hamiltonian is

TABLE I. The B field is written as $B = nB_{\min}$, where $B_{\min} = h/(ed y_{\min})$ is the minimal B field that satisfies periodicity of the Peierls phase, with $y_{\min} = a/2\sqrt{3}$ for transport in the zigzag direction. The n at which the relative flux is unity is given by $n_{\max} = 2h/(\sqrt{3}ea^2 B_{\min})$.

Lattice configuration	d	$B_{\min}$ $(2h/\sqrt{3}ea^2)$
Triangular	$3LNa$	$1/LN$
Rotated triangular	LNa	$3/LN$
Rectangular	$L_x Na$	$3/L_x N$
Honeycomb	$3LNa$	$1/LN$

block tridiagonal by construction, but in the case of GALs, it is not, due to periodicity in the x direction coupling the first cell to the last (Nth) one. In this case, the Hamiltonian can easily be made block tridiagonal by merging cells such that cells 1 and N are merged, 2 and $N-1$ are merged, and so forth. The result is that the diagonal blocks double in size, but the resulting matrix is block diagonal.

Due to the additional periodicity of the system in the x direction for GALs, we require the Peierls phase to be an integer multiple of 2π for a pair of neighbor sites on either end of the unit cell in order for the Hamiltonian to be periodic. This limits the B fields that can be used in a calculation, but is remedied by creating a supercell consisting of several unit cells, as was also done in Ref. [16]. The minimal B field which ensures periodicity is denoted $B_{\min}$. The B field is then written as $B = nB_{\min}$, where n is an integer. When the magnetic flux $\Phi = B\sqrt{3}a^2/2$ through a graphene unit cell equals one flux quantum $\Phi_0 = h/e$, the energy spectrum is restored. Therefore, we only let the relative magnetic flux density $\Phi/\Phi_0 \in [0;1]$. The n at which the relative flux is unity is denoted $n_{\max}$. The minimal field is summarized for the different lattice configurations in Table I. In practice, we take advantage of the fact that a given B field can be obtained by several supercell sizes and then always choosing the smallest, as was done in Ref. [16].

The local DOS (LDOS) on atom i is proportional to the diagonal element of the Green's function,

$$L_i(E) = -\frac{1}{\pi}\mathrm{Im}\{G_{ii}\}, \tag{4}$$

and the full DOS is then the sum of all local contributions,

$$D(E) = \sum_i L_i(E). \tag{5}$$

The conductance of the system is given by the Landauer-Büttiker formula $G = \frac{2e^2}{h}T$, where $T = \mathrm{Tr}\{\Gamma_L G^\dagger \Gamma_R G\}$ is the transmittance. Finally, the bond current between atoms i and j at low temperature and low bias V_a can be calculated as [32,43]

$$I_{i\to j}(E) = -\frac{4e^2 V_a}{\hbar}\mathrm{Im}\left\{H_{ij}A^{(L)}_{ji}\right\}, \tag{6}$$

where $A^{(L)} = G\Gamma_L G^\dagger$ is the left-lead spectral function.

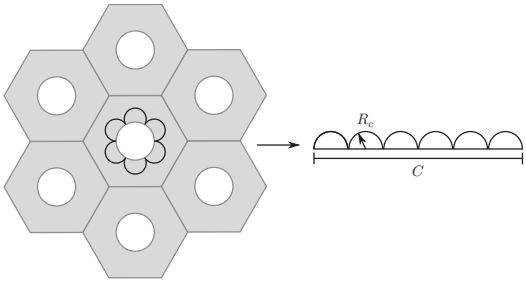

FIG. 2. Magnetic edge state with cyclotron radius R_c for an antidot with circumference C.

B. Magnetic edge states

A prominent feature of GALs is the presence of magnetic edge states. Semiclassically, a magnetic edge state is a state which is confined to the antidot due to repeated reflections off the antidot due to the presence of an applied magnetic field, as illustrated in Fig. 2. In this section, we derive an approximate condition for the occurrence of magnetic edge states. To this end, we will rely on a simple continuum (Dirac) model of gapped graphene. In this model, the energy is given by $E = \pm\sqrt{\hbar^2 v_F^2 k^2 + \Delta^2}$, where $v_F = \sqrt{3}a\gamma/2\hbar \simeq 10^6$ m/s is the Fermi velocity.

The cyclotron radius is given by $R_c = m^* v/eB$ [44], where v is the speed of the electron and m^* is the cyclotron effective mass (or dynamical mass), which is semiclassically given by [44–46]

$$m^* = \frac{\hbar^2}{2\pi}\left[\frac{\partial A(E)}{\partial E}\right]_{E=E_F}. \tag{7}$$

Here, $A(E)$ is the area enclosed by the orbit in k space and given by $A(E) = \pi k^2(E)$ for rotationally symmetric band structures. In the gapped graphene model, we can write $\hbar v_F k(E) = \sqrt{E^2 - \Delta^2}$, and so

$$A(E) = \frac{\pi(E^2 - \Delta^2)}{\hbar^2 v_F^2}, \quad |E| \geqslant \Delta. \tag{8}$$

The cyclotron effective mass is then

$$m^* = \frac{E}{v_F^2}, \quad |E| \geqslant \Delta, \tag{9}$$

which is exactly the same result as for pristine graphene [29,45]. The cyclotron effective mass is thus independent of band gap, given by $E_g = 2\Delta$. It therefore does not change between the pristine graphene in the leads and the antidot regions as long as the energy satisfies $|E| \geqslant \Delta$. The cyclotron radius is then given by

$$R_c = \frac{E}{ev_F B}. \tag{10}$$

In order to have a magnetic edge state, the electron must form a stationary wave on the periphery on the antidot. As an approximation, we analyze the case where the electron is reflected off a straight line with length equal to the circumference of the antidot C. In order to form a stationary

wave, there must be an integer multiple of cyclotron diameters along the length of the line, as illustrated in Fig. 2, which is equivalent to $2nR_c = C$, where n is an integer equal to the number of reflections for a complete circuit of the antidot. The B fields that satisfy this requirement with n reflections are then $B_n = 2nE/ev_FC$. In addition, we require the electron wave function to be in phase after one orbit. The electron gains a phase on one orbit of $\phi = \int_P \mathbf{k}\cdot d\mathbf{l} = kD$, where P is the path traveled by the electron and $D = n\pi R_c = \pi C/2$ is the total distance traveled. We thus require $kD = m2\pi$, where m is an integer. Here, we use the approximation $\hbar v_F k = \sqrt{E^2 - \Delta^2} \approx E$, which is a good approximation when $E \gg \Delta$. The energies that satisfy the phase requirement are then $E = 4m\hbar v_F/C$ and we may finally write the B-field requirement as

$$B_n = \frac{8mn\hbar}{eC^2}. \tag{11}$$

The oscillation period of magnetoresistance caused by magnetic edge states is then given by $\Delta B = 8m\hbar/eC^2$. We see that doubling the antidot circumference, equivalent to quadrupling the area, decreases the oscillation period by a factor of four.

III. RESULTS

Previous transport calculations of GABs without a magnetic field have found their transport gap to be in good agreement with those predicted for Dirac mass barriers (DMBs) [33,38]. These are modeled using the Dirac approximation with a local mass term in order to open a band gap in the barrier region. A derivation of the transmittance of a DMB in a magnetic field is included in the appendix. Figure 3 shows a comparison between the transmittance of GABs with that of DMBs and gapped graphene with similar gap sizes. Note that care must be taken in the DMB model in the $B \to 0$ limit, as the magnetic length then tends to infinity. We note that our $B = 0$ T results are consistent with the nonmagnetic DMB expression in Ref. [38]. An excellent qualitative match is seen between the DMB and the gapped graphene barrier in almost all cases. The match between these simplified models and GABs is quite good near the onset of the transport gap, particularly for smaller antidots. However, discrepancies appear as the energy is increased towards higher-order GAB features, as the antidot size increases, and as the field is increased further (not shown). The DMB and gapped graphene models are therefore good for approximating the transport gap given that the magnetic field is not too large.

A. Comparison with DOS

Figure 4 shows a comparison between DOS and transmittance of $\{L,6\}$ GABs for four different lattice configurations as well as for a gapped graphene model. L was chosen such that the neck widths were approximately the same ($\simeq$1.3 nm) for all lattices. The transport calculations were performed with four rows of antidots in the transport direction. The figure shows that the transmittance spectra retains most of the features of the DOS for all lattice configurations and for gapped graphene. The gapped graphene model shows no transmittance between the band gap and first Landau level. A similar situation arises in the GABs, where we can identify a *geometric band gap*

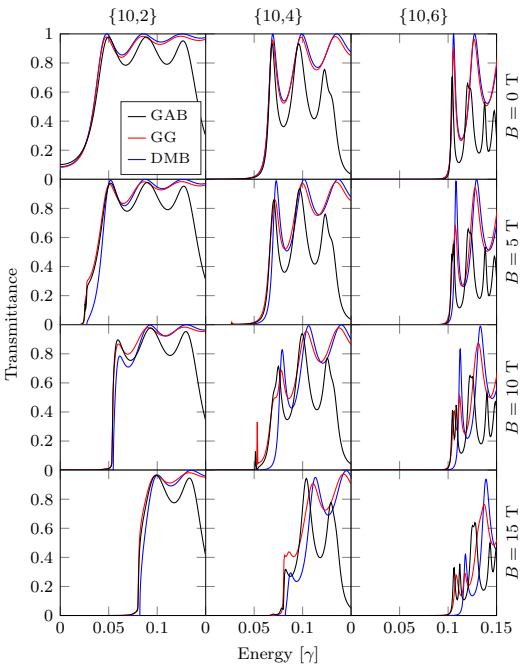

FIG. 3. Transmission through $\{10,S\}$ triangular GABs containing four rows of antidots in the transport direction, as well as gapped graphene (GG) barriers and Dirac mass barriers (DMBs) with the same length ($d = 16.5$ nm) and band gaps as the GABs. All calculations were made for $k_y = 0$. The tight-binding (TB) calculations are divided by two for comparison with the single valley Dirac result.

and a *Landau-level gap*, which are outlined for the triangular lattice (top panels in Fig. 4) with dashed red and yellow lines, respectively. The differences between the spectra are greatest for small fields. Notice that transport is not fully suppressed in the band-gap regions, due to the finite width of the barrier. We observe rather high transmittance in the geometric energy gap regions of the rotated triangular lattice, while the transport gap appears larger than the band gap for the rectangular lattice. Additionally, there is rather high transmittance in the band-gap region of the honeycomb lattice, and the secondary band gap is completely invisible in transport.

A striking similarity between all GAB lattice configurations is the narrow bands in the Landau-level gap region. We will demonstrate that these are due to magnetic edge states, i.e., states that are localized on the periphery of the antidots by the magnetic field, as illustrated in Fig. 2. According to Eq. (10), the edge states here all have cyclotron radii which are smaller than the antidot radius. The similarity between the panels of the figure demonstrates that the magnetic edge states are robust against lattice configuration. The reason for the relatively high transmittance of these states is that the antidots are close enough to their neighbors that the states couple between antidots. Magnetically induced band-gap quenching

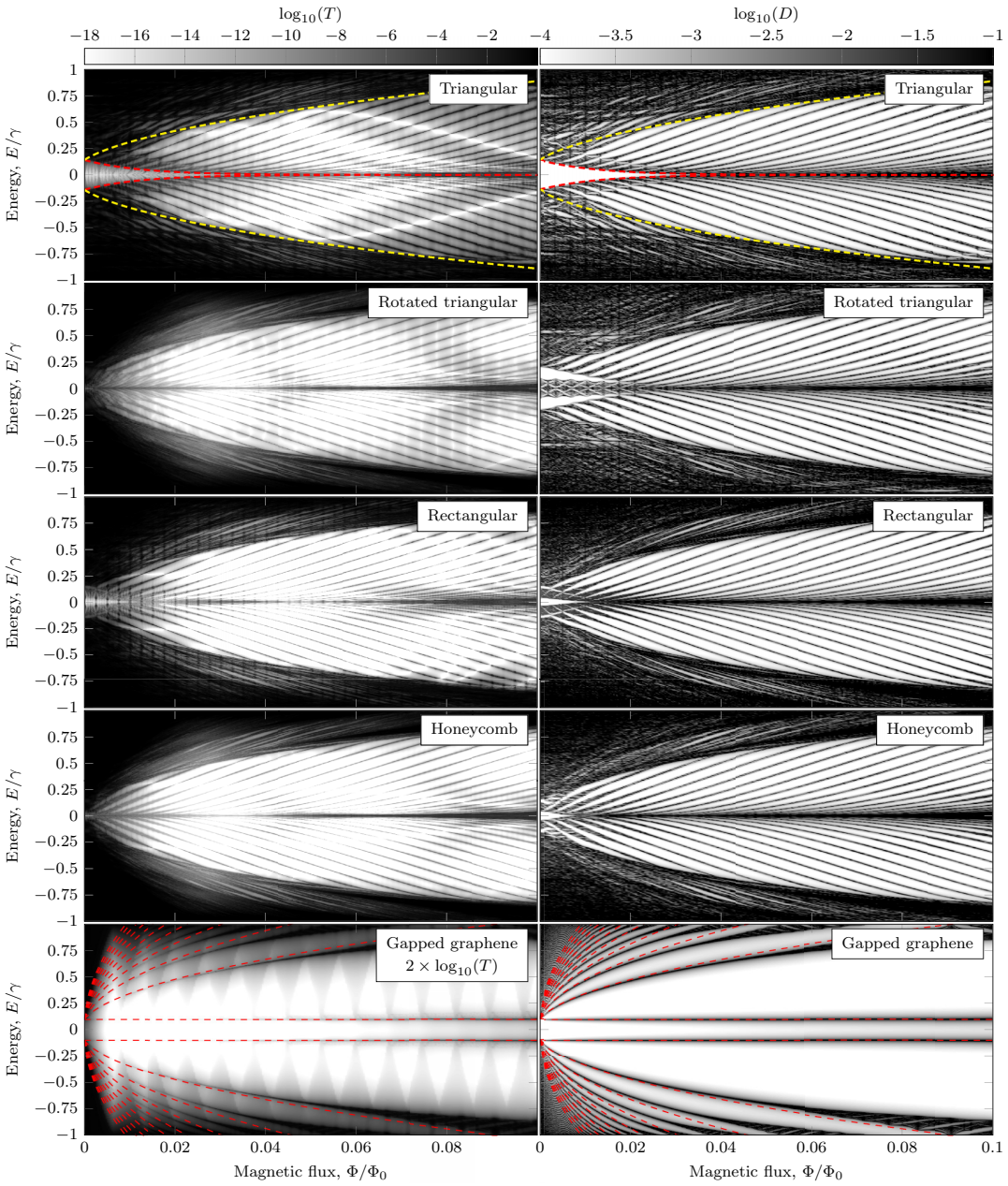

FIG. 4. Comparison between transmittance (left) and DOS (right) of $\{L,6\}$ GABs in different lattice configurations. L is chosen to give the systems approximately the same neck width ($\simeq$1.3 nm). For the triangular antidot lattice, this corresponds to a $\{10,6\}$ system. The transport calculations are made with four rows of antidots in the transport direction. The dashed lines in the top panels outline the geometric band gap (red) and the Landau-level gap (yellow). The two bottom panels show a $\Delta = 0.1\gamma$ gapped graphene system. The dashed red lines in the bottom panels show the first 10 Landau levels of massive Dirac fermions, $E_n = \pm\sqrt{\Delta^2 + 2v_F^2\hbar eBn}$ [16]. For the gapped graphene model, we plot $2 \times \log_{10}(T)$ due to the generally lower transmittance for this system.

is observed both in the DOS and in transmittance. The quenching seems to be due to magnetic edge states as the magnetic edge state bands begin to form at the quenched band gap. Band-gap quenching may therefore disappear if the distance between antidots is increased sufficiently or if a large degree of disorder is introduced.

Since magnetic edge states are localized on the antidot edge, these are of course absent in the gapped graphene model. The gapped graphene model in Fig. 4 has approximately the same band gap as the {10,6} triangular GAB. However, at these B-field values, there is little resemblance between their transmittance spectra. For instance, in the GAB, the transport gap is quenched by the magnetic field, while the transport gap is retained in the gapped graphene model. It was argued in Ref. [16] that band-gap quenching occurs when the magnetic length become sufficiently small that the eigenstates do not sample the lattice sufficiently for the band gap to be fully resolved. In gapped graphene, however, the band gap is not introduced by geometrical effects and is therefore retained. Another notable difference between the gapped graphene model and the GAB is that practically all transmittance, except for the Landau levels, is suppressed in the gapped graphene model for large magnetic fields, which is not the case for the GAB. The gapped graphene result is consistent with results by De Martino *et al.* [47], who showed that Dirac electrons incident on a wide magnetic barrier (i.e., either wide spatial region or large magnetic field) will be totally reflected by the barrier independent of the angle of incidence. The GAB result is also consistent with the results by Xu *et al.* [31] that magnetic barriers in graphene nanoribbons are unable to completely suppress electron transport due to successive reflections on the nanoribbon edge. GALs can be viewed as a connected network of graphene nanoribbons, so the similarity to the nanoribbon case is expected.

The periodic features in the transmittance of the gapped graphene model are Fabry-Pérot-type oscillations, which are a result of the additional phase factor that comes from the magnetic field. Additional calculations show that the oscillations double in frequency when the device length is doubled, hence demonstrating the Fabry-Pérot-type nature of the oscillations. This type of oscillations in transmittance has previously been observed in graphene nanoribbons in a magnetic field [31]. Additionally, we observe excellent agreement between the gapped graphene model and the predicted Landau levels.

B. Magnetic edge states

In order to show that the narrow bands in transmittance are indeed edge states, we show the bond current and LDOS of a {10,6} triangular GAB at different magnetic fields and at different energies in Fig. 5. It is clear that the bond currents at these bands are localized around the antidots, whereas the bond currents elsewhere are not. The shown bond currents are averaged over small area elements, which is

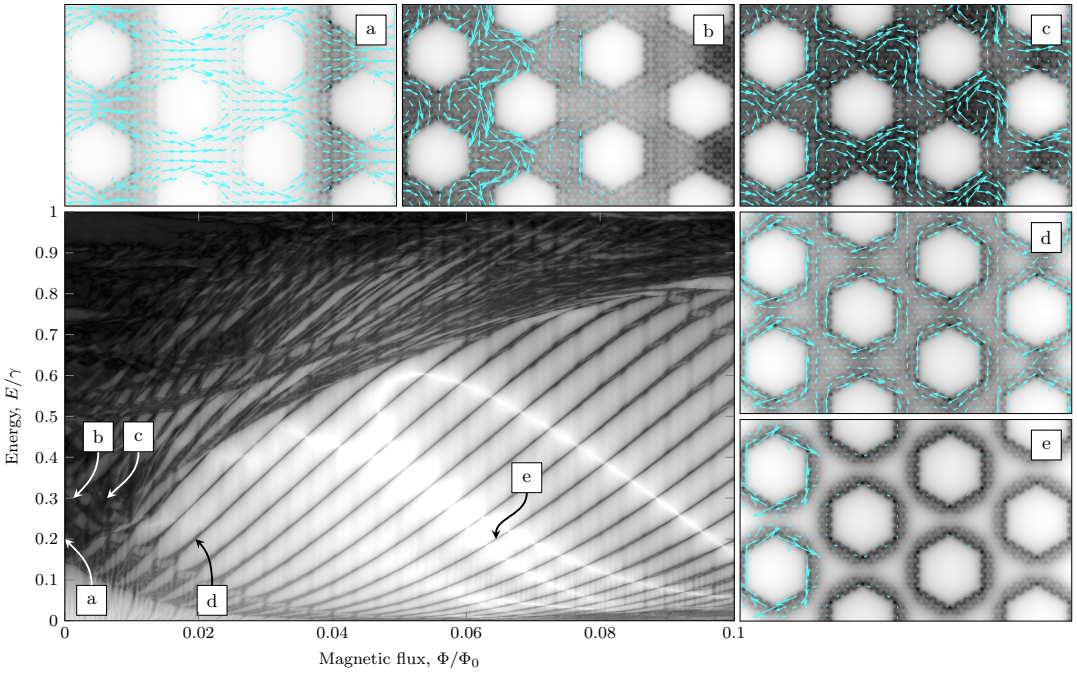

FIG. 5. LDOS (gray shading) and bond current (blue arrows) of a {10,6} triangular GAB for different B-field strengths at energies of (a),(d),(e) $E = 0.2\gamma$ or (b),(c) $E = 0.3\gamma$. The main panel shows the transmittance of the system. Here, we plot $\sqrt{|\log_{10}(T)|}$ in order to enhance the contrast.

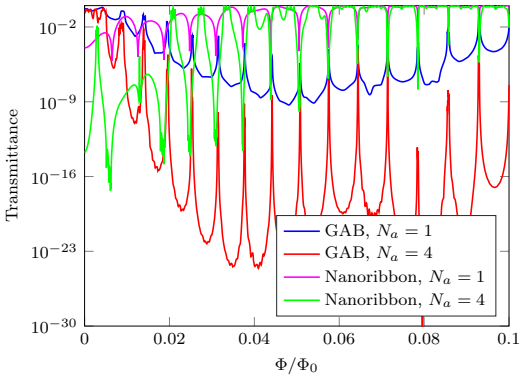

FIG. 6. Transmittance as a function of applied magnetic field at an energy of $E = 0.2\gamma$ for four different rectangular antidot lattice systems with N_a antidots in the transport direction.

why bond currents appear inside some of the antidots. This averaging may also give rise to a visual artifact, where it can appear as if the Kirchoff's current law is not obeyed on small scale. However, we have verified that the bond currents themselves do satisfy the current law. Additionally, the lengths of the arrows are scaled such that the longest arrow in all plots have the same length. In the case of circular current paths or large transverse currents, this can make it appear as if the current does not propagate through the barrier and therefore make it seem like the transmittance should be lower than it is.

According to Eq. (11), the oscillation period of the transmittance with respect to the B field only depends on the circumference of the antidot. This is in agreement with the observation that the energies of the edge state bands are nearly linearly dependent on the B field, thus giving rise to the same oscillation period for all energies. Increasing the magnetic field corresponds to decreasing the cyclotron radius, which in turn should decrease the average electron distance from the antidot. This is indeed the case, which is apparent when comparing Figs. 5(d) and 5(e). According to Eq. (11), the oscillation period is independent of lattice configuration (as confirmed by Fig. 4), number of antidots, and whether the system is periodic or nonperiodic, i.e., a graphene nanoribbon. In Fig. 6, we show the transmittance of GABs and nanoribbons with one and four rows of antidots in the transport direction. We find indeed that the oscillation period is unaffected by both the number of antidots and periodicity, supporting the validity of Eq. (11). For the GABs, we see increased transmittance on the edge state resonances, due to these being the only available states. However, for the nanoribbons, we see decreased transmittance on the edge state resonances. In the nanoribbon case, there is transmission along the edges of the system at these energies without the antidot. Introducing the antidots then gives the electrons a possibility to couple to the antidot magnetic edge states and backscatter. This explains the increased (decreased) transmittance at the edge state resonances for the GAB (nanoribbon) case. Additional calculations show that zigzag antidots with similar circumference have approximately the same oscillation period as armchair antidots (not shown). This demonstrates that the magnetic edge states are additionally robust against antidot edge chirality.

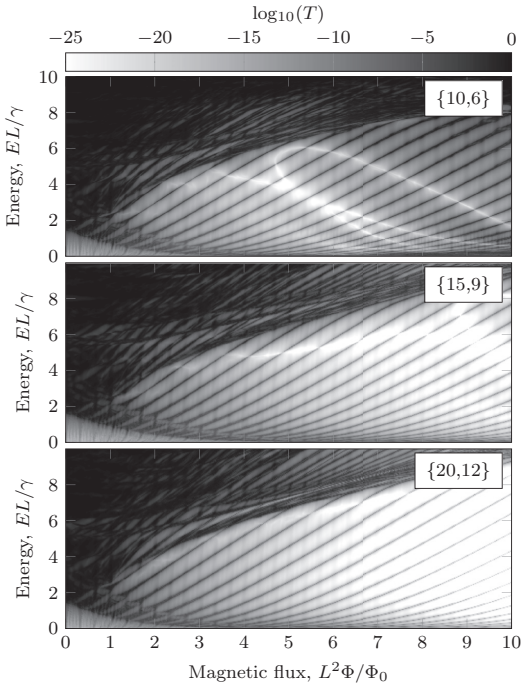

FIG. 7. Transmittance of {10,6},{15,9}, and {20,12} triangular GABs in scaled units.

In Fig. 7, we compare the transmittance of different $\{L,0.6L\}$ triangular GABs, where the energy and magnetic field axes have been scaled with L and L^2, respectively. We see that by plotting on scaled axes, the spectrum is very nearly conserved. The scaling with respect to the B-field is consistent with Eq. (11), which states that the oscillation period due to magnetic edge states is inversely proportional to the square of the circumference. It is remarkable that Eq. (11) correctly predicts (i) the periodicity of the edge state bands, (ii) the insensitivity to the lattice arrangement of the antidots, and (iii) the behavior under uniform geometry scaling. Additionally, the geometry scaling shows that even though the structures we consider here are probably too small for current experimental realization, our conclusions should hold for larger structures at smaller magnetic fields and energies. Finally, Fig. 7 shows that the transmittance of the magnetic edge states decreases as the distance between antidots is increased, which is expected as these states are localized to the edges of antidots.

C. Disorder

The systems we have considered until now have been fully ordered. However, experimental samples tend to have varying degrees of disorder. It is therefore important to understand

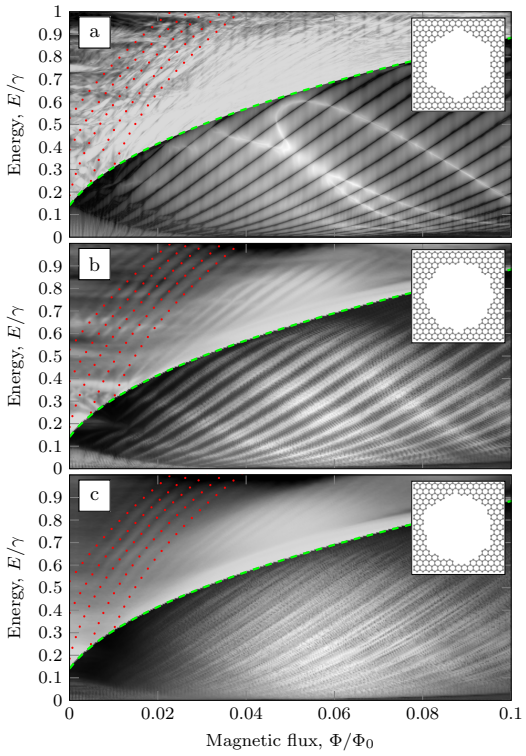

FIG. 8. Ensemble-averaged transmittance of (a) an ordered {10,6} triangular GAB and of disordered systems with (b) $\sigma = 0.5$ and (c) $\sigma = 1$. The area of the antidots is on average the same in the disordered and ordered systems. An example of the disordered antidots in the two cases is shown as an inset. In order to highlight the features in the plot, we plot T above and $\log T$ below the dashed green line. The dotted red lines are plotted according to $E_i/\gamma = \sqrt{a_i + b\Phi/\Phi_0}$, where a_i and $b \approx 31.668$ were determined by least-squares fitting.

the effects of disorder and find out which features of the transmittance remain. The effects of disorder are investigated by ensemble averaging transmittance over different realizations of unit cells with disordered antidots. The antidots were created by first removing six carbon atoms at the locations of the antidots and then iteratively removing edge atoms according to a Gaussian weight profile $w(\mathbf{r}) = \frac{1}{N}\sum_i^N e^{-|\mathbf{r}-\mathbf{r}_i|^2/(2\sigma^2 a^2)}$, where $\mathbf{r}$ is the position of the atom, $\mathbf{r}_i$ are the centers of the antidots in the ordered system, and σ is the standard deviation measured in graphene lattice constants a. A large (small) σ gives rise to a large (small) degree of disorder. This creates antidots that are roughly centered at the position of the ordered system but with disordered edges. In order to decrease the effects of periodicity, the unit cells are doubled in size in the periodic direction such that there are eight antidots in the unit cells instead of four. The ensemble size is determined by convergence testing, and is about 50–100 in the cases we study here.

The ensemble-averaged transmittance of two disordered systems with $\sigma = 0.5$ and $\sigma = 1$, respectively, is shown in Fig. 8 where it is compared to the ordered system. The figure shows that as the amount of disorder is increased, the rich substructure in transmittance observed in the ordered system is almost completely washed out. However, some of the features of the ordered system do remain. These features form narrow transmittance bands that are highlighted by the fitted red curves in the figure. They are also present in the ordered system, but here they are almost completely disguised by the rich substructure in the transmittance, which is absent in the disordered systems.

Both the Landau levels of pristine graphene, $E_n = \sqrt{2v_F^2\hbar eBn}$ [16], and the energy levels of a single graphene antidot in a magnetic field [19] scale as $\sqrt{B}$. Therefore, we fit the features in the transmittance spectrum to an expression of the form $E_i/\gamma = \sqrt{a_i + b\Phi/\Phi_0}$, where a_i and b are fitting parameters, which are determined by least-squares fitting. In all cases, we find $b \approx 31.668$ although no explanation for this observation has been found. The fitted curves are shown as the dotted red lines on the plots. The fit shows that these features do indeed scale approximately as $\sqrt{B}$, albeit with an offset.

Both magnetically induced band-gap quenching and magnetic edge states in the Landau gap are present for the $\sigma = 0.5$ disordered system. However, compared to the ordered system, the initial band gap is decreased and the magnetic edge state bands are broadened. For the $\sigma = 1$ disordered system, the edge state bands are broadened sufficiently so that they are almost impossible to identify. Additionally, the band-gap quenching for this system is less pronounced. The broadening of the magnetic edge state bands is expected as the antidot circumference now differs between individual perforations and, according to Eq. (11), a variation in circumference of 5% will lead to a 10% change in the magnetic edge state band position. Hence, transmittance features within the Landau gap may be difficult to observe experimentally in disordered samples. In contrast, the robustness of the features above the Landau gap, combined with the long phase-coherence length in graphene, suggests that these states will also be observable in experiments even in the presence of disorder.

IV. CONCLUSIONS

Using a recursive Green's-function method, we have calculated electronic transmission and density of states of graphene antidot barriers and graphene antidot lattices, respectively, in magnetic fields. We find, in general, electronic transmission and density of states spectra to be in good agreement. We have additionally derived an expression for the transmittance of Dirac mass barriers in magnetic fields and found that this provides a good description of the transport gap of graphene antidot barriers for small antidot sizes and low to moderate field strengths. Calculations of gapped graphene barriers, i.e., graphene with a staggered sublattice potential, are in good agreement with the Dirac mass barrier, and therefore show the same limitations.

We find that antidots support magnetic edge states, which are robust against variations in lattice configuration, antidot edge chirality, periodicity, and number of antidots. Moreover,

we observe that these edge states survive a modest degree of disorder. The robustness of these states suggests that they will also be observable in experiments even in the presence of disorder. Furthermore, we find that our results scale in a simple manner with system size, thus allowing calculations on small structures to generalize to larger structures. Additionally, we observe magnetically induced band-gap quenching in both density of states and transmittance due to magnetic edge states. In the presence of mild disorder, some fine structure is washed out, but several characteristic and prominent transmission bands are found to survive.

ACKNOWLEDGMENTS

The authors would like to thank Mikkel Settnes for valuable discussions. Furthermore, the authors gratefully acknowledge the financial support from the Center for Nanostructured Graphene (Project No. DNRF103) financed by the Danish National Research Foundation and from the QUSCOPE project financed by the Villum Foundation.

APPENDIX: DIRAC MASS BARRIER

We can estimate the transmittance through a GAB in a magnetic field by using the Dirac equation with mass term and magnetic field. The mass term and magnetic field are nonzero only in the barrier region, thereby creating a magnetic Dirac mass barrier (DMB). We calculate the transmission through this system by matching wave functions at the interfaces on either side of the barrier at $x = 0$ and $x = d$. We denote the regions where $x < 0, 0 \leqslant x \geqslant d$, and $x > d$ as region I, II, and III, respectively. The wave functions are given by the eigenstates of a generalized Dirac equation, which arises from the substitution $\mathbf{p} \to \boldsymbol{\pi}$, where $\boldsymbol{\pi} = \mathbf{p} + e\mathbf{A}$ is the generalized momentum,

$$\begin{pmatrix} \tilde{\Delta}(x) & \frac{1}{\hbar}\pi_-^\xi \\ \frac{1}{\hbar}\pi_+^\xi & -\tilde{\Delta}(x) \end{pmatrix} \begin{pmatrix} \psi_1 \\ \psi_2 \end{pmatrix} = k \begin{pmatrix} \psi_1 \\ \psi_2 \end{pmatrix}. \tag{A1}$$

Here, $\tilde{\Delta}(x) = \Delta(x)/\hbar v_F$, where $\Delta(x)$ is a mass term, which we set equal to Δ inside the barrier to open a band gap of 2Δ, and vanishing elsewhere. $k = E/\hbar v_F$ is the magnitude of the wave vector corresponding to energy E in graphene in the absence of a B field or mass term. Also,

$$\pi_\pm^\xi = \xi\pi_x \pm i\pi_y \tag{A2}$$

are the standard linear combinations of the x and y components of momenta that occur in the Dirac equation for graphene charge carriers in the $\xi = \pm 1$ valley. From now on, we shall assume identical contributions from the valleys and drop the ξ index. To set a constant magnetic field of strength B in the $\hat{\mathbf{z}}$ direction in the barrier, we choose a Landau gauge; see Eq. (2). Since this gauge, and the system in general, is invariant along $\hat{\mathbf{y}}$, we can write the spinor components of the wave function in terms of Bloch functions,

$$\begin{pmatrix} \psi_1 \\ \psi_2 \end{pmatrix} = \begin{pmatrix} f(x) \\ g(x) \end{pmatrix} e^{ik_y y}. \tag{A3}$$

Region I. As the vector field is zero in region I, the wave functions here are identical to those in pristine graphene. The total wave function can be written as a sum of an incoming (right-going) component of unit amplitude and a reflected (left-going) component, giving

$$\Psi_\mathrm{I} = \frac{1}{\sqrt{2}}\left[\begin{pmatrix} 1 \\ e^{i\theta_k} \end{pmatrix} e^{ik_x x} + r\begin{pmatrix} 1 \\ -e^{-i\theta_k} \end{pmatrix} e^{-ik_x x}\right] e^{ik_y y}, \tag{A4}$$

where $\theta_k = \tan^{-1}(k_y/k_x)$ and r is the reflection coefficient.

Region II. In region II, the wave functions are solutions of Eq. (A1) with nonzero mass and B field. Making the substitutions $p_x \to -i\hbar\partial_x$ and $p_y \to \hbar k_y$ and rearranging gives

$$\begin{aligned} \left[-\partial_x^2 + W_+(x)\right] f(x) &= k^2 f(x), \\ \left[-\partial_x^2 + W_-(x)\right] g(x) &= k^2 g(x), \end{aligned} \tag{A5}$$

where

$$W_\pm(x) = \tilde{\Delta}^2 \pm \frac{1}{l_B^2} + \left(k_y + \frac{x}{l_B^2}\right)^2, \tag{A6}$$

where $l_B = \sqrt{\hbar/eB}$ is the magnetic length.

By using the substitutions $z = \sqrt{2}(k_y l_B + x/l_B)$ and $\nu = (k^2 - \tilde{\Delta}^2)l_B^2/2 - 1$, the expression for $f(x)$ becomes the Weber differential equation,

$$\left(\partial_z^2 + \nu + \frac{1}{2} - \frac{z^2}{4}\right) f(x) = 0, \tag{A7}$$

which has solutions in the form of *parabolic cylinder functions* $D_\nu(\pm z)$. This allows us to write

$$f(x) = \frac{1}{\sqrt{2}}[\alpha D_\nu(z) + \beta D_\nu(-z)]. \tag{A8}$$

Moreover, $g(x)$ can be related to $f(x)$ using Eq. (A1), and using the identity $\partial_z D_\nu(z) = \frac{z}{2} D_\nu(z) - D_{\nu+1}(z)$, we find

$$g(x) = \frac{i}{l_B(k + \tilde{\Delta})}[\alpha D_{\nu+1}(z) - \beta D_{\nu+1}(-z)]. \tag{A9}$$

The full wave function in region II is then

$$\Psi_\mathrm{II} = \frac{1}{\sqrt{2}}\begin{pmatrix} \alpha D_\nu(z) + \beta D_\nu(-z) \\ \frac{\sqrt{2}i}{l_B(k+\tilde{\Delta})}[\alpha D_{\nu+1}(z) - \beta D_{\nu+1}(-z)] \end{pmatrix} e^{ik_y y}. \tag{A10}$$

Region III. In region III, the magnetic field and mass terms are set to zero again. However, unlike, e.g., Klein tunneling problems where the wave function has a similar form to region I, here we must account for the constant vector potential remaining in this region. The vector potential cannot be set to zero in this region, as this would imply an infinite magnetic field in the interface between regions II and III. We define a wave vector,

$$\mathbf{K} = K_x\hat{\mathbf{x}} + \left(k_y + \frac{eB}{\hbar}d\right)\hat{\mathbf{y}}, \tag{A11}$$

in this region, and enforcing conservation of energy, which is equivalent to conservation of the magnitude of the momentum $K = k$, gives

$$K_x = \sqrt{k_x^2 - \frac{d^2}{l_B^4} - 2\frac{d}{l_B^2}k_y}. \tag{A12}$$

The wave function in region III is then

$$\Psi_{\mathrm{III}} = \frac{t}{\sqrt{2}}\begin{pmatrix}1\\ e^{i\theta_K}\end{pmatrix}e^{i(K_x x + k_y y)}. \tag{A13}$$

Boundary matching. Continuity of the spinor wave function components at the interfaces gives the following set of simultaneous equations, which can be solved for r,α,β, and t:

$$\begin{aligned}
1 + r &= \alpha D_\nu(z_0) + \beta D_\nu(-z_0),\\
te^{iK_x d} &= \alpha D_\nu(z_d) + \beta D_\nu(-z_d),\\
e^{i\theta_k} - re^{-i\theta_k} &= \frac{\sqrt{2}i}{l_B(k+\tilde{\Delta})}[\alpha D_{\nu+1}(z_0) - \beta D_{\nu+1}(-z_0)],\\
te^{i(\theta_K + K_x d)} &= \frac{\sqrt{2}i}{l_B(k+\tilde{\Delta})}[\alpha D_{\nu+1}(z_d) - \beta D_{\nu+1}(-z_d)].
\end{aligned} \tag{A14}$$

These four equations are all linear in the coefficients, which makes it straightforward to formulate them as a matrix problem and solve for the coefficients numerically. We can then calculate the reflectance and transmittance as $R = |r|^2$ and $T = |t|^2\mathrm{Re}\{K_x/k_x\} = 1 - R$. The K_x/k_x factor is necessary in order to account for the change in longitudinal momentum. Note that the expressions for R and T are exactly the same as those used in optics.

[1] T. G. Pedersen, C. Flindt, J. Pedersen, N. A. Mortensen, A.-P. Jauho, and K. Pedersen, Phys. Rev. Lett. **100**, 136804 (2008).
[2] R. Petersen, T. G. Pedersen, and A.-P. Jauho, ACS Nano **5**, 523 (2010).
[3] J. Eroms and D. Weiss, New J. Phys. **11**, 095021 (2009).
[4] M. Kim, N. S. Safron, E. Han, M. S. Arnold, and P. Gopalan, Nano Lett. **10**, 1125 (2010).
[5] J. Bai, X. Zhong, S. Jiang, Y. Huang, and X. Duan, Nat. Nanotechnol. **5**, 190 (2010).
[6] F. Oberhuber, S. Blien, S. Heydrich, F. Yaghobian, T. Korn, C. Schüller, C. Strunk, D. Weiss, and J. Eroms, Appl. Phys. Lett. **103**, 143111 (2013).
[7] S. J. Brun, M. R. Thomsen, and T. G. Pedersen, J. Phys. Condens. Matter **26**, 265301 (2014).
[8] A. Sandner, T. Preis, C. Schell, P. Giudici, K. Watanabe, T. Taniguchi, D. Weiss, and J. Eroms, Nano Lett. **15**, 8402 (2015).
[9] R. Yagi, R. Sakakibara, R. Ebisuoka, J. Onishi, K. Watanabe, T. Taniguchi, and Y. Iye, Phys. Rev. B **92**, 195406 (2015).
[10] L. Wang, I. Meric, P. Y. Huang, Q. Gao, Y. Gao, H. Tran, T. Taniguchi, K. Watanabe, L. M. Campos, D. A. Muller, J. Guo, P. Kim, J. Hone, K. L. Shepard, and C. R. Dean, Science **342**, 614 (2013).
[11] T. Taychatanapat, K. Watanabe, T. Taniguchi, and P. Jarillo-Herrero, Nat. Phys. **9**, 225 (2013).
[12] K. S. Novoselov, Z. Jiang, Y. Zhang, S. V. Morozov, H. L. Stormer, U. Zeitler, J. C. Maan, G. S. Boebinger, P. Kim, and A. K. Geim, Science **315**, 1379 (2007).
[13] C. R. Dean, A. F. Young, P. Cadden-Zimansky, L. Wang, H. Ren, K. Watanabe, T. Taniguchi, P. Kim, J. Hone, and K. L. Shepard, Nat. Phys. **7**, 693 (2011).
[14] X. Du, I. Skachko, F. Duerr, A. Luican, and E. Y. Andrei, Nature (London) **462**, 192 (2009).
[15] J. Baringhaus, M. Settnes, J. Aprojanz, S. R. Power, A.-P. Jauho, and C. Tegenkamp, Phys. Rev. Lett. **116**, 186602 (2016).
[16] J. G. Pedersen and T. G. Pedersen, Phys. Rev. B **87**, 235404 (2013).
[17] S. İslamoğlu, M. Ö. Oktel, and O. Gülseren, Phys. Rev. B **85**, 235414 (2012).
[18] Z. Z. Zhang, K. Chang, and F. M. Peeters, Phys. Rev. B **77**, 235411 (2008).
[19] J. G. Pedersen and T. G. Pedersen, Phys. Rev. B **85**, 035413 (2012).
[20] D. R. Hofstadter, Phys. Rev. B **14**, 2239 (1976).
[21] M. L. Trolle, U. S. Møller, and T. G. Pedersen, Phys. Rev. B **88**, 195418 (2013).
[22] Y. Takagaki and D. K. Ferry, Surf. Sci. **305**, 669 (1994).
[23] E. N. Bogachek and U. Landman, Phys. Rev. B **52**, 14067 (1995).
[24] S. Ishizaka and T. Ando, Phys. Rev. B **55**, 16331 (1997).
[25] D. Weiss, M. L. Roukes, A. Menschig, P. Grambow, K. von Klitzing, and G. Weimann, Phys. Rev. Lett. **66**, 2790 (1991).
[26] F. Nihey and K. Nakamura, Physica B **184**, 398 (1993).
[27] R. Schuster, K. Ensslin, D. Wharam, S. Kühn, J. P. Kotthaus, G. Böhm, W. Klein, G. Tränkle, and G. Weimann, Phys. Rev. B **49**, 8510 (1994).
[28] R. Farghadan, A. Saffarzadeh, and E. H. Semiromi, J. Appl. Phys. **114**, 214314 (2013).
[29] S. Bhandari, G. Lee, A. Klales, K. Watanabe, T. Taniguchi, E. Heller, P. Kim, and R. Westervelt, Nano Lett. **16**, 1690 (2016).
[30] S. Morikawa, Z. Dou, S.-W. Wang, C. G. Smith, K. Watanabe, T. Taniguchi, S. Masubuchi, T. Machida, and M. R. Connolly, Appl. Phys. Lett. **107**, 243102 (2015).
[31] H. Xu, T. Heinzel, M. Evaldsson, and I. V. Zozoulenko, Phys. Rev. B **77**, 245401 (2008).
[32] S. R. Power and A.-P. Jauho, Phys. Rev. B **90**, 115408 (2014).
[33] M. R. Thomsen, S. J. Brun, and T. G. Pedersen, J. Phys. Condens. Matter **26**, 335301 (2014).
[34] J. G. Pedersen, T. Gunst, T. Markussen, and T. G. Pedersen, Phys. Rev. B **86**, 245410 (2012).
[35] M. R. Thomsen, M. M. Ervasti, A. Harju, and T. G. Pedersen, Phys. Rev. B **92**, 195408 (2015).
[36] S. Datta, *Electronic Transport in Mesoscopic Systems* (Cambridge University Press, Cambridge, UK, 1995).
[37] T. Markussen, R. Rurali, M. Brandbyge, and A.-P. Jauho, Phys. Rev. B **74**, 245313 (2006).
[38] T. G. Pedersen and J. G. Pedersen, J. Appl. Phys. **112**, 113715 (2012).
[39] T. Gunst, T. Markussen, A.-P. Jauho, and M. Brandbyge, Phys. Rev. B **84**, 155449 (2011).

[40] T. G. Pedersen, A. P. Jauho, and K. Pedersen, Phys. Rev. B **79**, 113406 (2009).
[41] A. Svizhenko, M. Anantram, T. Govindan, B. Biegel, and R. Venugopal, J. Appl. Phys. **91**, 2343 (2002).
[42] C. H. Lewenkopf and E. R. Mucciolo, J. Comput. Electron. **12**, 203 (2013).
[43] T. N. Todorov, J. Phys. Condens. Matter **14**, 3049 (2002).
[44] N. W. Ashcroft and N. D. Mermin, *Solid State Physics* (Saunders College Publishing, Philadelphia, USA, 1976).
[45] A. Castro Neto, F. Guinea, N. Peres, K. S. Novoselov, and A. K. Geim, Rev. Mod. Phys. **81**, 109 (2009).
[46] L. Smrčka and T. Jungwirth, J. Phys. Condens. Matter **6**, 55 (1994).
[47] A. De Martino, L. Dell'Anna, and R. Egger, Phys. Rev. Lett. **98**, 066802 (2007).

ISSN (online): 2246-1248
ISBN (online): 978-87-7112-791-1

AALBORG UNIVERSITY PRESS